

**THEORETICAL AND NUMERICAL STUDIES OF
SEMICONDUCTING CARBON NANOTUBES**

A THESIS
PRESENTED TO
THE ACADEMIC FACULTY
BY
AMIT VERMA

IN PARTIAL FULFILLMENT
OF THE REQUIREMENTS FOR THE DEGREE OF
DOCTOR OF PHILOSOPHY IN ELECTRICAL ENGINEERING

GEORGIA INSTITUTE OF TECHNOLOGY

May 2006

THEORETICAL AND NUMERICAL STUDIES OF SEMICONDUCTING CARBON NANOTUBES

Approved by:

Dr. P. Paul Ruden, Advisor
Department of Electrical and
Computer Engineering
University of Minnesota

Dr. W. R. Callen, Advisor
School of Electrical and
Computer Engineering
Georgia Institute of Technology

Dr. D. S. Citrin
School of Electrical and Computer
Engineering
Georgia Institute of Technology

Dr. A.B. Frazier
School of Electrical and
Computer Engineering
Georgia Institute of Technology

Dr. C. J. Summers
School of Materials Science and
Engineering
Georgia Institute of Technology

Dr. H. M. Zhou
School of Mathematics
Georgia Institute of Technology

Date Approved: December 15, 2005

To my wife Tejal

ACKNOWLEDGMENTS

I wish to thank my advisors Dr. Paul Ruden and Dr. Russ Callen, not only for their valuable guidance throughout the course of this research, but also for the invaluable support after the sad demise of Dr. Kevin Brennan.

Special thanks go to Zahed Kauser. Without his participation, and significant contributions in the research, this thesis would not have been possible.

In addition, I am also grateful to all the people with whom I have had the pleasure and honor to work: Chi-Ti Hsieh, Dr. Tsung-Hsing Yu, and Dr. Michael Weber.

Special thanks also go to my wife Tejal for her endless support and encouragement throughout my doctoral studies years. This thesis is dedicated to her.

TABLE OF CONTENTS

	Page
ACKNOWLEDGEMENTS	iv
LIST OF TABLES	viii
LIST OF FIGURES	ix
SUMMARY	xii
<u>CHAPTER</u>	
1. Introduction	1
1.1 History of the problem	1
1.2 Objective	6
1.3 Overview of the Thesis	7
1.4 Physical structure of carbon nanotubes	8
1.5 Brillouin zone for a CNT	12
1.6 Electronic band structure of carbon nanotubes	16
1.6.1 Band structure of 2-D graphite	16
1.6.2 Band structure of carbon nanotubes	18
1.6.3 Electron effective mass	27
1.7 Phonon dispersion	31
1.8 Electron-phonon interaction	37
2. Ensemble Monte Carlo simulation for semiconducting carbon nanotubes	41
2.1 Boltzmann transport equation	41
2.2 Monte Carlo method	42
2.3 Ensemble Monte Carlo simulation for carbon nanotubes	47

3. Results and discussion	59
3.1 Scattering rates	61
3.2 Steady-state	64
3.2.1 Field dependent mobility	64
3.2.1.a Velocity and mobility behavior with electric field	64
3.2.1.b Diameter dependence of the velocity	69
3.2.1.c Temperature dependence of the velocity	73
3.2.1.d Impact of individual scattering rates on velocity	75
3.2.2 Low-field mobility	79
3.3 Transient phenomenon	84
3.3.1 Transient velocity	84
3.3.1.a Average transient velocity response	84
3.3.1.b Diameter dependence of the velocity	88
3.3.1.c Effect of various scattering rates	90
3.3.2 Ballistic distance	94
4. Conclusion	98
4.1 Conclusions	98
4.1.1 Low-field mobility	99
4.1.2 Field dependent mobility	100
4.1.3 Transient phenomena	102
4.1.3.a Velocity response	102
4.1.3.b Ballistic distance	103
4.2 Recommendations for future work	104

APPENDIX	106
REFERENCES	110

LIST OF TABLES

		Page
Table 3.1	Semiconducting zigzag CNTs included in this work, and their grouping.	60

LIST OF FIGURES

		Page
Figure 1.1	Illustration of a multi-walled CNT.	3
Figure 1.2	An illustration of a top-gated structure for a CNTFET.	4
Figure 1.3	Fundamental parameters of a CNT, and relationship of those parameters to those of graphene.	10
Figure 1.4	Three distinct carbon nanotubes: a. armchair, b. zigzag, and c. chiral.	12
Figure 1.5	Direct (a), and indirect (b) lattice structure of graphene.	14
Figure 1.6	Extended reciprocal zone for CNT (4,2) superimposed on the graphene reciprocal lattice.	17
Figure 1.7	Illustration of the electron energy dispersion of the π and π^* orbitals for graphene over the entire Brillouin zone.	19
Figure 1.8	Electron energy dispersion of graphene along the high symmetry directions.	19
Figure 1.9	Condition for obtaining a metallic or a semiconducting CNT.	20
Figure 1.10	Condition for obtaining a metallic or a semiconducting zigzag $(n,0)$ CNT.	22
Figure 1.11	Categorization of CNTs based on the physical structure.	22
Figure 1.12	Lowest few conduction subbands for CNTs (a) (10,0), and (b) (14,0) with and without the curvature effect.	28
Figure 1.13	Lowest seven conduction subbands for CNT (49,0).	29
Figure 1.14	(a) The effective mass of the lowest subbands for CNTs, $(3p+1,0)$ and $(3p+2,0)$. (b) The normalized effective mass difference of the lowest three subbands for the two zigzag CNT families.	30
Figure 1.15	Brillouin zone for a zigzag (5,0) semiconducting CNT superimposed on graphene k-space.	34
Figure 1.16	(a) LO and (b) LA phonon dispersion for (10,0) CNT by zone folding the LA and LO phonon modes of graphene.	36

Figure 2.1	Monte Carlo method applied to the charge transport simulation of bulk semiconductor materials.	44
Figure 2.2	Illustration of the algorithm used to determine the final electron state after scattering. (a) The initial electron position, k_i . (b) The phonon branch involved in the electron scattering. (c) An absorption process with the final two possible electron k vectors and the phonon q vectors.	49
Figure 2.3	Algorithm implemented to evaluate q and k_f based on Figure 2.2.	52
Figure 2.4	(a) Equilibrium momentum, and (b) energy distributions for CNT (10,0) at 300K.	55
Figure 2.5	Algorithm for a drift-scattering cycle within the Monte Carlo CNT bulk simulator.	58
Figure 3.1	Lowest subbands scattering rates versus energy for (a) CNT (10,0) and (b) CNT (49,0) at 300K.	62
Figure 3.2	Lowest subband scattering rates for (a) CNT(10,0) and (b) CNT(49,0) at 300K. Scattering rates are depicted versus k directed along the tube axis.	63
Figure 3.3	Average electron drift steady-state drift velocity as a function of electric field for CNT (10,0) and (11,0) at 300K.	65
Figure 3.4	Variation of the electron mobility with electric field for CNTs (10,0) and (11,0).	66
Figure 3.5	Steady-state momentum distribution for CNT (10,0) at various electric fields.	68
Figure 3.6	Electron occupancy of various subbands as a function of electric field for (a) CNT (10,0), (b) CNT (11,0), and (c) CNT (49,0).	71
Figure 3.7	Steady-state electron velocity versus electric field for various CNTs encompassing a broad range of diameter, at 300K.	72
Figure 3.8	Effect of temperature on steady-state electron velocity for (a) CNT (10,0), and (b) CNT (50,0).	74
Figure 3.9	Total electron-phonon scattering rates for CNT (10,0) at 100K and 300K.	76

Figure 3.10	Effect of LO phonon scattering for CNT (10,0) on (a) steady-state velocity, and (b) electron occupancy.	77
Figure 3.11	Velocity versus applied field for (a) CNT (10,0), and (b) CNT (11,0) with and without RBM scattering.	78
Figure 3.12	Low field mobility as a function of temperature and n .	82
Figure 3.13	Effect of RBM scattering on low field mobility. (a) RBM scattering causes a degradation of mobility, but (b) the relative difference is essentially independent of tube diameter.	83
Figure 3.14	Evolution of the average transient velocity with time for CNT (49,0) at various electric fields and 300K.	85
Figure 3.15	Evolution of the electron momentum distribution function with time for CNT (49,0) at 5 kV/cm and 300K.	87
Figure 3.16	Average transient drift velocity versus distance at 5 kV/cm and 10 kV/cm for CNT (49,0) at 300K.	89
Figure 3.17	Transient velocity response versus time for various CNTs at 300K.	90
Figure 3.18	Effect of LO scattering on the average transient velocity for CNT (49,0) at 300K at (a) 5 kV/cm and (b) 1 kV/cm.	92
Figure 3.19	Effect of LA and RBM scattering on the transient velocity oscillations for CNT (49,0) at 300K at (a) 5 kV/cm and (b) 1 kV/cm.	93
Figure 3.20	Effect of temperature on the transient velocity for CNT (49,0) at 5 kV/cm.	94
Figure 3.21	Average electron distance traveled versus time for CNT (49,0) at 300K and various electric fields.	96
Figure 3.22	Variation of the average electron distance versus time across various CNTs at 300K.	97

SUMMARY

The purpose of the research presented in this thesis is two-fold. In general, the research work aims to investigate the feasibility of semiconducting carbon nanotubes (CNTs) for future nano-electronic applications. In particular, the research is focused towards investigating the charge transport properties in these novel materials and determining data that will be of tremendous importance in applications.

The method employed for these purposes is the semi-classical Monte Carlo simulation. Various semiconducting zigzag $(n,0)$ CNTs, with wide-ranging diameters, were individually simulated towards this end. The bases for the Monte Carlo simulations are electronic structure calculations in the framework of a tight binding model. The principal scattering mechanism considered is due to the electron-phonon interaction. The phonons include longitudinal acoustic (LA), longitudinal optical (LO), and radial breathing mode (RBM). From the ensemble Monte Carlo simulation we determine the evolution of the electron distribution function as a function of position and time.

Since the envisioned switching time for devices utilizing CNTs is very short, both steady-state and transient phenomena are explored. In the steady-state domain, results show very high low-field mobility and average drift velocity, which increase with tube diameter. In the transient domain, transient velocity results show a behavior not observed in traditional 3-D semiconductors. This behavior is attributed to the limited phase-space available for scattering, resulting in electrons participating in streaming motion. Ballistic distance is also explored through a proposed elegant model. The ballistic distance values

obtained for various CNTs are in close agreement with recently reported experimental results.

Through the Monte Carlo simulation, various factors that affect charge transport in a CNT, both externally (electric field, temperature), and internally (role played by individual phonons - LA, LO, RBM), are explored in-depth. Through the simulation results, a very graphic and vivid picture of charge transport in these low dimensional materials emerges. The results presented help to determine the device speeds that may be expected, and support the potential of semiconducting carbon nanotubes for high-speed electron device applications.

CHAPTER 1

Introduction

1.1 History of the problem

Carbon nanotubes (CNTs) are currently being advertised as the flagship materials that are a harbinger of the age of nanotechnology. CNTs were first discovered in 1991 [1], and since then they have been utilized in such divergent fields as nano-electronics, to tires in automobiles, to the garment industry, and the pharmaceutical industry [2]. This is not only because of their promising electrical properties, but also because they are considered to be mechanically the strongest known material, and chemically very stable. CNTs may be considered to be sheets of graphene (two dimensional, or 2-D graphite sheets) rolled into hollow tubes [3]. The diameter of a tube is on the scale of nanometers - and hence the term carbon nanotube. If the aspect ratio (i.e. length of tube/diameter of tube) is high, we obtain a pseudo 1-D structure. Based on how the carbon atoms are arranged with respect to the axis of the tube, a vast number of unique CNTs are possible with wide ranging properties. CNTs thus represent a class of nano-scale materials.

There are two broad categorizations of CNTs possible in terms of the physical structure. If the tube is mono-atomic, i.e., the surface (and the tube itself) is composed of a single layer of carbon atoms, we have a structure known as the single wall carbon nanotube (SWCNT). Because of certain fabrication procedures, however, CNTs obtained

will more than likely have more than one layer of carbon atoms. Such a structure may be viewed as a multi-walled carbon nanotube (MWCNT), where two or more CNTs are co-axially aligned. In Figure 1.1 we can see an illustration of two SWCNTs that share the same axis, resulting in a MWCNT structure.

In terms of the electrical response, CNTs may either be metallic or semiconducting. CNTs have shown to have the potential to be basic building blocks of future nano-scale electronic and optoelectronic devices and circuits, and have been used in elementary logic circuits, and as optical emitters and detectors [5,6,7,8,9,10]. Thus it is possible to have a complete integrated circuit composed of logic gates and interconnects fabricated entirely of CNTs. An example of an electronic application utilizing CNTs is shown in Figure 1.2. This figure shows a carbon nanotube field effect transistor (CNTFET). A CNTFET is similar in structure to that of a Si-MOSFET, except that the conducting channel is now a CNT in place of Silicon.

CNTs were first fabricated by Iijima in 1991 [1], using an arc-discharge evaporation of graphite. Since then various other methods have been developed for the synthesis of CNTs. These include [13]:

1. Laser vaporization
2. Thermal chemical vapor deposition
3. Plasma enhanced chemical vapor deposition
4. Vapor phase growth
5. Electrolysis

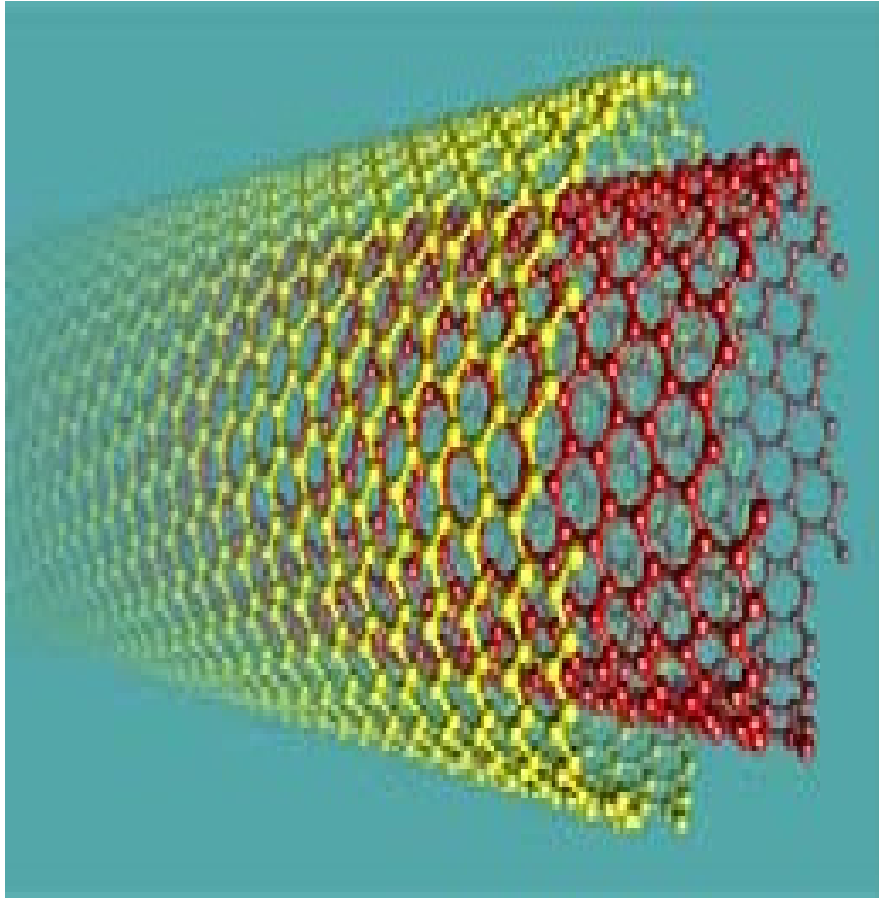


Figure 1.1: Illustration of a multi-walled CNT. Two single walled CNTs (red interior and yellow exterior) are seen to share the same axis. Such structures are very common in various CNT fabrication methods [figure from reference 4].

The first CNTs obtained were multi-walled, where each CNT was composed of SWCNTs ranging in numbers from 2 to about 50. Later on, the experimental synthesis of SWCNTs was reported simultaneously by two groups [14,15]. Subsequent introduction of better methods of synthesis provided better control over the physical structure of the

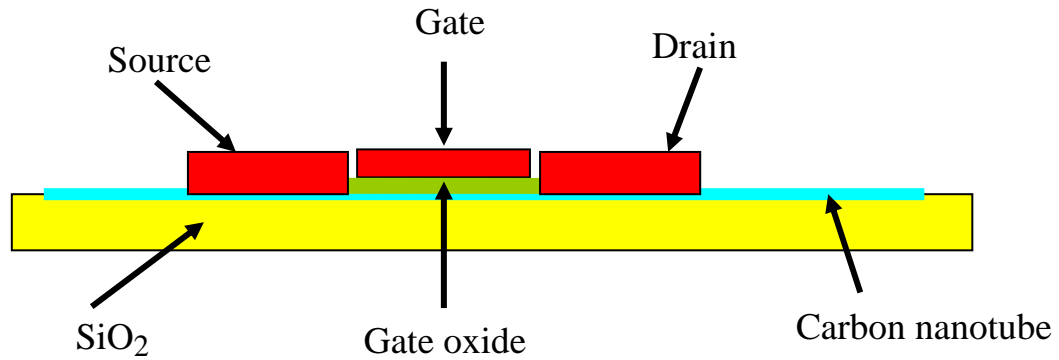


Figure 1.2: An illustration of a top-gated structure for a CNTFET [figure from reference 11]. Besides this, a bottom gate structure has also been fabricated, with the CNT lying on top of the gate, source and drain electrode. However, top-gated structures show superior performance and are easier to implement in a planar circuit design [12].

single-walled structures obtained, and the experimental characterization focus soon shifted from MWCNTs to SWCNTs. At the time of this writing, however, the controlled synthesis of individual CNTs with desired properties remains a challenge. In any synthesis process, a plethora of CNTs are usually obtained, with relatively wide ranging properties. This makes reproducibility, the backbone of success for an industrial assimilation of a semiconductor material, very difficult. Since there are large numbers of different types of CNTs, any experimental work involving them is therefore difficult and expensive. This makes it challenging to study the charge transport properties of a particular CNT, and extrapolate it to those of other CNTs. This essentially means that, given the charge transport data for one CNT obtained through experiments (example, low field mobility), it is not possible to predict similar data for other CNTs within the same

class, vis-à-vis, semiconductor or metallic, making the successful assimilation of CNTs in electronic applications even more challenging.

Theoretical focus on CNTs, unlike experimental focus, has almost always been on SWCNTs. Many researchers, including Saito and Dresselhaus [3,16], Ando [17], Lieber [18], and Mintmire and White [19] have made significant contributions towards a better understanding of the electronic behavior of CNTs. These contributions include (but are not limited to) the determination of the electronic band structure and phonon dispersion. This has allowed further research into various aspects of charge (electron and hole) transport in CNTs. Charge transport has been modeled numerically by drift-diffusion modeling [20], by the solution of the Boltzmann transport equation [21], by a Monte Carlo analysis [22,23,24], and by a more detailed quantum mechanical treatment [25].

All the above mentioned theoretical and numerical methods of modeling of charge transport in CNTs, however, have concomitant issues. The drift-diffusion and Boltzmann transport formulations have only a limited range of accuracy, while a quantum mechanical treatment usually is quite complex in terms of implementation, and is demanding on computing resources. A Monte Carlo analysis provides the best trade-off. However, the Monte Carlo studies of CNT charge transport behavior [22,23,24], have made various simplifying assumptions that make the results obtained only suggestive rather than an accurate depiction (a good example of the shortfall in the Monte Carlo analysis of CNTs is illustrated in reference 21). Moreover, all numerical studies of charge behavior in CNTs so far have focused exclusively on the steady-state domain. However, it is more than likely that CNTs will be utilized in electronic applications where electrons or holes do not have enough time to reach steady-state. Therefore, it is

extremely important to investigate the transient behavior of charge transport in CNTs in addition to steady-state. In addition, the theoretical and numerical studies conducted so far do little to investigate any correlation of charge transport properties across various CNTs, even though these studies are not hampered by the limitations, including financial, imposed on experimental studies [26,27,28].

1.2 Objective

Based on the discussion in the previous section, it is clear that the inability to predict accurately the electronic properties of CNTs prevents not only a deeper understanding of the behavior of charges (electrons and holes) within a CNT, but also proves to be a hindrance in the implementation of these materials in electronic applications. The work presented as part of this thesis attempts to overcome the above mentioned problems through detailed theoretical and numerical modeling of the charge transport properties of various semiconducting CNTs. As has been mentioned, numerical modeling circumvents the issues of fabrication of CNTs required to perform experiments. Moreover, a thorough understanding of the physics behind the behavior of charges may be obtained, which is difficult through experiments. By a skillful design of the numerical simulator, it is possible to reduce the time to investigate a wide range of CNTs with wide ranging diameters. This allows us to find a correlation in the charge transport properties across these CNTs, and predict data that are of extreme value to a device designer.

On a more fundamental level, because CNTs are currently being considered as the

leading candidate materials in future nano-electronic applications, it is important to discover the range, and fundamental limits, for which these materials can be used (in short, what may, or may not be expected from CNTs). Numerical and theoretical modeling makes this task easier [26,27,28].

In this work, the method of choice for numerical modeling of CNTs is primarily the semi-classical Monte Carlo algorithm, which includes the accurate numerically tabulated values of the band structure and phonon dispersion. Hence the results from the simulations are expected to be more accurately depictive of the actual behavior of charge carriers within the CNTs. As part of this, various facets of electron transport, for example steady-state, transient, temperature, and physical structure effects, are covered. The primary electron scattering mechanism is phonon-assisted. Results obtained not only demonstrate the viability of carbon nanotubes as basic building blocks for future nano-scale devices, but also provide useful data needed for these applications.

1.3 Overview of the Thesis

The objective of this research is to model various aspects of charge transport behavior of different semiconducting CNTs. In order to do that, it is first important to delve deeper into the physical structure of CNTs (section 1.4), and the effect it has on the electronic properties. Sections 1.5 and 1.6 not only investigate the work done so far towards the determination of the electronic band structure, but also outline further modifications that were made as part of this research. This includes the incorporation of

the curvature effect (details in section 1.6). Section 1.7 is devoted to the determination of the phonon dispersion in CNTs and includes a discussion of previous work, and the modifications and assumptions made as part of this work. Section 1.8 focuses on the electron-phonon interactions. The prescriptions for the electron-phonon scattering rates are evaluated based on the deformation potential theory and Fermi's Golden Rule (details in section 1.8).

Chapter 2 outlines the design and construction of the Monte Carlo algorithm utilized in this work. Contrast is also drawn with the highly simplified previously reported Monte Carlo models of semiconducting CNTs [22,23,24]. Contrast is also drawn to 3-D and 2-D Monte Carlo simulators for semiconductors.

Detailed results are presented in Chapter 3. Both steady-state and transient phenomena are explored in-depth, as are the effects of tube diameter and various external factors, such as temperature, on electron transport.

Chapter 4 provides a review and draws conclusions of the results obtained in Chapter 3. It also suggests directions that future research into the charge transport behavior of semiconducting CNTs may take.

1.4 Physical structure of carbon nanotubes

Since CNTs may be considered as rolled graphene sheets, it is only appropriate that various physical features and properties of CNTs be compared to graphene [3]. Figure 1.3, which is of an unrolled CNT unit cell, depicts various fundamental parameters

of a CNT, and their relationships to graphene. The chiral vector \mathbf{C}_h , as shown in Figure 1.3, is the primary vector that is used to describe the structure of a CNT. \mathbf{C}_h is perpendicular to the axis of the CNT, which is parallel to the vector \mathbf{T} . The magnitude of \mathbf{C}_h is equal to the circumference of the CNT, while \mathbf{T} connects the origin to the first equivalent site on graphene. By rolling the shaded portion of the figure parallel to the vector \mathbf{T} , such that \mathbf{T} and \mathbf{T}' overlap, we obtain a CNT unit cell.

\mathbf{C}_h can be broken down into vector components that are composed of the unit vectors of graphene. These unit vectors are depicted in Figure 1.3 as \mathbf{a}_1 and \mathbf{a}_2 . Subsequently, it is possible to express the chiral vector as [3]:

$$\mathbf{C}_h = n \mathbf{a}_1 + m \mathbf{a}_2 \equiv (n, m), \quad m \leq n \quad (1.1)$$

Here n and m are integers. Since a CNT is composed of complete hexagons on its surface, the atoms on one end of the boundary of an un-rolled CNT (for instance along \mathbf{T} in Figure 1.3), must be equivalent to atoms on the other end of the boundary (i.e., \mathbf{C}_h connects one lattice point on graphene to another). This condition requires that \mathbf{C}_h be the sum of integer multiples of the unit vectors of graphene, and hence n and m are integers. Moreover, the hexagonal symmetry means that we need consider only cases for which $m \leq n$. This may be easily deduced from the fact that $(n, 0)$ is equivalent to $(0, n)$. Once n and m are known, the diameter of a CNT may be readily obtained by the prescription:

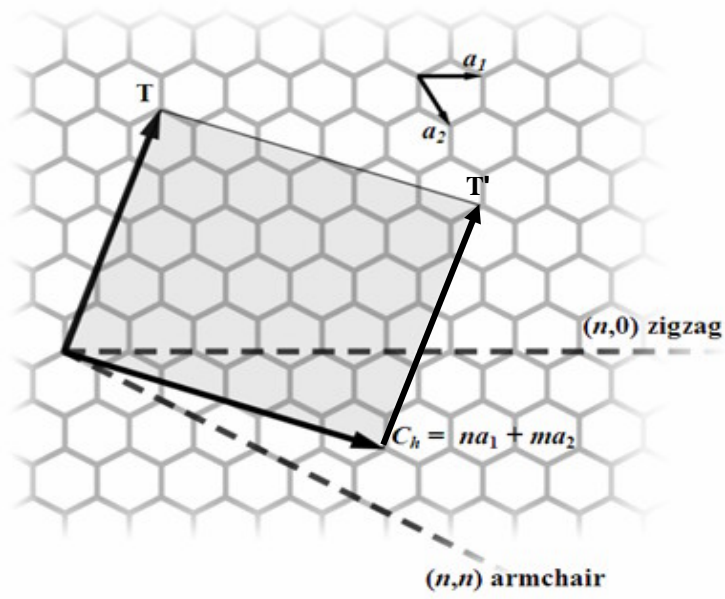


Figure 1.3: Fundamental parameters of a CNT, and relationship of those parameters to those of graphene. Vector T defines the axis of the CNT, while C_h , the vector perpendicular to T and along the circumference of the CNT is called the chiral vector. a_1 and a_2 are unit vectors of the graphene sheet [figure from reference 29].

$$d = \frac{|C_h|}{\pi} \quad (1.2)$$

Based on the chiral vector C_h , which, according to the description above, describes the orientation of carbon hexagons with respect to the axis of the CNT, three distinct classes of CNTs are possible [3]. Two of the CNTs, armchair and zigzag, are called achiral, or symmorphic, because their mirror image has an identical structure to the original one. The other is called chiral, or non-symmorphic. An armchair CNT is defined to be one where $n = m$, or $C_h \equiv (n, n)$. A zigzag nanotube is one where $m = 0$, or $C_h \equiv$

$(n,0)$. These two are the only two classes of achiral CNTs. A chiral CNT has a chiral vector as (n,m) where $m \neq 0$ and $m < n$. These three distinct CNTs are depicted in Figure 1.4. The vector \mathbf{T} is the unit vector for a CNT (\mathbf{C}_h is not a CNT unit lattice vector. Since a CNT is a pseudo 1-D structure, it can have only one unit vector [30]). This vector is parallel to the CNT axis and perpendicular to \mathbf{C}_h . It may also be expressed in terms of the vectors \mathbf{a}_1 and \mathbf{a}_2 as:

$$\mathbf{T} = t_1 \mathbf{a}_1 + t_2 \mathbf{a}_2 \equiv (t_1, t_2) \quad (1.3)$$

where t_1 and t_2 are integers. As was mentioned above, \mathbf{T} connects the origin to the first equivalent site on graphene (a lattice point), therefore t_1 and t_2 do not have a common divisor except for unity. Simple rules of vector algebra may be used to determine the relationship among n , m , t_1 and t_2 [3].

As mentioned, and depicted in Figure 1.3, the unrolled unit cell for a CNT is given by the rectangle formed by the vectors \mathbf{C}_h and \mathbf{T} . The number of hexagons in a unit cell for a CNT, denoted by N , is obtained simply from the vector cross-product of \mathbf{C}_h and \mathbf{T} (the area of the 2-D unit cell for a CNT) divided by the cross-product of \mathbf{a}_1 and \mathbf{a}_2 (area of a hexagon). Since there are two carbon atoms per hexagon, the number of carbon atoms per unit cell is $2N$.

In addition to the above, we may also define an angle θ , called the chiral angle [3]. It is obtained through the dot product of \mathbf{C}_h and \mathbf{a}_1 , and represents, as an angle, the tilt of the hexagons with respect to the axis of the CNT. In particular, for armchair

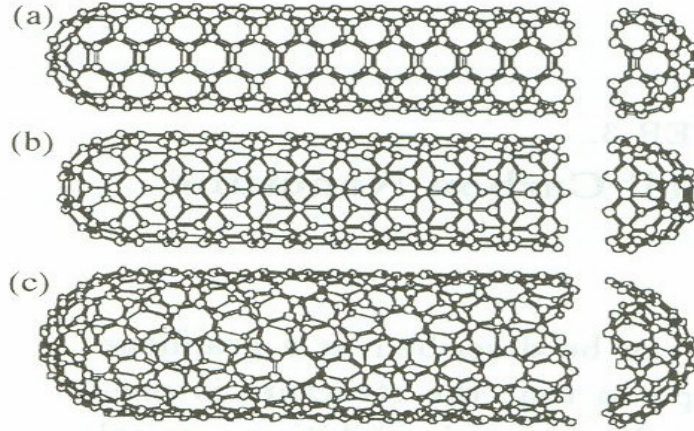


Figure 1.4: Three distinct carbon nanotubes: a. armchair, b. zigzag, and c. chiral. An armchair like structure may be inferred from the cross-section in (a), while (b) clearly shows a zigzag structure. The cross-section in (c) demonstrates no such order [figure from reference 3].

CNTs, $\theta = 30^\circ$ and for zigzag CNTs, $\theta = 0^\circ$.

1.5 Brillouin zone for a CNT

The general relationship between a direct lattice vector, \mathbf{a}_i , and reciprocal lattice vector, \mathbf{b}_j , is given by [30]:

$$\mathbf{a}_i \bullet \mathbf{b}_j = 2\pi\delta_{ij} \quad (1.4)$$

Here δ_{ij} is the well known Kronecker delta function defined such that [30]:

$$\delta_{ij} = \begin{cases} 1 & \text{if } i = j \\ 0 & \text{if } i \neq j \end{cases} \quad (1.5)$$

Thus for a graphene unit cell, if \mathbf{a}_1 and \mathbf{a}_2 are direct lattice vectors, we may define two indirect or reciprocal lattice vectors \mathbf{b}_1 and \mathbf{b}_2 . Figure 1.5 shows the four vectors. Now, the length of a reciprocal lattice vector is given by:

$$|\mathbf{b}_i| = \frac{2\pi}{|\mathbf{a}_i|} \quad (1.6)$$

Similarly if vectors \mathbf{C}_h and \mathbf{T} define a CNT unit cell in 2-D (Figure 1.3), then we may assign two associated reciprocal vectors \mathbf{K}_1 and \mathbf{K}_2 respectively. These vectors are given by:

$$\mathbf{K}_1 = \frac{2\pi}{|\mathbf{C}_h|^2} \mathbf{C}_h; \text{ and,} \quad (1.7)$$

$$\mathbf{K}_2 = \frac{2\pi}{|\mathbf{T}|^2} \mathbf{T}$$

Thus \mathbf{K}_1 and \mathbf{K}_2 define a CNT reciprocal unit cell in 2-D. It is also clear from the definition of \mathbf{K}_1 and \mathbf{K}_2 that the larger the CNT unit cell, the smaller the 2-D reciprocal unit-cell. For a CNT, only \mathbf{K}_2 is the reciprocal lattice unit vector, corresponding to a single

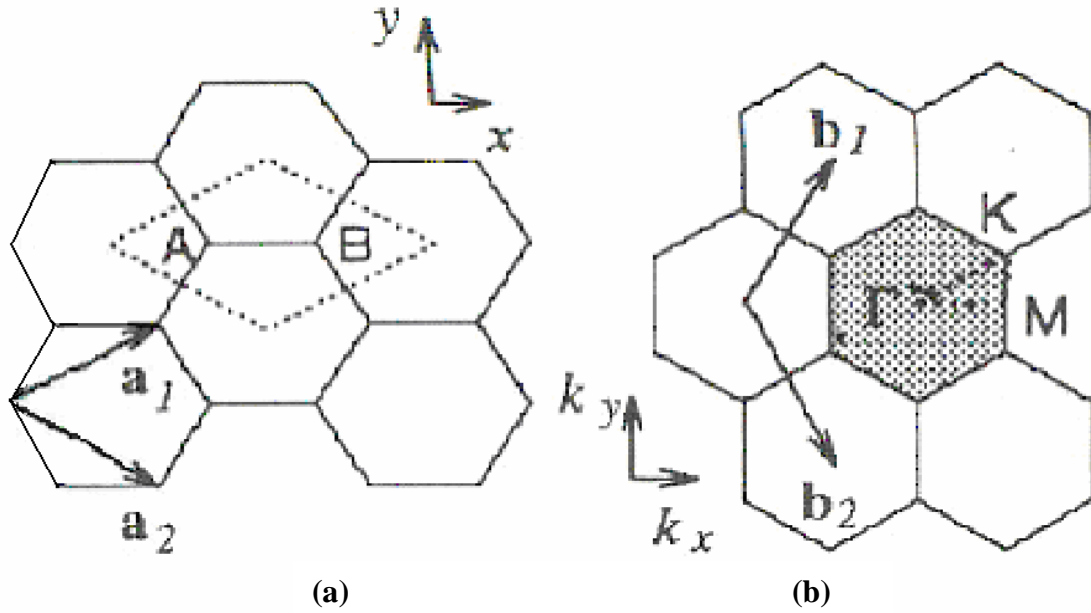


Figure 1.5: Direct (a), and indirect (b) lattice structure of graphene. Two atoms, A and B, define the unit cell with unit vectors a_1 and a_2 . b_1 and b_2 are the reciprocal unit lattice vectors. The high-symmetry Γ , K, and M points are also depicted in the reciprocal lattice structure [figure from reference 3].

direct lattice vector, as mentioned previously.

The above picture is, however, not complete. In a CNT, the vector C_h actually folds onto itself, thus imposing periodic boundary conditions on the wave function. This means that only certain values of the component of wave vector \mathbf{k} , parallel to \mathbf{K}_I , are allowed. Consider the electron wave function for graphene:

$$\psi(\mathbf{x}) = e^{i\mathbf{k} \cdot \mathbf{x}} u(\mathbf{x}) \quad (1.8)$$

where $\mathbf{u}(\mathbf{x})$ is the Bloch function that contains the periodicity of the lattice [30]. Now by imposing periodic boundary conditions on the wave function we imply that any translation by a distance in multiples of $|\mathbf{C}_h|$, and in the direction of \mathbf{C}_h , on the graphene lattice should result in the same wave function. Therefore,

$$\mathbf{k} \cdot \mathbf{C}_h = 2\pi\nu, \quad (1.9)$$

where ν is in integer. Expanding out the above equation in components of k_x and k_y , we obtain a linear relationship between k_x and k_y . Therefore the application of periodic boundary conditions on \mathbf{C}_h results in the appearance of discrete lines in the CNT Brillouin zone (BZ) that represent the allowed values of k_x and k_y and satisfy Equation 1.9. These lines are continuous along the \mathbf{K}_2 direction. The distance between each parallel line along the \mathbf{K}_1 direction is $2\pi/|\mathbf{C}_h|$.

The next step in determining the Brillouin zone for a CNT is to determine the restriction on the integer ν , if any. Since any point outside of the first Brillouin zone of graphene is equivalent to any point within the zone, we obtain [19]:

$$\nu = \frac{\text{graphene reciprocal unit cell area}}{|\mathbf{K}_1 \times \mathbf{K}_2|} = N \left(\equiv \text{Number of hexagons in CNT unit cell} \right) \quad (1.10)$$

These N lines (0 to $N-1$, or $-\left(\frac{N}{2}+1\right)$ to $\frac{N}{2}$) represent the extended zone scheme for a CNT. This is depicted in Figure 1.6, which shows the Brillouin zone for a chiral (4,2) CNT

superimposed on the graphene reciprocal lattice [3].

Since a CNT is essentially a 1-D material, each line segment can be translated to the $K_I=0$ line, resulting in a reduced zone scheme. This is called the zone folding method.

1.6 Electronic band structure of carbon nanotubes

The electronic band structure of a CNT depends very strongly on its diameter and chirality (i.e. chiral vector). CNTs may be metallic or semiconducting. Even within the broad category of semiconducting CNTs, vastly different properties are exhibited by different CNTs. The simplest way to obtain the band structure of a CNT is to start from the band structure of the graphene sheet. In this section we first discuss the method to obtain the band structure of a CNT from a simple zone-folding scheme of the π -electron band structure of graphene. Then we discuss a modification to this scheme that forms a basis for our work.

1.6.1 Band structure of 2-D graphite

The π -electron band structure for graphene may be obtained from the application of the tight-binding (TB) method [3]. Figure 1.5, as mentioned previously, shows the direct lattice structure (a), and reciprocal or indirect lattice structure (b) of graphene. Vectors \mathbf{a}_1 and \mathbf{a}_2 define the unit cell, and \mathbf{b}_1 and \mathbf{b}_2 define the reciprocal unit cell. The symmetry points, Γ , \mathbf{K} , and \mathbf{M} , in the reciprocal lattice are also depicted. By considering the π orbital overlap between the A and B atoms to be zero (i.e. no overlap), one obtains a

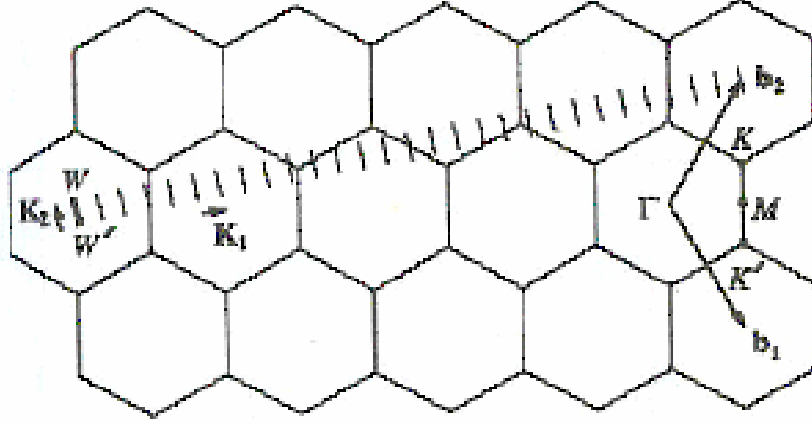


Figure 1.6: Extended reciprocal zone for CNT (4,2) superimposed on the graphene reciprocal lattice. 28 discrete bands are observed corresponding to the 28 hexagons in CNT (4,2). The 29th band of the CNT is equivalent to the 1st band [figure from reference 3].

tight-binding (TB) formulation of the band structure as [3]:

$$e(\mathbf{k}) = \pm \gamma_0 \sqrt{1 + 4\cos^2\left(\frac{k_y a}{2}\right) + 4\cos\left(\frac{k_y a}{2}\right)\cos\left(\frac{\sqrt{3}k_x a}{2}\right)} \quad (1.11)$$

In the equation, γ_0 is the nearest-neighbor transfer integral, also called the hopping matrix element, a is the lattice constant for the graphene direct lattice structure, and e is the electron energy.

Figure 1.7 shows an illustration of the energy dispersion for graphene over the entire Brillouin zone (BZ). This intersection gives rise to the semi-metallic nature of graphene. If we do not consider the overlap to be zero, we obtain an asymmetric band

structure around the Fermi level. This is depicted in Figure 1.8, which shows the band structure of graphene along the high symmetry directions.

1.6.2 Band structure of carbon nanotubes

As was mentioned in the previous section, periodic boundary conditions imposed by the chiral vector C_h cause the wave vector K_1 , which is associated with C_h , to be quantized in a CNT, while the wave vector K_2 , which is associated with the vector T , remains continuous. This gives rise to a set of k vectors that are parallel to T . These k vectors will result in cross-sections of the graphene electron dispersion. These cross-sections result in the appearance of various subbands in a CNT. The band structure is obtained along the K_2 vector.

Since the graphene conduction and valence bands intersect at the high symmetry K points (Figures 1.7 and 1.8), if a CNT band line in the extended zone scheme (Figure 1.6) also intersects a graphene K point, the CNT will exhibit metallic properties. However, if the band lines do not intersect any graphene K point, a band gap appears in the CNT band structure, resulting in semiconducting properties. Figure 1.9 illustrates the condition for obtaining metallic versus semiconducting CNTs. If the vector YK is an integer multiple of vector K_1 , we will have a CNT band line intersecting the graphene K point. This is because, in the extended zone scheme, CNT band lines are spaced $|K_1|$ apart. However a case in which YK is a non-integer multiple of K_1 does not correspond to a CNT band line, and the CNT will be semiconducting. In general [3],

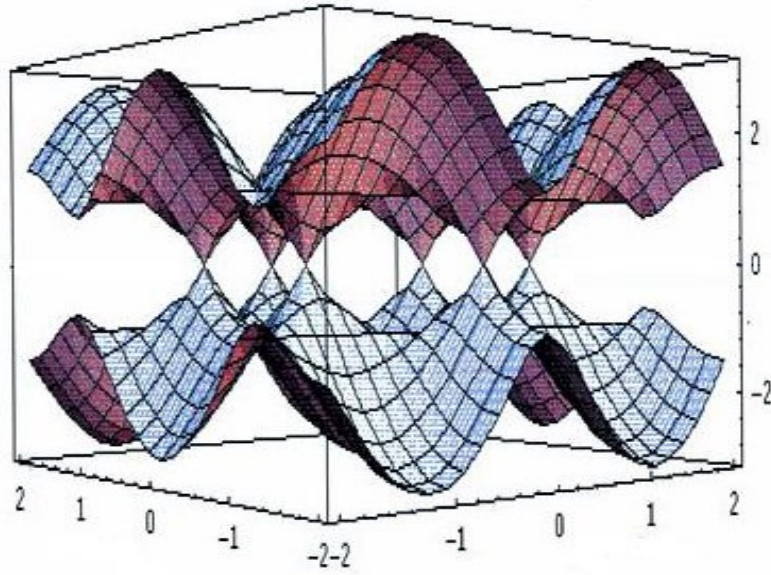


Figure 1.7: Illustration of the electron energy dispersion of the π and π^* orbitals for graphene over the entire Brillouin zone [figure from reference 31]. The π and π^* bands are seen to meet at the six high symmetry K points, giving rise to the metallic nature of graphene. The overlap integral is considered to be zero.

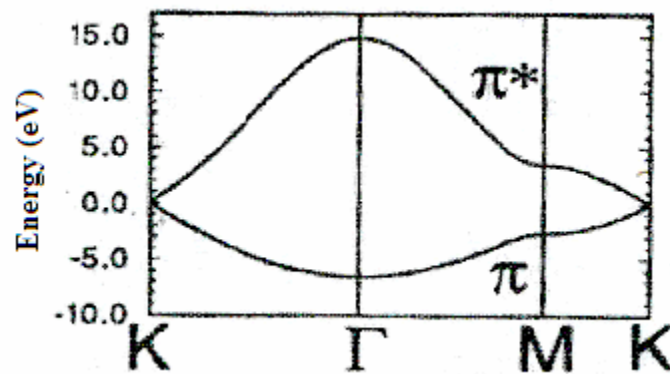


Figure 1.8: Electron energy dispersion of graphene along the high symmetry directions [figure from reference 3]. The overlap integral is non-zero.

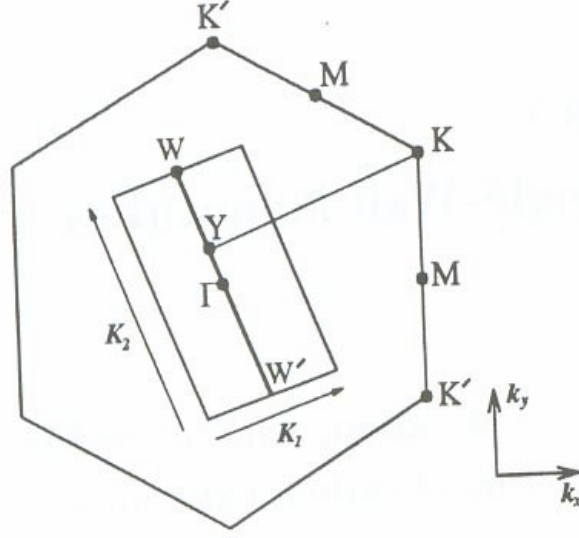


Figure 1.9: Condition for obtaining a metallic or a semiconducting CNT. When $|YK|$ is an integer multiple of $|K_I|$, a subband of CNT intersects the graphene K point, resulting in a metallic CNT [figure from reference 3]. The points K and K' are equivalent.

$$\mathbf{YK} = \frac{2n+m}{3} \mathbf{K_I} \quad (1.12)$$

and therefore if $n - m$ (n minus m) is a multiple of 3, the CNT (n,m) will be metallic. If $n - m$ is not a multiple of 3, the CNT will be semiconducting. Let us look at the example of a zigzag $(n,0)$ CNT. If we rotate our \hat{k}_x and \hat{k}_y axis so that $\mathbf{K_I}$ vector is in the direction of \hat{k}_y we obtain a layout as depicted in Figure 1.10. Using Equations 1.1 and 1.9, we find

that \mathbf{K}_I in this case is simply given by $\frac{2\pi}{na}\hat{\mathbf{k}}_y$. Since the distance from the Γ point to the

\mathbf{K} point is $\frac{4\pi}{3a}$, we obtain the relationship:

$$\mathbf{YK} = \frac{2n}{3}\mathbf{K}_I \quad (1.13)$$

From Equations 1.12 and 1.13 it is clear that, for example, CNT (9,0) will be metallic while CNT (10,0) will be semiconducting. Also, all armchair CNTs (n,n) are metallic.

Figure 1.11 broadly depicts the physical categorization of CNTs based on the discussion so far. The research work, and results presented in this thesis, focuses on semiconducting zigzag ($n,0$) CNTs.

From the above discussion, it is also evident that to obtain the band structure for a CNT, we simply obtain allowed CNT Brillouin zone \mathbf{k} vectors and obtain the associated energy for each \mathbf{k} from the graphene band structure. This results in the following prescription [3]:

$$e_\nu(\mathbf{k}) = e_{\text{graphene}}\left(\left|\mathbf{k} \mid \frac{\mathbf{K}_2}{|\mathbf{K}_2|} + \nu\mathbf{K}_I\right), \nu = -\left(\frac{N}{2} + 1\right) \dots \frac{N}{2}, \text{ and } -\frac{\pi}{|\mathbf{T}|} < \mathbf{k} < \frac{\pi}{|\mathbf{T}|}\right) \quad (1.14)$$

where $k = |\mathbf{k}|$. N pairs of subbands are obtained corresponding to the π and π^* orbitals.

This can be inferred from Figures 1.7 and 1.8, where each vector $\left|\mathbf{k} \mid \frac{\mathbf{K}_2}{|\mathbf{K}_2|} + \nu\mathbf{K}_I\right.$ “cuts”

the energy dispersion above and below the Fermi level.

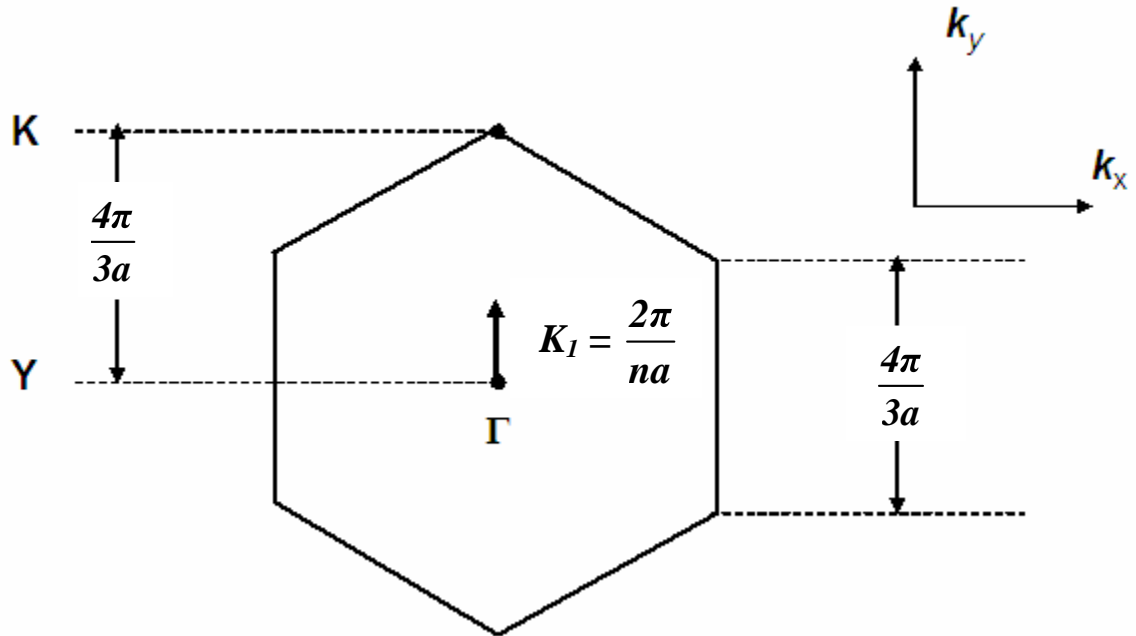


Figure 1.10: Condition for obtaining a metallic or a semiconducting zigzag $(n,0)$ CNT. If n is a multiple of 3, one obtains a metallic CNT. For all other n , the CNT is semiconducting.

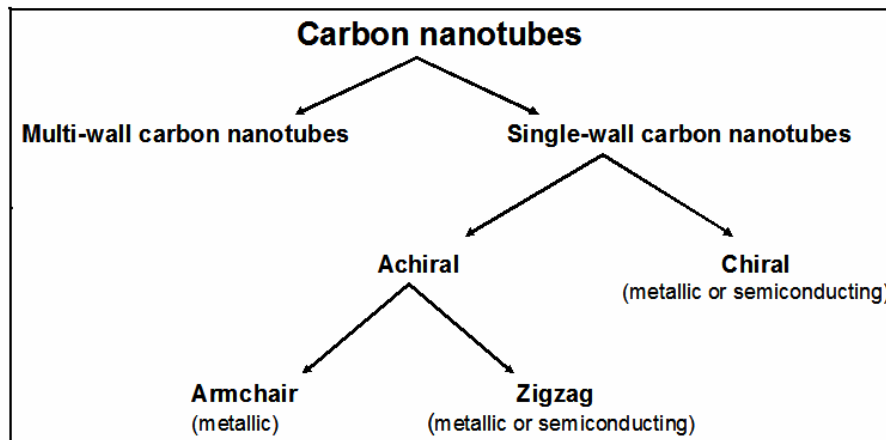


Figure 1.11: Categorization of CNTs based on the physical structure. This work focuses on semiconducting zigzag CNTs.

For a zigzag CNT $(n,0)$, the expression is further simplified by the application of the periodic boundary condition on k_y in the expression for the band structure for graphene, Equation 1.11. Therefore:

$$k_y = \frac{2\pi\nu}{na}, \text{ where } \nu = -n+1, \dots, 0, \dots, n \quad (1.15)$$

where the quantum number ν represents the discrete values of allowed wave vectors in the circumferential direction. Therefore the energy dispersion for a zigzag CNT becomes [3]:

$$e_\nu(\mathbf{k}) = \pm \sqrt{\gamma_0^2 + 4\gamma_0^2 \cos^2\left(\frac{\pi\nu}{n}\right) + 4\gamma_0^2 \cos\left(\frac{\pi\nu}{n}\right) \cos\left(\frac{\sqrt{3}|\mathbf{k}|a}{2}\right)}, \quad (1.16)$$

$$\left(\frac{-\pi}{\sqrt{3}a} \hat{\mathbf{k}} \leq \mathbf{k} \leq \frac{\pi}{\sqrt{3}a} \hat{\mathbf{k}} \right), \quad (-n+1 \leq \nu \leq n)$$

As can also be inferred from Equation 1.16, in addition to the spin degeneracy, the subbands are doubly degenerate for $\pm \nu$ except for subbands $\nu = 0$ and n . The vector \mathbf{k} is along the CNT axis.

The discussion so far regarding the CNT band structure is, however, not an accurate depiction. In a graphene sheet, all carbon-carbon (C-C) bond lengths may be considered to be of equal lengths, resulting in Equation 1.11, and subsequently Equation 1.16 for a zigzag CNT. However in a CNT, this is not the case. When a graphene sheet is rolled into a tube, the C-C bond lengths undergo a change to accommodate the curvature

of the tube. The effect of the curvature is incorporated by allowing for two different effective bond lengths, distinguishing the bond parallel to the CNT axis from the zigzag bonds [32,33]. Based on *ab initio* electronic structure calculations, the following empirical relation for the bond lengths has been reported: $d_1 = d_2 = d_0 + s_1/d^2$ and $d_3 = d_0 + s_3/d^2$, where $s_1 = 0.427 \text{ \AA}^3$, $s_3 = -0.320 \text{ \AA}^3$. The bond length d_3 is along the tube axis, whereas d_1 and d_2 are in the other directions; $d_0 = 1.406 \text{ \AA}$ is the C-C bond length of graphene, and d is the diameter of the tube [34]. For a particular CNT the diameter can be calculated using a relationship as provided in reference 34. However, in this work only the lowest order curvature correction is considered, and the diameter for a $(n,0)$ CNT is approximated by, $d = \sqrt{3}d_0n/\pi$. This approximation introduces less than 0.2% error in the diameter for CNT (10,0) and becomes negligible for larger diameter CNTs. The above bond length relationship and the universal TB scaling scheme are then used to relate the two different hopping matrix elements for the TB calculations:

$$\gamma_1 = \gamma_2 = \bar{\gamma} \frac{d_0^2}{(d_0 + s_1/d^2)^2} \quad (1.17)$$

$$\gamma_3 = \bar{\gamma} \frac{d_0^2}{(d_0 + s_3/d^2)^2} \quad (1.18)$$

The hopping matrix element γ_3 corresponds to the bond parallel to the CNT axis, whereas γ_1 , and γ_2 correspond to the two zigzag bonds. In principle, $\bar{\gamma}$ is the hopping matrix

element for (planar) graphene.

Using two different hopping matrix elements, the 1-D dispersion relations of the lowest conduction subbands (+) and the top valence subbands (-) of an $(n,0)$ zigzag CNT in TB formulation become:

$$e_v(\mathbf{k}) = \pm \sqrt{\gamma_3^2 + 4\gamma_I^2 \cos^2\left(\frac{\pi\nu}{n}\right) + 4\gamma_I\gamma_3 \cos\left(\frac{\pi\nu}{n}\right) \cos\left(\frac{\sqrt{3}|\mathbf{k}|a}{2}\right)}, \quad (1.19)$$

$$\left(\frac{-\pi}{\sqrt{3}a} \hat{\mathbf{k}} \leq \mathbf{k} \leq \frac{\pi}{\sqrt{3}a} \hat{\mathbf{k}}\right), \quad (-n+1 \leq \nu \leq n)$$

where \mathbf{k} is the 1-D electron wave vector along the tube axis, and the quantum number ν represents the discrete values of allowed wave vectors in the circumferential direction. The length of a primitive lattice vector of graphene is given by $a = \sqrt{3}d_0$. In addition to the spin degeneracy, the subbands are doubly degenerate for $\pm \nu$, except for subbands $\nu = 0, n$.

Two types of semiconducting zigzag CNTs are possible depending on the location of the lowest energy subbands outside or inside of the \mathbf{K} -point of the graphene BZ. We group them as $n = (3p+1)$ and $n = (3p-1)$, where p is an integer. From Equation 1.19, and the condition that the lowest conduction subband and highest valence subband correspond to $\nu = (2n \pm 1)/3$, the energy gap is given by:

$$e_g = 2 \left| \gamma_3 + 2\gamma_I \cos\left(\frac{2\pi}{3} \pm \frac{\pi}{3n}\right) \right|, \quad (1.20)$$

where (+) and (-) signs are for the CNTs $(3p+1,0)$ and $(3p-1,0)$, respectively. The band gap can also be approximated from Equations 1.17, 1.18, and 1.20 by:

$$e_g = 2 \left| \mp \frac{d_0 \bar{\gamma}}{d} + \frac{d_0^2 \bar{\gamma}}{6d^2} + \frac{2\bar{\gamma}(s_1 - s_2)}{d_0 d^2} \right|, \quad (1.21)$$

where (-) and (+) signs are for the CNTs $(3p+1,0)$ and $(3p-1,0)$ respectively. Now, neglecting the curvature effect, i.e. setting $s_1 = s_2 = 0$, Equation 1.21 simplifies to

$$e_g = 2 \left| \mp \frac{d_0 \bar{\gamma}}{d} + \frac{d_0^2 \bar{\gamma}}{6d^2} \right| \quad (1.22)$$

The value of $\bar{\gamma}$ used for this work is extracted by fitting Equation 1.21 to experimental data reported in reference 18. The value of $\bar{\gamma}$ is found to be -2.85 eV, which gives the hopping matrix elements for CNT (10,0) of $\gamma_1 = \gamma_2 = -2.82$ eV and $\gamma_3 = -2.87$ eV. Similarly, the hopping matrix elements for the CNT (14,0) are found to be $\gamma_1 = \gamma_2 = -2.83$ eV and $\gamma_3 = -2.86$ eV. For comparison, Equation 1.22 is also fit to the same experimental data yielding $\bar{\gamma} = -2.53$ eV, which is similar to the value reported in reference 18. Further comparing Equations 1.21 and 1.22 for CNT (10,0), we find that the term of second order in $1/d$ is more than four times that obtained when curvature effects are neglected. Once the hopping matrix elements are known, we are ready to use Equation 1.19 to determine the band structure for the CNT. The lowest few conduction subbands for CNTs (10,0) and (14,0) are plotted in Figure 1.12 a and b. The solid lines

and dotted lines represent bands with the curvature effect ($\bar{\gamma} = -2.85$ eV) and without the curvature effect ($\bar{\gamma} = -2.53$ eV), respectively. The curvature effect decreases with tube diameter. This is intuitively clear because in the infinite diameter limit, the graphene structure is obtained where all C-C bonds have equal lengths [3].

From Equations 1.21 and 1.22 it is clear that with increasing tube diameter, the band gap between the lowest conduction and highest valence subband decreases. Within the conduction subbands, the intersubband energy difference also decreases with increasing diameter. This can be seen by comparing Figures 1.12a and 1.13, both of which show limited conduction band structures for CNTs (10,0) and (49,0) respectively.

1.6.3 Electron effective mass

The electron effective mass has tremendous influence on the transport properties. The effective mass is a measure of how much energy, and how quickly, electrons will gain from an applied electric field. Therefore effective mass essentially affects, to various extent, all transport characteristics of a semiconductor material.

The electron effective masses of the lowest conduction subbands for CNTs from (10,0) to (50,0) are plotted in Figure 1.14a. Instead of grouping the zigzag families as $(3p+1,0)$ and $(3p-1,0)$, we can, without loss of generality, group them as $(3p+1,0)$ and $(3p+2,0)$. This allows us easy grouping of the CNTs modeled in Chapter 3 to the two families. It can be seen that the electron effective mass is smaller for the $(3p+1,0)$ group compared to that of the $(3p+2,0)$ group for small diameter tubes. However, the effective masses become comparable for both groups for large diameters. Results presented in Chapter 3 show that this effect leads to a markedly different charge transport behavior for

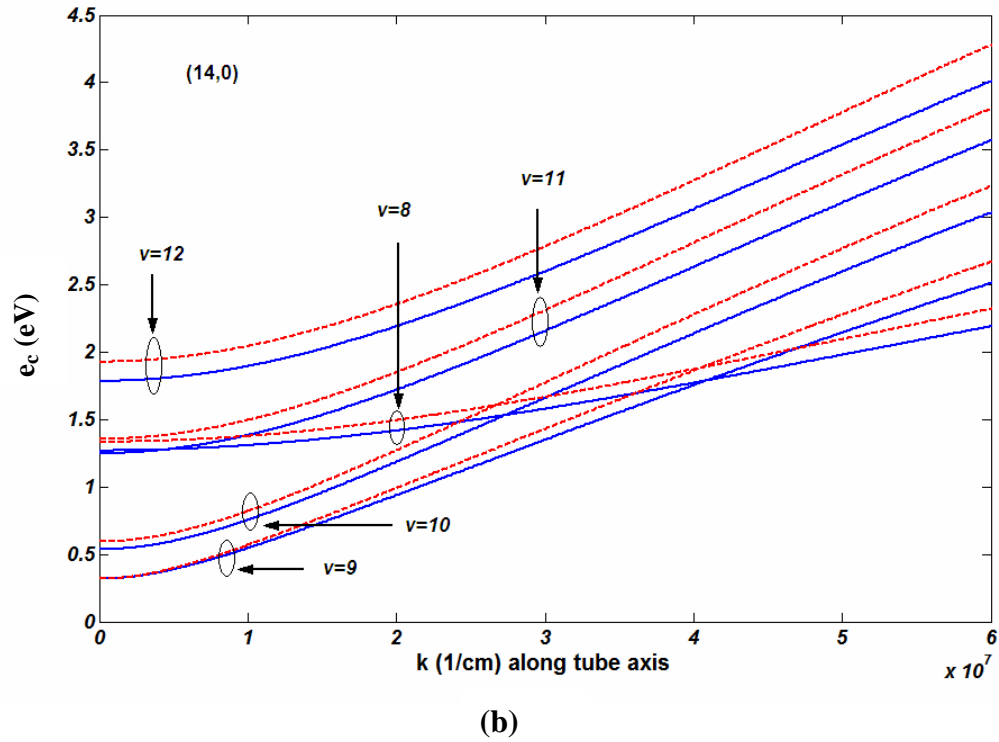
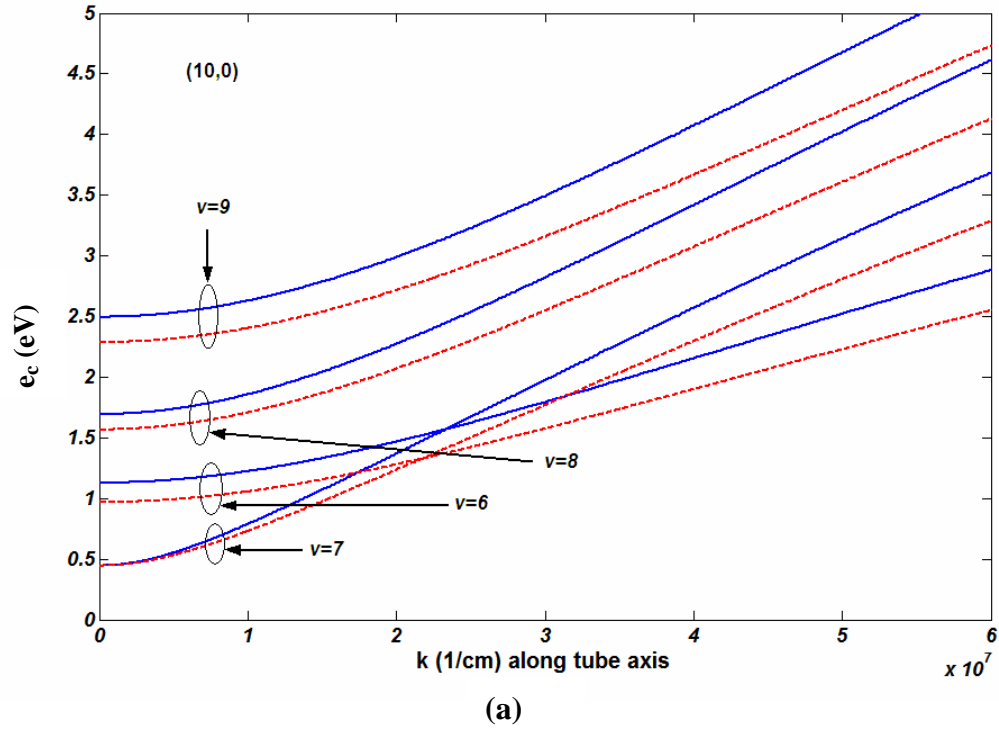


Figure 1.12: Lowest few conduction subbands for CNTs (a) (10,0), and (b) (14,0) with (solid blue lines) and without (broken red lines) the curvature effect. The curvature effect reduces with an increase in tube diameter.

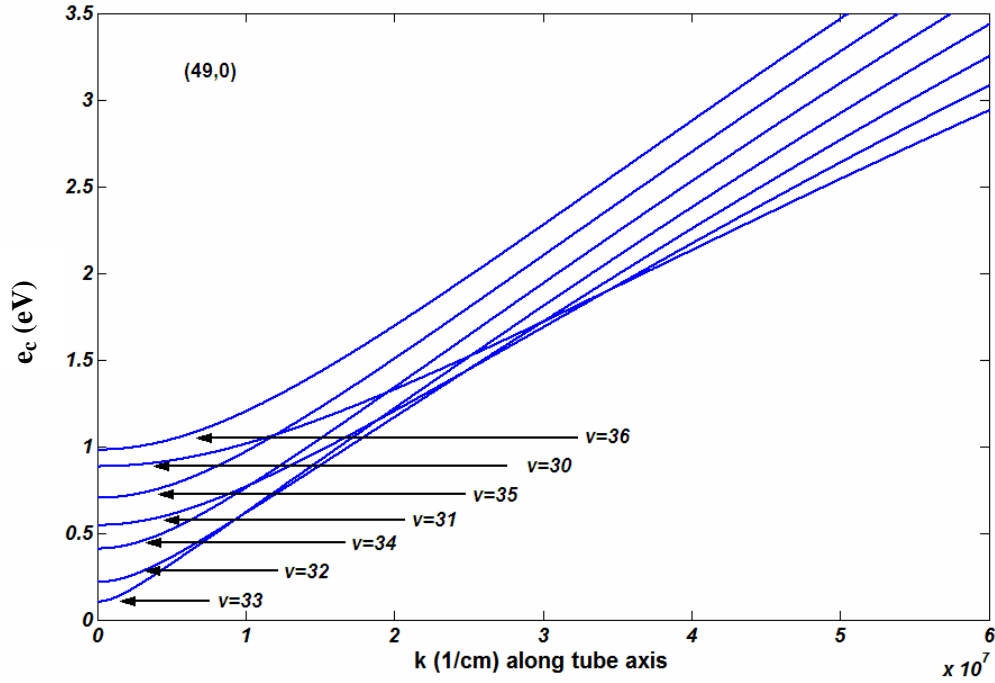


Figure 1.13: Lowest seven conduction subbands for CNT (49,0). Comparing with Figure 1.12, it can be noticed that with an increase in tube diameter, the band gap decreases, and subbands move closer to each other in energy.

the two families of CNTs. Figure 1.14b shows the normalized difference between the effective masses of the next higher energy subbands and the lowest subbands. A relatively large difference between the effective masses of the second and the lowest subbands is obtained for small diameter $(3p+1,0)$ CNTs compared to $(3p+2,0)$ CNTs. The difference becomes comparable for both families at large diameters. If the curvature correction is not incorporated in the determination of the band structure, there is a possibility of greatly overestimating the effective mass, particularly for smaller diameter CNTs. Without the curvature effect, the effective mass of electrons in the lowest subbands

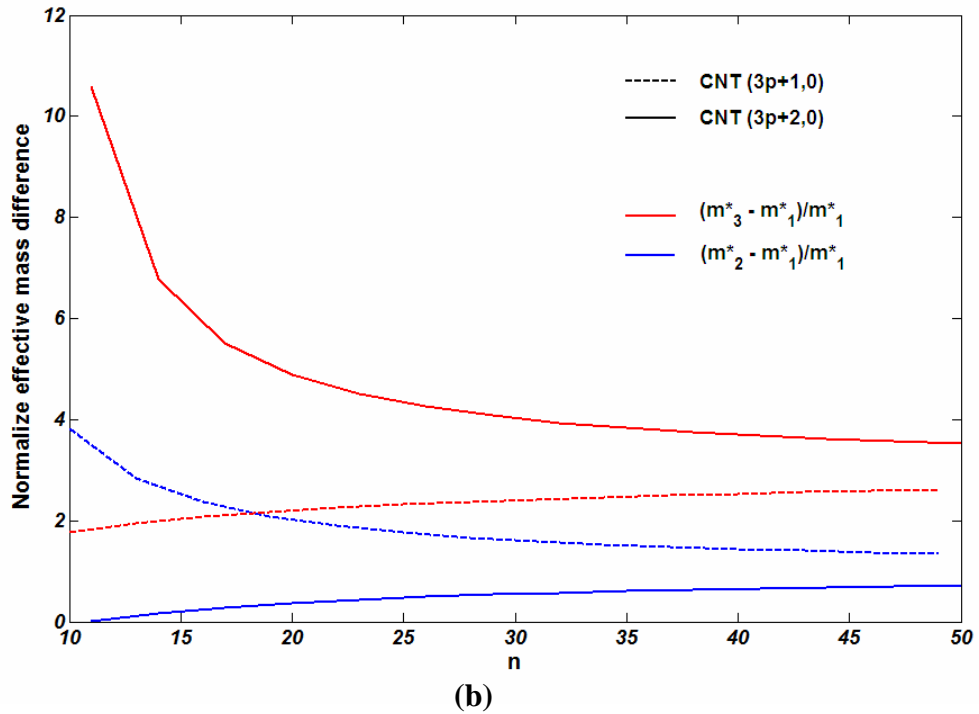
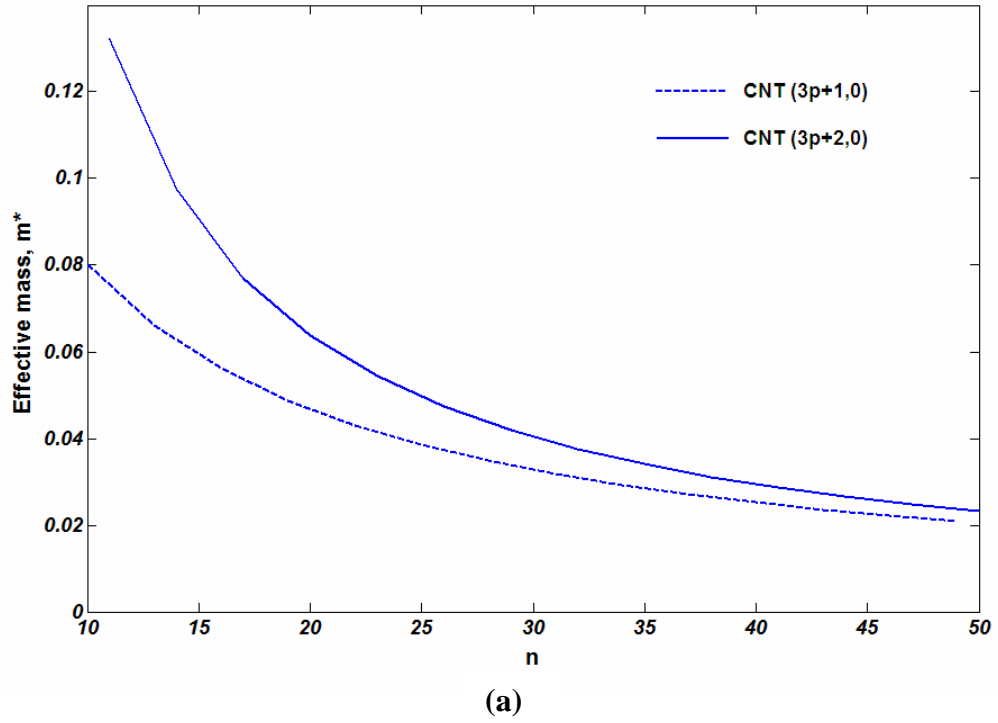


Figure 1.14: (a) The effective mass of the lowest subbands for CNTs, $(3p+1,0)$ and $(3p+2,0)$. CNTs $(3p+2,0)$ are seen to have a greater effective mass than CNTs $(3p+1,0)$ for the same p . (b) The normalized effective mass difference of the lowest three subbands for the two zigzag CNT families.

of CNTs (10,0) and (14,0) is overestimated by more than 25% and 5%, respectively.

1.7 Phonon dispersion

The phonon dispersion of a CNT may also be obtained by the application of zone-folding of the graphene phonon modes [3]:

$$e_p(\mathbf{q}, \mu) = e_p^{graphene} \left(\left| \mathbf{q} \right| \frac{K_2}{|K_2|} + \mu K_1 \right), \quad (1.23)$$

where $e_p(\mathbf{q}, \mu)$ denotes the energy of the phonon with wave vector \mathbf{q} , and μ denotes the branch index of the phonon (just as v denotes the electron subband in Equations 1.16 and 1.19). For zigzag $(n,0)$ CNTs, the phonon wave vectors are quantized in the circumferential direction as $q_x = 2\pi\mu/na$, where $-n+1 \leq \mu \leq n$, and the phonon wave vector, \mathbf{q} , along the tube axis assumes values, $-\pi/\sqrt{3}a \leq q_y = q \leq \pi/\sqrt{3}a$.

The above method however does not produce the phonon dispersion of a CNT in its entirety. One omission is the existence of Radial Breathing Mode (RBM) phonons that originate from transverse acoustic modes polarized perpendicular to the graphene sheet [3]. RBM phonons are perhaps among the most outstanding and unique features of SWCNTs. The RBM involves atoms on the surface of the CNT vibrating in the radial direction. The CNT thus appears to be “breathing in-and-out”. In recent experimental work these phonons were found to be the dominant phonon mode excited by electrons

tunneling into a SWCNT [35].

To get a complete picture of the phonon dispersion of a CNT, there is a need to directly evaluate the phonon dispersion of a CNT. This is done by constructing a dynamical matrix involving force-constant parameters and atomic interactions up to the fourth nearest neighbors [3]. Curvature of the tube is also taken into account.

Longitudinal acoustic (LA) and longitudinal optical (LO) phonons are the dominant modes in electron scattering in simple, undoped, non-polar semiconductors as well as in graphene. On this basis, along with the RBM phonons, LA and LO phonons, which are derived from the corresponding vibrational modes of graphene, are considered as the most important electron scattering mechanism in CNTs in this work. However in a CNT, longitudinal and transverse modes are generally coupled and the interaction of these coupled modes with electrons is rather complicated. Hence, for the work that forms this thesis, we simplify the phonons of the CNTs by fitting simple polynomials to the calculated dispersion curves of the LA and LO modes of graphene (neglecting coupling to the transverse modes). We then apply the zone folding scheme, Equation 1.23, to generate the corresponding CNT LA and LO phonons.

The phonon branches of the graphene LA and LO phonons are calculated by taking into account atomic interactions up to the fourth nearest-neighbors and then solving the 6X6 dynamical matrix with force constants determined by fits to experimental data [3]. Within the graphene BZ, the LA phonon dispersion is nearly rotationally invariant around the Γ -point, up to the M point. Beyond that radius the phonon energy is almost constant. As an illustrative example, Figure 1.15 shows the BZ for a zigzag (5, 0) semiconducting CNT superimposed on the graphene k -space. The graphene LA phonon

dispersion is rotationally invariant around each Γ -point within the inscribed circles (Regions 1 and 2), and the phonon energy is essentially constant in the shaded regions of the graph (Region 3). Therefore we model the LA phonon dispersion with a third order polynomial as follows:

$$e_p^{LA}(\mathbf{q}, \mu) = \begin{cases} \hbar \omega_m^{LA} + A_1(q_1 - q_m)^2 + A_2|q_1 - q_m|^3 & \text{Region 1} \\ \hbar \omega_m^{LA} + A_1(q_2 - q_m)^2 + A_2|q_2 - q_m|^3 & \text{Region 2} \\ \hbar \omega_m^{LA} & \text{Region 3} \end{cases} \quad (1.24)$$

The LA phonon energy at the \mathbf{M} -point and the length of the wave vector at the \mathbf{M} -point are $\hbar \omega_m^{LA} = 155.6 \text{ meV}$ and $q_m = 2\pi/\sqrt{3}a$, respectively. The velocity of sound in graphene is $v_s = 2.0 \times 10^6 \text{ cm} \cdot \text{s}^{-1}$. The parameters A_1 , A_2 , q_1 and q_2 may be expressed as,

$$A_1 = -\frac{1}{5} \left(\frac{\hbar v_s}{q_m} + \frac{3\hbar \omega_m^{LA}}{q_m^2} \right), \quad A_2 = \frac{1}{5} \left(\frac{\hbar v_s}{q_m^2} - \frac{2\hbar \omega_m^{LA}}{q_m^3} \right), \quad q_1 = \sqrt{\left(\frac{2\pi\mu}{na} \right)^2 + q^2}, \quad \text{and}$$

$$q_2 = \sqrt{\left(\frac{2\pi\mu}{na} - \frac{2\pi}{a} \right)^2 + (q - q_m)^2}, \quad \text{where } q = |\mathbf{q}|.$$

The LO phonons in graphene have similar symmetry (and much weaker dispersion) and are well described by a fifth order polynomial:

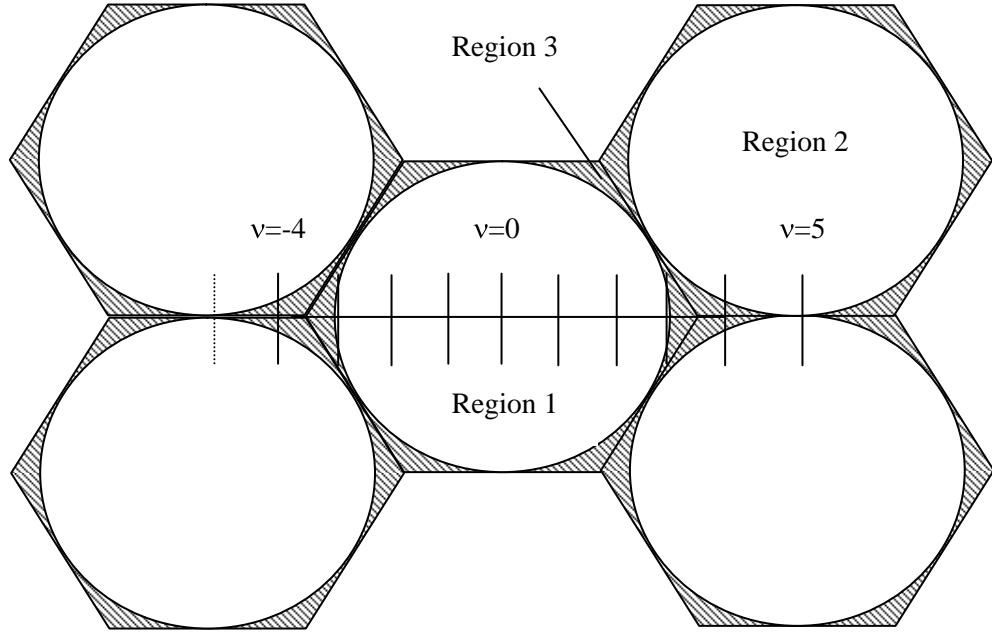


Figure 1.15: Brillouin zone for a zigzag (5,0) semiconducting CNT superimposed on graphene k-space. Both LA and LO phonon dispersions are approximately isotropic around each Γ -point, and the phonon energies are constant in the shaded regions of the graph.

$$e_p^{LO}(\mathbf{q}, \mu) = \begin{cases} \hbar \omega_0^{LO} + B_1(q_1 a)^2 + B_2|q_1 a|^3 + B_3(q_1 a)^4 + B_4|q_1 a|^5 & \text{Region 1} \\ \hbar \omega_0^{LO} + B_1(q_2 a)^2 + B_2|q_2 a|^3 + B_3(q_2 a)^4 + B_4|q_2 a|^5 & \text{Region 2} \\ \hbar \omega_m^{LO} & \text{Region 3} \end{cases} \quad (1.25)$$

Here the parameters are, $B_1 = -0.43$ meV, $B_2 = 2.91$ meV, $B_3 = -2.23$ meV, $B_4 = 0.36$ meV, and the LO phonon energy of graphene at the Γ -point and the \mathbf{M} -point are $\hbar\omega_0^{\text{LO}} = 196.3$ meV and $\hbar\omega_m^{\text{LO}} = 171.2$ meV, respectively.

Using the above equations, LA or LO phonon dispersion curves for any CNT can be obtained by zone folding. Similar to the electronic bands, phonon branches are symmetric around $q = 0$ and doubly degenerate for $\pm\mu$ with the exception of $\mu = 0, n$. As an example, the LA and LO phonon dispersion relations for CNT (10,0) are shown in Figure 1.16 a and b, respectively. In analogy to the electronic subbands, the number of phonon branches increases with increasing tube diameter. For an $(n, 0)$ CNT there are a total of $2n$ LA and LO phonon branches.

The radial breathing mode phonon dispersions are evaluated for zigzag CNTs based on separate lattice dynamical calculations taking into account interactions up to the fourth nearest neighbor carbon atoms. The CNT force constant tensors are obtained by unitary transformation of the force constant tensors of graphene, which are determined by fits to experimental data [3]. The RBM phonon branches are found to be nearly dispersionless, although they interact with the LA mode. The lowest RBM phonon energy is found to be $E_p^{\text{RBM}} \approx C_1/d$, where d is the tube diameter, and the fitting parameter $C_1 = 27.9$ meV-nm. This is in agreement with references 36 and 37. The RBM energies for CNT (10,0) and CNT (11,0) are 35.2 meV and 32 meV, respectively. For this work only the lowest RBM phonon with $\mu = 0$ is considered, where μ is the phonon branch index. This phonon branch corresponds to a breathing mode with all atomic displacements in phase and, as will be shown in the next section, it induces intrasubband electron transitions. Higher index RBM phonon branches, corresponding to

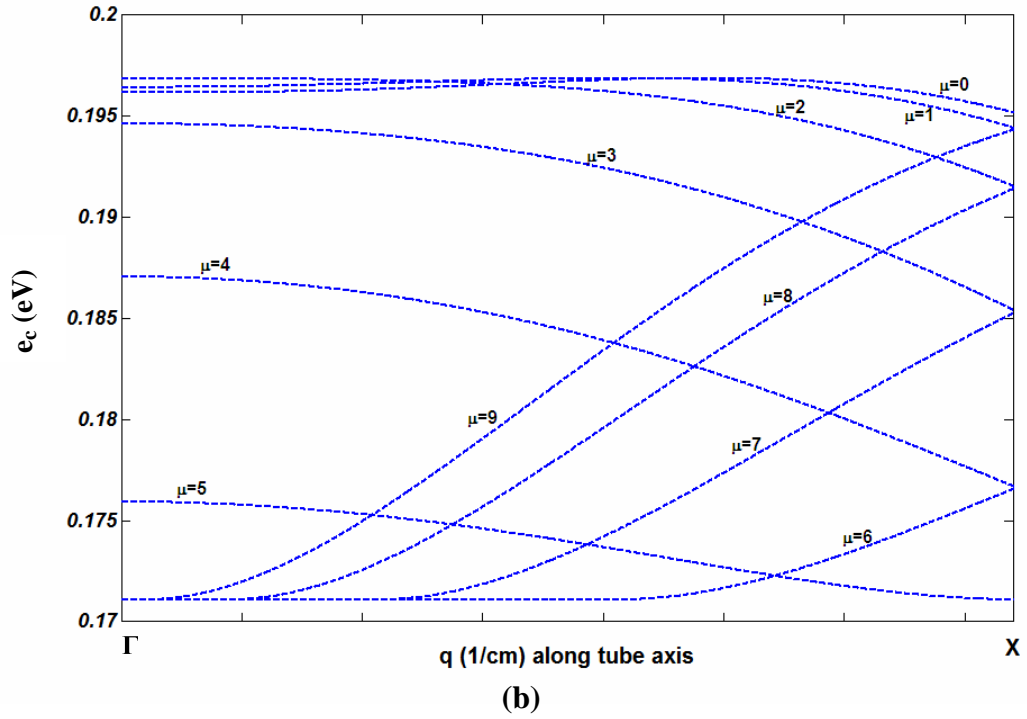
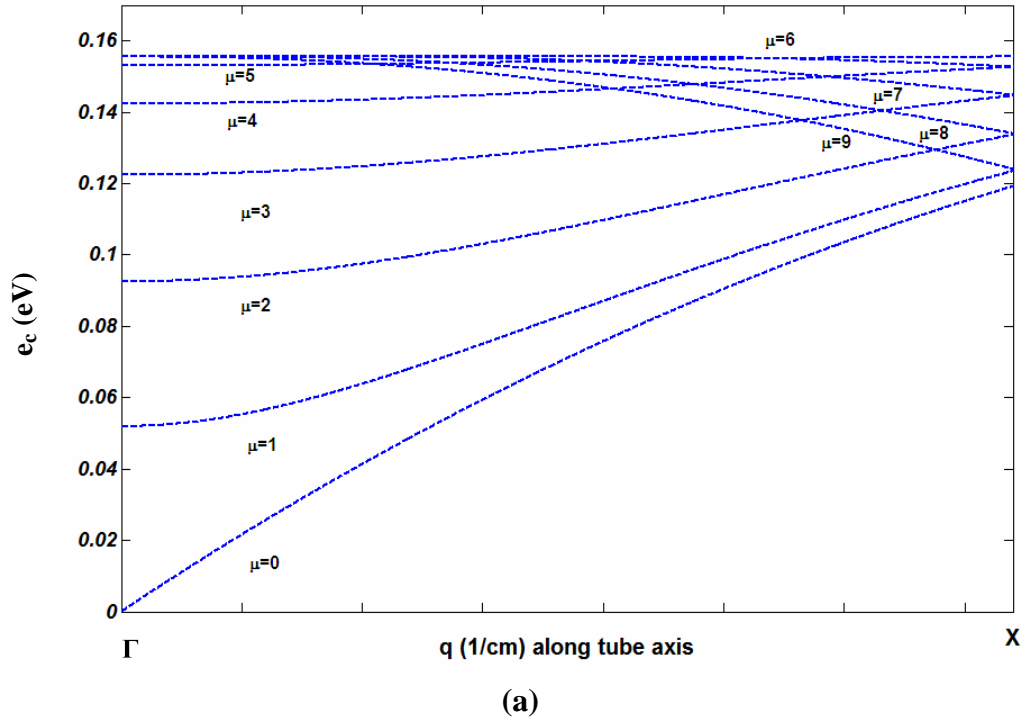


Figure 1.16: (a) LO and (b) LA phonon dispersion for (10,0) CNT by zone folding the LA and LO phonon modes of graphene.

intersubband electron transfer, are not required, because results presented in Chapter 3 demonstrate that almost all of the electrons remain within the lowest subband even at relatively high electric fields because of the strong LA and LO phonon scattering. Moreover the lowest possible intersubband transitions corresponding to an Umklapp process that scatters electrons from subbands $\nu = \pm 7$ to subbands $\nu = \mp 7$ involves phonons with branch indices $\mu = \mp 6$ for CNT (10,0) and $\mu = \mp 8$ for CNT (11,0) [section 1.8]. These RBM phonon branches have much higher energy, and therefore are not excited to a significant degree at room temperature.

1.8 Electron-phonon interaction

The electron-phonon scattering rate is calculated using first order perturbation theory and the deformation potential approximation. Taking the value of overlap integral between the cell periodic parts of the initial and final Bloch states to be unity, an electron initially in band ν_i with a wave vector \mathbf{k}_i , scatters inelastically with LA phonons with a rate given by [22,23] (appendix):

$$W(\mathbf{k}_i, \nu_i) = \sum_{\substack{\text{all} \\ \text{possible} \\ \mathbf{q}, \mu}} \frac{\hbar D_{LA}^2 \left[q^2 + \left(\frac{2\mu}{d} \right)^2 \right]}{2\rho e_p^{LA}(\mathbf{q}, \mu)} \times \left(N \left[e_p^{LA}(\mathbf{q}, \mu) \right] + \frac{1}{2} \pm \frac{1}{2} \right) \times d\delta \quad (1.26)$$

where, $\mathbf{k}_f = \mathbf{k}_i \pm \mathbf{q}$, D_{LA} is the deformation potential constant for the LA phonon (the same

value is used as in previously reported Monte Carlo calculations [22,23]), $N(e)$ is the Bose-Einstein phonon occupation number in equilibrium, ρ is the linear mass density of the nanotube, and the (+) and (-) sign indicate phonon emission and absorption respectively. Also $q = |\mathbf{q}|$. The function $d\delta$ is a 1-D joint density of states given by:

$$d\delta = \left| \frac{de(\mathbf{k}_f, \nu_f)}{d\mathbf{q}} \pm \frac{de_p(\mathbf{q}, \mu)}{d\mathbf{q}} \right|^{-1} \quad (1.27)$$

and can be evaluated directly from the tabulated values of the electron band structure and phonon dispersion (appendix). The phonon wave vectors \mathbf{q} , and the phonon branch index μ involved in the electron scattering process are determined from the requirements of energy and momentum balance during the electron-phonon interaction. Based on the final state of the electron after scattering, two different processes are possible. They are the Normal process and the Umklapp process [38]. A Normal process results in a final electron wave vector \mathbf{k}_f that lies within the first BZ, while an Umklapp process results in a \mathbf{k}_f that lies outside the first BZ, and a reciprocal lattice vector needs to be added to it to determine an equivalent point within the first BZ. For a Normal process, the requirements of energy and momentum balance lead to the following selection rules for \mathbf{q} and μ :

$$\left. \begin{aligned} e(\mathbf{k}_f, \nu_f) &= e(\mathbf{k}_i, \nu_i) \pm e_p(\mathbf{q}, \mu), \\ \mathbf{k}_f &= \mathbf{k}_i \pm \mathbf{q}, \\ \nu_f &= \nu_i \pm \mu, \end{aligned} \right\} \quad (1.28)$$

Here (+) and (-) signs indicate phonon absorption and emission, respectively, and ν_f denotes the final subband of the electron.

For an Umklapp process the selection rules become:

$$\left. \begin{aligned}
 k_f &= k_i \pm q - \frac{2\pi}{\sqrt{3}a} \hat{k} \text{ and } \nu_f = \nu_i \pm \mu - n; \text{ if } 0 < \nu_f \leq n, \text{ but } k_i \pm q > \frac{\pi}{\sqrt{3}a} \hat{k} \\
 k_f &= k_i \pm q - \frac{2\pi}{\sqrt{3}a} \hat{k} \text{ and } \nu_f = \nu_i \pm \mu + n; \text{ if } -n+1 \leq \nu_f \leq 0, \text{ but } k_i \pm q > \frac{\pi}{\sqrt{3}a} \hat{k} \\
 k_f &= k_i \pm q + \frac{2\pi}{\sqrt{3}a} \hat{k} \text{ and } \nu_f = \nu_i \pm \mu - n; \text{ if } 0 < \nu_f \leq n, \text{ but } k_i \pm q < -\frac{\pi}{\sqrt{3}a} \hat{k} \\
 k_f &= k_i \pm q + \frac{2\pi}{\sqrt{3}a} \hat{k} \text{ and } \nu_f = \nu_i \pm \mu + n; \text{ if } -n+1 \leq \nu_f \leq 0, \text{ but } k_i \pm q < -\frac{\pi}{\sqrt{3}a} \hat{k} \\
 k_f &= k_i \pm q \text{ and } \nu_f = \nu_i \pm \mu - 2n; \text{ if } |k_f| < \frac{\pi}{\sqrt{3}a} \text{ but } \nu_i \pm \mu > n \\
 k_f &= k_i \pm q \text{ and } \nu_f = \nu_i \pm \mu + 2n; \text{ if } |k_f| < \frac{\pi}{\sqrt{3}a} \text{ but } \nu_i \pm \mu < -n+1
 \end{aligned} \right\} \quad (1.29)$$

Similarly, the scattering rate for electrons interacting with LO phonons is given by:

$$W(k_i, \nu_i) = \sum_{\substack{\text{all} \\ \text{possible} \\ \mathbf{q}, \mu}} \frac{\hbar D_{LO}^2}{2\rho e_p^{LO}(\mathbf{q}, \mu)} \times \left(N[e_p^{LO}(\mathbf{q}, \mu)] + \frac{1}{2} \pm \frac{1}{2} \right) \times d\delta \quad (1.30)$$

where D_{LO} is the deformation potential field for the LO phonon. D_{LO} is chosen to agree with recent experimental data [39,40]. The scattering rates for electrons interacting with RBM phonons is given by:

$$W(\mathbf{k}_i, \nu_i) = \sum_{\substack{\text{all} \\ \text{possible} \\ \mathbf{q}, \mu}} \frac{\hbar D_{RBM}^2}{2 \rho e_p^{RBM}(\mathbf{q}, \mu)} \times \left(N[e_p^{RBM}(\mathbf{q}, \mu)] + \frac{1}{2} \pm \frac{1}{2} \right) \times d\delta \quad (1.31)$$

where D_{RBM} is the deformation potential field for the ($\mu=0$) RBM, defined as $D_{RBM} = (1/2) \left(\partial(E_b^c - E_b^v) / \partial u \right)$ eV/Å, E_b^c and E_b^v are the conduction and valence band energies at the band extrema ($k=0$) for the lowest subbands. The RBM-electron-interaction deformation potentials for CNTs (10,0) and (11,0) are obtained as 1.28 eV/Å and 0.93 eV/Å, respectively, from recently reported results based on *ab initio* calculations [36].

After having obtained the electron band structure, the phonon dispersion, and the electron-phonon scattering rates expressions, we are ready to set up a numerical simulator to study the charge transport properties of CNTs. As was mentioned, the numerical simulator is based on the Monte Carlo algorithm. A description of the issues related to the simulator will form part of the next chapter.

CHAPTER 2

Ensemble Monte Carlo simulation for semiconducting carbon nanotubes

2.1 Boltzmann transport equation

As computer processing speeds and memory have increased, various methods have been developed and refined to investigate computationally the charge transport properties in semiconductor materials and devices. The most popular and widely used methods involve the solution of the Boltzmann Transport Equation (BTE). These are usually referred to as the classical or semi-classical formulations. Some of these methods are:

1. Drift-Diffusion
2. Hydrodynamic
3. Monte Carlo

All these methods in essence rely on calculating the electron distribution within a semiconductor device or material in different ways. The electron distribution is the solution of the BTE, which is given by [30,41]:

$$\frac{\partial f}{\partial t} + \frac{d\mathbf{r}}{dt} \cdot \nabla_{\mathbf{r}} f + \frac{d\mathbf{p}}{dt} \cdot \nabla_{\mathbf{p}} f = \sum_{\mathbf{p}'} [f(\mathbf{p}') [1 - f(\mathbf{p})] S(\mathbf{p}', \mathbf{p}) - f(\mathbf{p}) [1 - f(\mathbf{p}')] S(\mathbf{p}, \mathbf{p}')] \quad (2.1)$$

where f is the distribution function ($f \equiv f(\mathbf{r}, \mathbf{p}, t)$), \mathbf{r} is the position vector and \mathbf{p} is the momentum vector. The first term on the right, $f(\mathbf{p}') [1 - f(\mathbf{p})] S(\mathbf{p}', \mathbf{p})$, in the above equation denotes in-scattering from \mathbf{p}' to \mathbf{p} due to collisions (from phonons, other electrons etc.) and increases $f(\mathbf{p})$. For this to occur, the state denoted by \mathbf{p}' should be occupied, and the state denoted by \mathbf{p} should be empty. S is the transition rate, i.e., the probability per second that an electron from state \mathbf{p}' will scatter to state \mathbf{p} . Similarly, the second term on the right, $f(\mathbf{p}) [1 - f(\mathbf{p}')] S(\mathbf{p}, \mathbf{p}')$, denotes out-scattering from state \mathbf{p} to \mathbf{p}' . This will decrease $f(\mathbf{p})$. Under non-degenerate conditions, $f(\mathbf{p}) \ll 1$, and $1 - f(\mathbf{p}) \approx 1$. The summation in the equation is over \mathbf{p}' . In effect, the solution of the BTE provides a method to obtain the distribution function under various externally controlled parameters (electric field, etc.) and internal effects (scattering, etc.). The equation states that the total time rate of change of the distribution function is dependent upon the rate at which particles scatter, either with each other, or with the lattice.

2.2 Monte Carlo method

As was mentioned in the previous section, Monte Carlo is one of the methods to solve the BTE numerically. This method involves tracking the trajectories of a large number of particles, or in simple cases, a single particle over a long period of time. The

Monte Carlo method provides the most accurate solution of the BTE at intermediate and high electric fields. However it is computationally intensive because of the need to work with a large ensemble of carriers over long trajectories (or in a few limited cases of interest, a single carrier over long trajectories). This fact also introduces statistical noise at low electric fields where the Monte Carlo method consequently becomes less accurate.

In terms of electron transport, during a Monte Carlo simulation, the carriers drift under a uniform electric field classically, i.e., they follow Newton's laws of motion. After a free drift, carriers scatter from phonons, impurities, or other carriers. The scattering mechanism is selected randomly. However the selection is not uniformly random. It reflects the scattering rate of the mechanism as a fraction of the total scattering rate. Scattering is assumed to change the carrier momentum instantaneously, but not the carrier position. This is because the time involved in a collision is much shorter than the free drift time [42]. Figure 2.1 shows the outline of the Monte Carlo method as applied specifically to bulk simulation of semiconductor materials.

Initial conditions for the simulations are based on a host of factors. In a lot of cases involving bulk simulation, particles are assumed initially to be distributed with a Gaussian distribution in reciprocal space with a mean momentum of zero ($\langle \mathbf{k} \rangle = 0$), and a mean carrier temperature equal to the lattice temperature. In some cases, particles are initially assumed to be injected into the semiconductor material with energy greater than the equilibrium thermal energy. This could happen, for example, when modeling a thermionic electron emission over a barrier. Particles are all usually assumed to be at a position arbitrarily defined as $z = 0$. However, in a device simulation particles are usually initially "spread over" the device in a way that reflects the best initial possible "guess"

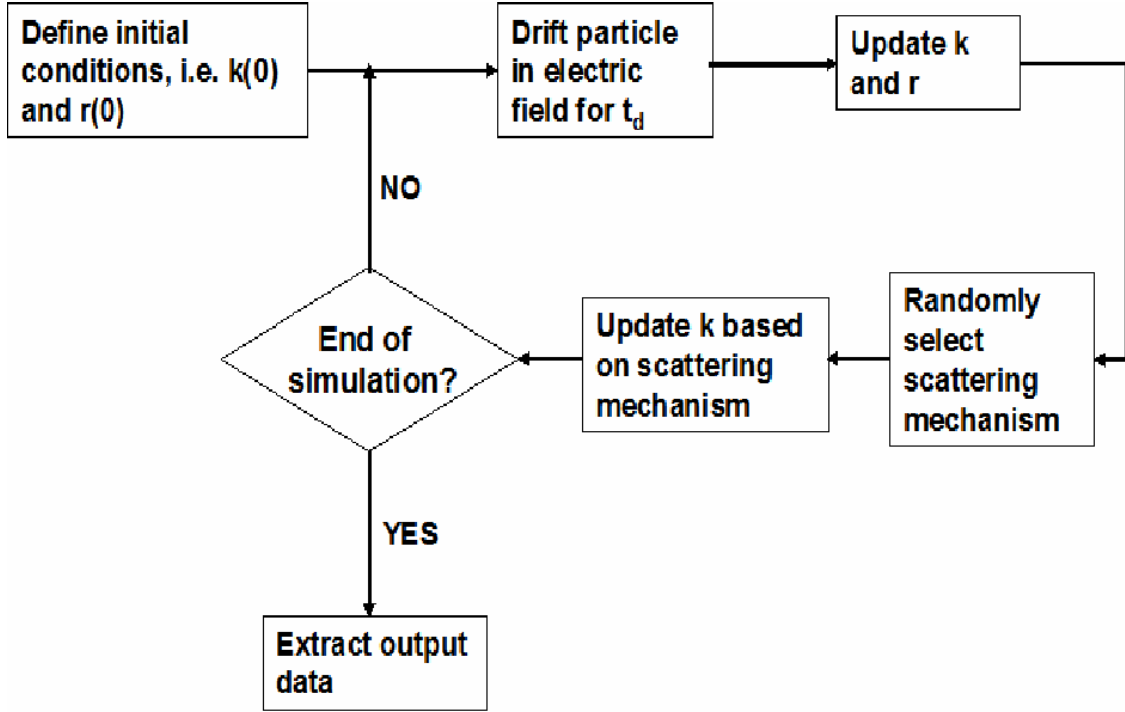


Figure 2.1: Monte Carlo method applied to the charge transport simulation of bulk semiconductor materials. Electrons drift according to classical mechanics, but scatter quantum mechanically. This makes Monte Carlo a semi-classical transport simulator.

about the concentration and equilibrium Poisson equation solution.

The free-drift time may be assumed to be a constant low value for all the particles involved in the simulation such that $\tau_d \ll \tau_t$, where τ_d is the free drift time and

$\tau_t = \frac{1}{\max(\text{total scattering rate for all } \mathbf{k})}$. The total scattering rate is the sum of all the

individual scattering rates at any particular \mathbf{k} ($=|\mathbf{k}|$) point and $\max(\text{total scattering rate for all } \mathbf{k})$ is the maximum value of the individual total scattering rates. An alternate method is

to use a randomly generated drift-time after each drift-scattering cycle. This involves the introduction of a “self-scattering” mechanism [41]. In this method each particle has a different free-drift time.

If we do not consider carrier-carrier interactions, the crystal momentum and position of each particle is updated after each drift. This involves quite simply the use of Newton’s laws under an external force, QE , where E is the applied electric field and Q is the magnitude of the electron charge.

After updating the crystal momentum and position information, the scattering mechanism is selected randomly, as has been explained above. The final electron crystal momentum after scattering is dependent upon the type of scattering mechanism selected. In addition, a carrier scattering event conserves total energy and crystal momentum. Particles then drift under the applied electric field with the new initial crystal momentum. This process is continued until the desired simulation time. This time duration may be long (\sim fraction of a ns to a ns or longer), if we are interested in evaluating the steady-state results. However, for transient results, the time duration is usually less than a picosecond.

A critical issue in Monte Carlo simulation is the treatment of the band structure. One may approximate the band structure by a simple analytical approximation such that [41]:

$$e(1 + \alpha e) = \frac{\hbar^2 k^2}{2m^*} \quad (2.2)$$

where α is the correction to the parabolic fit to the real band structure, and is called the non-parabolicity factor, m^* is the electron effective mass near the bottom of the band, e is the electron energy corresponding to the k-point, and \hbar is the reduced Plank's constant. The Monte Carlo simulator that utilizes this scheme of band structure representation is known as an analytical band Monte Carlo simulator. The analytical approximation is relatively simple to implement. However, since in most semiconductor materials the band structure is far more complicated than represented by Equation 2.2, the analytical assumption is accurate only near the bottom of the bands and consequently useful only up to intermediate electric fields.

For higher electric fields, the exact band structure needs to be taken into account within the simulator. This is done within the Monte Carlo simulator by discretizing the band structure into grids of k-points. The energy associated with each k-point is then stored as an array within the simulator. Simulation accuracy is limited by the number of grid points and thus the grid point spacing. It is clear that this simulator, also called the numerical band Monte Carlo simulator, is very computer memory intensive. However, this method has been used extensively to study high field transport in various semiconductor materials and devices and provides some of the most accurate (and vivid) depictions of the physics of charge transport in semiconductor materials and devices.

Use of a single particle (electron or hole) for simulation, called the single-particle Monte Carlo method, is useful only for steady-state, and only for specific cases, for example evaluating the field-dependent mobility. For all other cases, one needs to simulate a large number of electrons – ranging from a few thousand to a few hundred thousand. This is called the Ensemble Monte Carlo, or EMC, method.

2.3 Ensemble Monte Carlo simulation for carbon nanotubes

Work as part of this thesis includes the Ensemble Monte Carlo (EMC) numerical simulation of bulk charge transport properties in semiconductor carbon nanotubes (CNTs). A basic description of MC methods for numerical modeling of semiconductors has been provided in the previous section. From that discussion, we may conclude that the initial requirements for a carbon nanotube EMC simulator include:

1. Determination of the electronic band structure: This has been covered in section 1.6.
2. Determination of the phonon dispersion: This has been covered in section 1.7.
3. Determination of the electron-phonon scattering rates: The prescriptions are provided in section 1.8.
4. Basic EMC transport simulation setup: Details follow.

Within a CNT, electrons move parallel to the axis of the tube and the \mathbf{k} vector is continuous only along the axis. Along the circumference of the tube, the \mathbf{k} vector is discretized resulting in subbands (section 1.5). However, in a 3-D bulk material, the \mathbf{k} vector is treated as continuous along all the three spatial directions, resulting in a 3-D band structure. On the other hand, in a 2-D material, the \mathbf{k} vector is continuous along two directions and is discretized along the third [41]. Therefore the pseudo 1-D nature of a CNT results in a limited phase space, compared to a bulk material.

The restriction on the phase space for electrons in a CNT also impacts the scattering

events. In a 3-D material, after an electron-phonon interaction, the electron final wave vector, \mathbf{k}_f , has three directions available to relax, resulting in a maximum of nine possible combinations of $(\pm k_{x_f}, \pm k_{y_f}, \pm k_{z_f})$. However in a 1-D material, electrons undergo only either a forward scattering (\mathbf{k}_f is in the direction of the initial electron wave vector, \mathbf{k}_i), or back scattering (\mathbf{k}_f is directed opposite to \mathbf{k}_i). This reduction in the available final states results in a reduction of the scattering rates.

The one dimensionality of the CNT charge transport problem provides certain advantages. Instead of keeping track of electron transport over all the three spatial dimensions, as in a 3-D MC calculation, only a single dimension needs to be incorporated for a CNT. This also makes it easier to determine the phonon wave vector \mathbf{q} , and the final electron wave vector \mathbf{k}_f . The algorithm used to determine these two vectors for an initial wave vector \mathbf{k}_i is illustrated in Figure 2.2, which shows an absorption process (the figure is for illustration purpose only and does not correspond to a real CNT subband or phonon dispersion).

The electron is initially at point k_i ($= |\mathbf{k}_i|$) (Figure 2.2a) and the phonon branch (Figure 2.2b) is as given. For an absorption process, the $q = 0$, $E_p = 0$ point on the phonon dispersion (i.e., the origin), is placed on k_i . The phonon branch is extended along both positive and negative q directions (Figure 2.2c). As can be seen in the figure, the phonon branch intersects the electron band structure at two k -points, one for a positive q -value and the other for a negative q -value. These k -points represent a conservation of both energy and crystal momentum and are the two possible final k -points, k_{f1} and k_{f2} , in the electron-phonon scattering process.

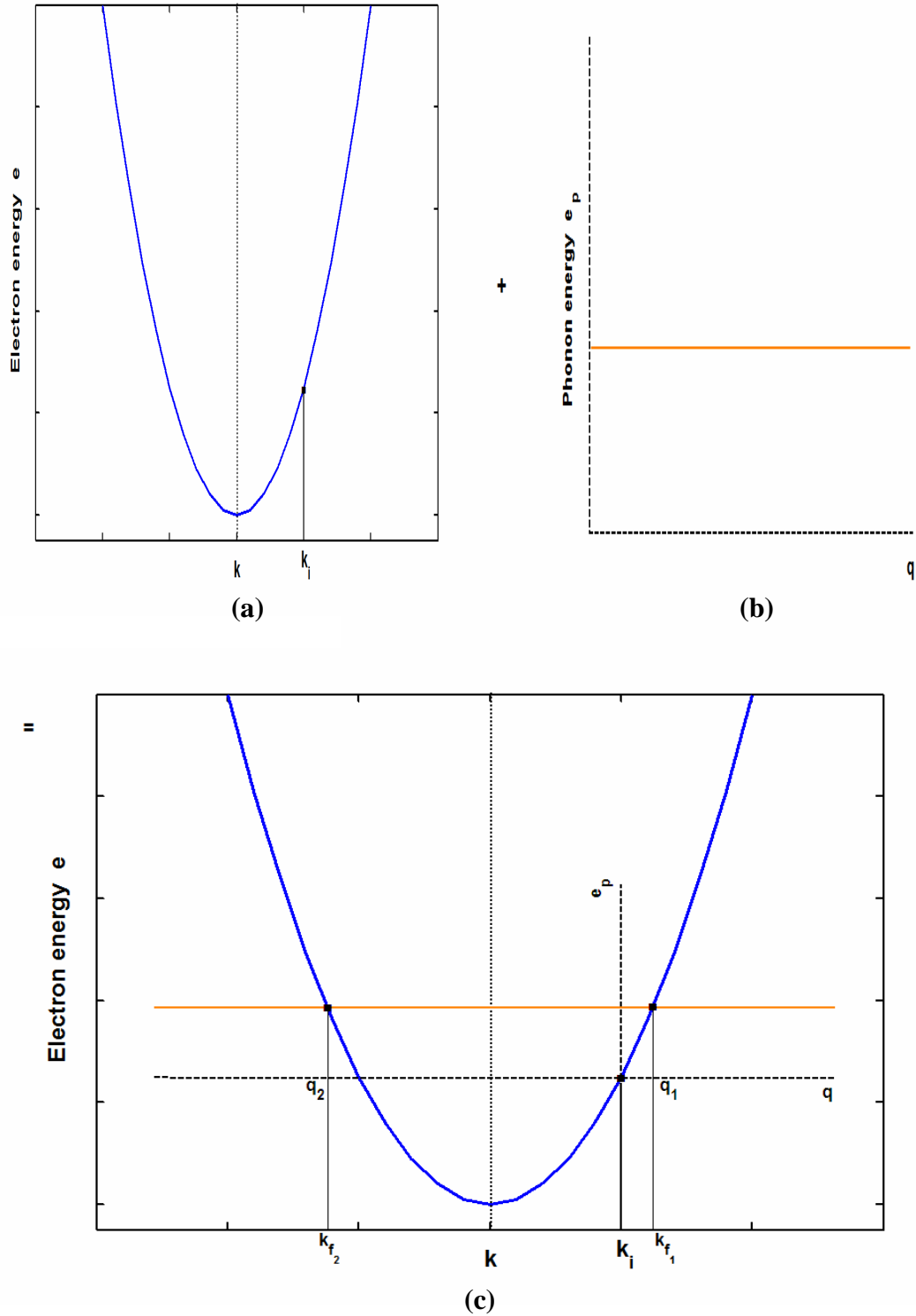


Figure 2.2: Illustration of the algorithm used to determine the final electron state after scattering. (a) The initial electron position, k_i . (b) The phonon branch involved in the electron scattering. (c) An absorption process with the final two possible electron k vectors and the phonon q vectors (see text for explanation).

The above process has, however, a limitation. Beyond a certain k_i -point, the determination of k_f would require that the phonon dispersion be extended beyond the first BZ. In order to avoid this, and yet evaluate the scattering rates for these k -points, complementary subbands need to be considered. For a semiconducting zigzag (n,0) CNT, subbands ν_1 and ν_2 are defined as complementary if $|\nu_1| + |\nu_2| = n$. Subband ν_1 has the same energy dispersion in the second BZ as ν_2 has in the first BZ and vice versa. The use of complementary subbands greatly eases the search for a final state. If during the scattering rate evaluation process, the phonon q vector is found to lie outside the first BZ, a k -point in the complementary subband is evaluated in the second BZ by the same method of intersection of two lines outlined above and demonstrated in Figure 2.2. This k -point in the complementary subband is equivalent to a final k_f in the desired subband through an Umklapp process. Therefore, for the scattering rate evaluation, Umklapp processes, in addition to Normal processes, need to be considered. This is taken into account in the selection process for phonons involved in electron scattering in Equations 1.29 and 1.30.

The simplest EMC simulation setup for CNTs includes the approximation of the electron band structure by Equation 2.2, and the phonon dispersion by linear relationships [22,23]. This allows one to find the final electron state after scattering, k_f , and the phonon wave-vector, q , involved in the process in a straightforward manner, as solutions to Equation 2.2 and linear phonon dispersion approximations, and therefore circumvents the need to implement the algorithm depicted in Figure 2.2. However this method is accurate only up to a certain relatively low value of electron energy. Beyond this range the analytical approximation to the band structure breaks down, and a linear description of

the phonon dispersion no longer remains valid [27]. Therefore for a greater accuracy in the study of charge transport in CNTs, particularly at intermediate and high electric fields, a realistic band structure and phonon dispersion need to be considered. This has been undertaken as part of this work.

For the determination of the electron-phonon scattering rates, which involves the solution of Equations 1.27, 1.31, and 1.32, the electron band structure is divided into 18,000 grid points covering the first and second BZs. The phonon dispersion is divided into 10,000 grid points covering the first BZ. The grid spacing is made extremely small to ensure greater accuracy (but at the cost of computer memory). An additional condition on the grid spacing will be discussed shortly. For each possible electron-phonon interaction, for an initial electron wave vector, \mathbf{k}_i , there are at most two possible \mathbf{q} vectors and consequently two possible \mathbf{k}_f , as seen in Figure 2.2. To determine these values, a loop is set up that runs over the entire 10,000 grid points for the phonon dispersion. At each step, the q -value is added to k_i , resulting in a new k -value. The energy corresponding to this k -value is obtained from the stored electron band structure and compared to the sum of the phonon energy and initial electron energy. The q -value and the k -value for which the energy difference is minimum are selected as the \mathbf{q} vector and \mathbf{k}_f vector. This is demonstrated in Figure 2.3.

In the formulation for the scattering rates, equations 1.27, 1.31, and 1.32, the term $d\delta$ (Equation 1.28), called the 1-D joint density of states (DOS), is seen to vary as

$$1/\sqrt{e(\mathbf{k}_f) - e_c} \text{ (appendix), where } e_c \text{ is the energy of the bottom of the subband where } \mathbf{k}_f$$

lies. This means that the scattering rate will approach infinity for any electron transition to very near the bottom of a subband. One way to avoid this situation is to use collisional

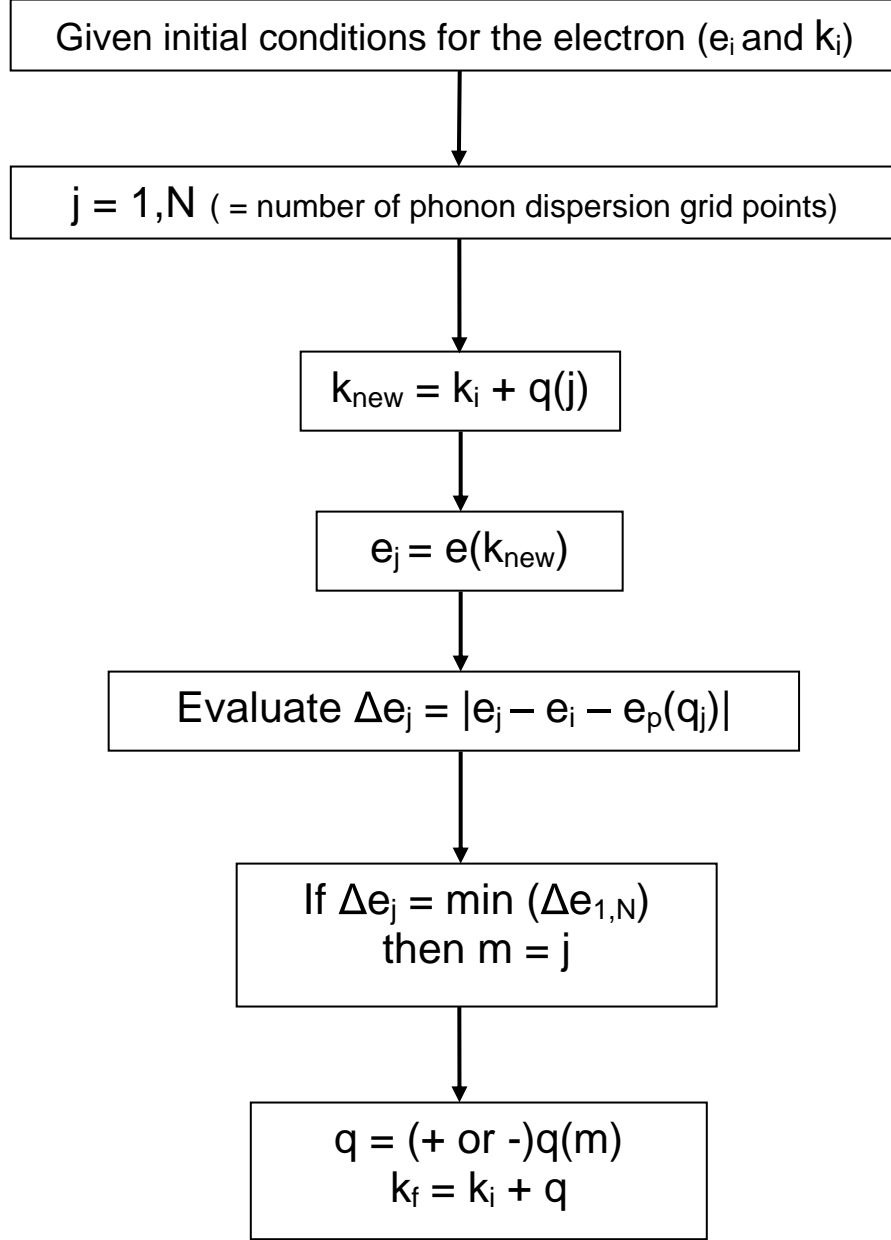


Figure 2.3: Algorithm implemented to evaluate q and k_f based on Figure 2.2. Momentum is balanced, but there is a slight error involved in balancing energy. This also makes EMC less accurate at low electric fields. The $j=1,N$ loop is evaluated once for each direction of q (see Figure 2.2), resulting in a $+q(m)$ and $-q(m)$ value.

broadening [23]. However this method introduces an additional burden on the computer processor and memory and increases the complexity of the numerical model. Another way to get around the divergence of the scattering rate is to divide the band structure into grid points in a way such that an electron transition does not cause $d\delta$ to be so large as to lead to computational difficulties. This is the additional condition imposed on the division of the band structure into grid points. Both methods were implemented into the EMC scheme, and the results were found to be the same. Therefore the careful division of the band structure into grid points not only overcomes the mathematical infinity involved in the electron-phonon interactions, but also avoids the introduction of additional complexity and demand on the computing resources that would be needed by the introduction of collisional broadening. Chapter 3 depicts the scattering rates for various CNTs.

Once the individual scattering rates are computed, the total scattering rate for each k-point is evaluated and stored in a separate array. At the same time, this array also stores the contribution of the individual scattering rates to the total scattering rate. That means that if there are, for example, three different scattering mechanisms, A, B, and C, and the respective scattering rates at a k-point, k_p , are a, b, and c per second, then the array would appear to be of the form:

$$\left. \begin{aligned} \text{Swk}(1, k_p) &= a \\ \text{Swk}(2, k_p) &= a + b \\ \text{Swk}(3, k_p) &= a + b + c \end{aligned} \right\} \quad (2.3)$$

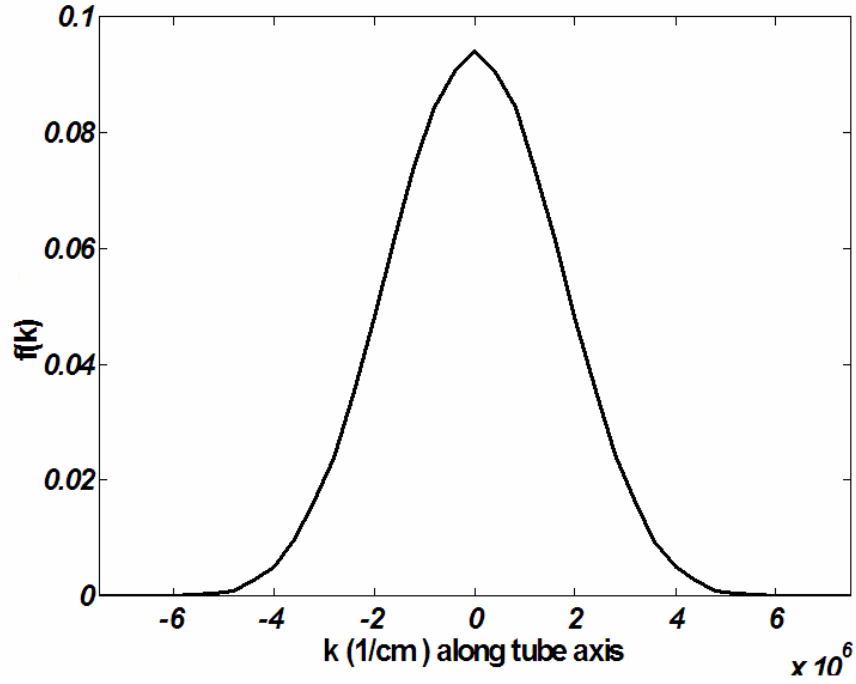
Therefore, $Swk(3, k_p)$ is the total scattering rate at the point k_p . Once Equation 2.3 is evaluated for all k-points in the electron band structure grid, we are ready to start the Monte Carlo transport simulation for a CNT. We will return to the example illustrated by Equation 2.3 to explain the selection of a scattering process during the Monte Carlo simulation.

Initially, all electrons are distributed according to the equilibrium thermal Gaussian distribution in the first subband, and the simulation is started from the $z=0$ position. Figure 2.4 shows the initial electron distribution in k-space (a) and versus energy (b).

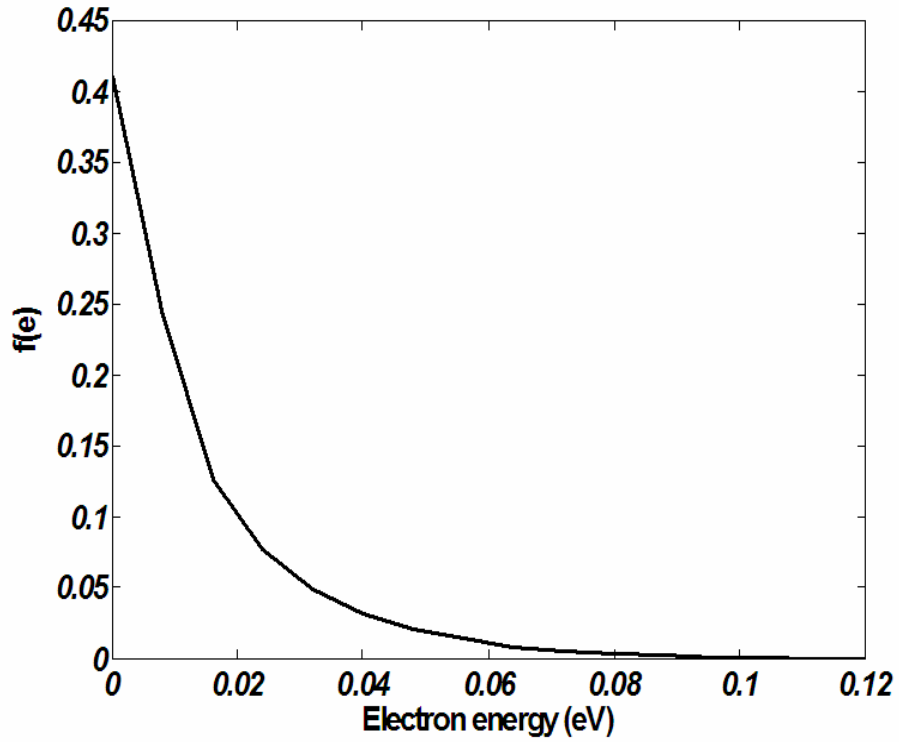
The Gaussian distribution is obtained through the application of the Central Limit Theorem [43]. The starting point is to obtain a random variable R such that:

$$R = \sum_{i=1,..,j} (r_i - 0.5) \quad (2.4)$$

where r_i is a random variable uniformly distributed between 0 and 1. j is chosen such that the final electron distribution has an average energy of $\frac{1}{2}K_B T$, where T is the temperature and K_B is the Boltzmann constant. In this work, $j=6$ has been found to be a reasonable assumption. After the determination of R , the following prescription is applied to determine the k-value for an electron:



(a)



(b)

Figure 2.4: (a) Equilibrium momentum, and (b) energy distributions for CNT (10,0) at 300K. The momentum distribution is Gaussian with a mean momentum of zero, while the average energy is equal to the thermal energy.

$$k = R \times \sqrt{\frac{2m^* K_B T}{\hbar^2}} \quad (2.5)$$

The process is repeated for all the electrons and the value of k for each is stored in a separate array.

In the presence of an electric field, an electron accelerates (drifts) for a time t_d . This time is of the order of a fs (10^{-15} seconds). During this time, the electron gains momentum from the electric field and has a new \mathbf{k}_p . After the drift, the electron scatters through a phonon interaction, whereby it either gains or loses energy and momentum. For the selection of the scattering process involved, a random number between 0 and 1 is generated. The random number is compared to the ratio of the drift time and the inverse of the total scattering rate for the electron at the grid point \mathbf{k}_p ($=|\mathbf{k}_p|$) (Equation 2.3). If the random number is smaller than the ratio, the electron will scatter, and only the scattering process need be now determined. If the ratio is larger, then the electron is allowed to complete its drift without scattering. To determine the scattering process involved, another uniform random number ran is generated, which is then multiplied by the total scattering rate at \mathbf{k}_p . If we look at the example in Equation 2.3 above, which shows the total scattering rates array, then the above discussion implies that we obtain a number of the form:

$$SWK = ran \times Swk(3, \mathbf{k}_p) \quad (2.6)$$

SWK is then compared to $Swk(1, \mathbf{k}_p)$. If SWK is found to be less than $Swk(1, \mathbf{k}_p)$, scattering mechanism A is selected. If however SWK is found to be between $Swk(1, \mathbf{k}_p)$

and $S_{wk}(2, k_p)$, scattering mechanism B is selected, and so on. Once this is done, the momentum of the electron is updated based on the scattering process and the phonon wave vector involved. This completes one drift-scattering cycle for one electron. Figure 2.5 shows this basic outline of the algorithm mentioned. This cycle is then repeated for all the electrons. This completes the simulation for a time period of 1 fs (or another selected constant free drift time before scattering). The cycles are continued until the desired simulation time is reached, after which the final desired results are extracted through an appropriate averaging procedure [41]. For example, if the average k of the ensemble is desired, then all the k for all electrons are simply vector added and the result is divided by the number of electrons to obtain the average k per electron.

If, during a drift, an electron k vector is in the second BZ, it is translated to the first BZ by the addition of an appropriate reciprocal vector. However, in this work this has not been required because, as results to be presented in Chapter 3 show, most electrons remain at low magnitudes of k even at relatively high applied electric fields. The Umklapp processes associated with the phonon scattering, however, are needed and are included within the simulation. This has already been discussed above.

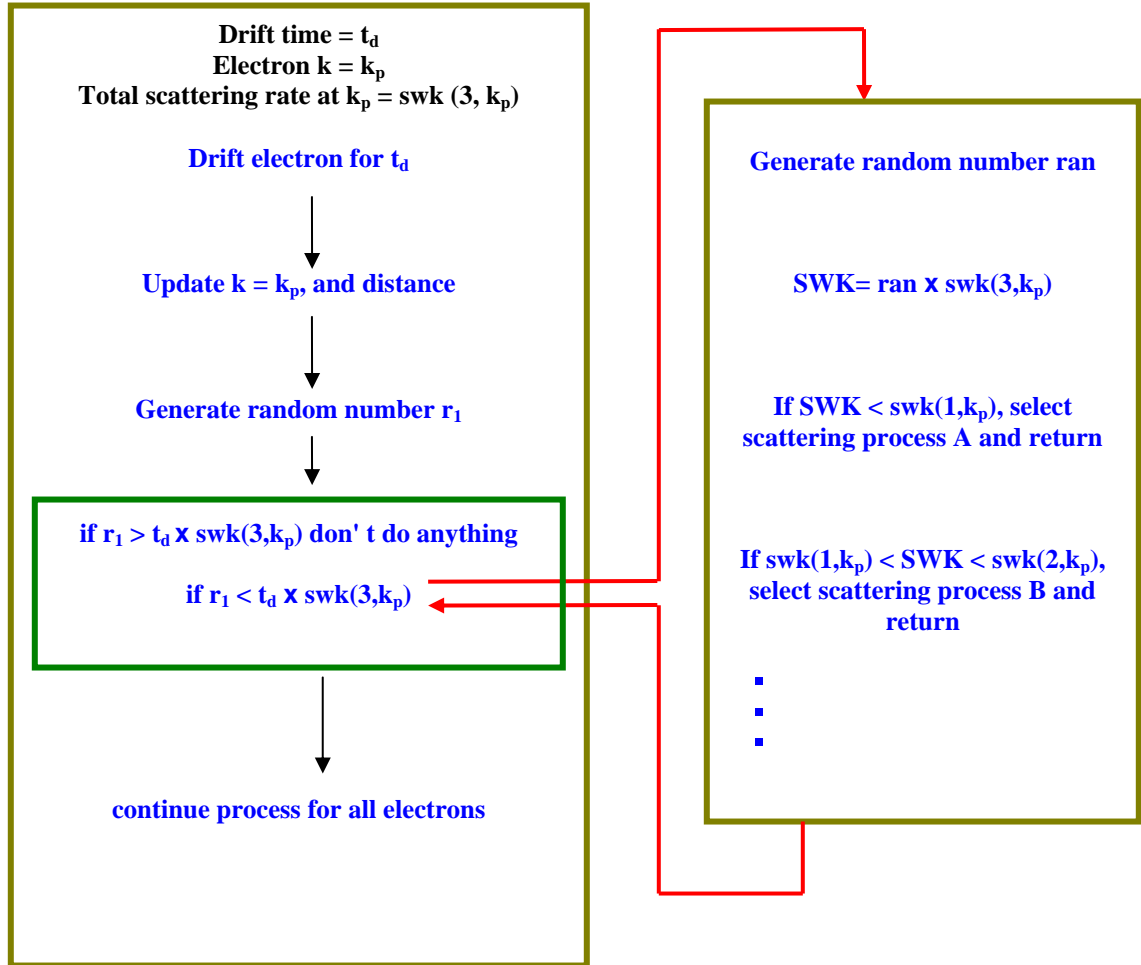


Figure 2.5: Algorithm for a drift-scattering cycle within the Monte Carlo CNT bulk simulator. The cycle is repeated until the desired total simulation time is reached.

Chapter 3

Results and discussion

Theoretical and numerical modeling of the charge transport properties of semiconducting zigzag carbon nanotubes (CNTs), undertaken as part of this work, has to a great extent relied upon the setting up of the ensemble Monte Carlo (EMC) algorithm. The details of the implementation of the EMC for CNTs have been discussed extensively in Chapter 2. Before proceeding further, it will be worthwhile to keep in mind some of the assumptions made about the CNTs being modeled. These are:

1. CNTs are single crystals without any crystal defects.
2. CNTs are intrinsic, i.e., there is no doping, either interstitial, or substitutional.
3. CNTs are infinite in extent.
4. The applied electric field is uniform and directed along the axis of the CNT (arbitrarily defined as the z -axis).
5. Electrons are initially at an arbitrary point in space defined as the origin, $z = 0$.
6. Electrons have an initial thermal distribution, with an average energy of $\frac{1}{2}K_B T$,

where T is the lattice temperature and K_B is the Boltzmann constant (Figure 2.4).

The stated aim of the work presented is not only the study of individual zigzag semiconducting CNTs, but also the study of the effect of physical structure on the

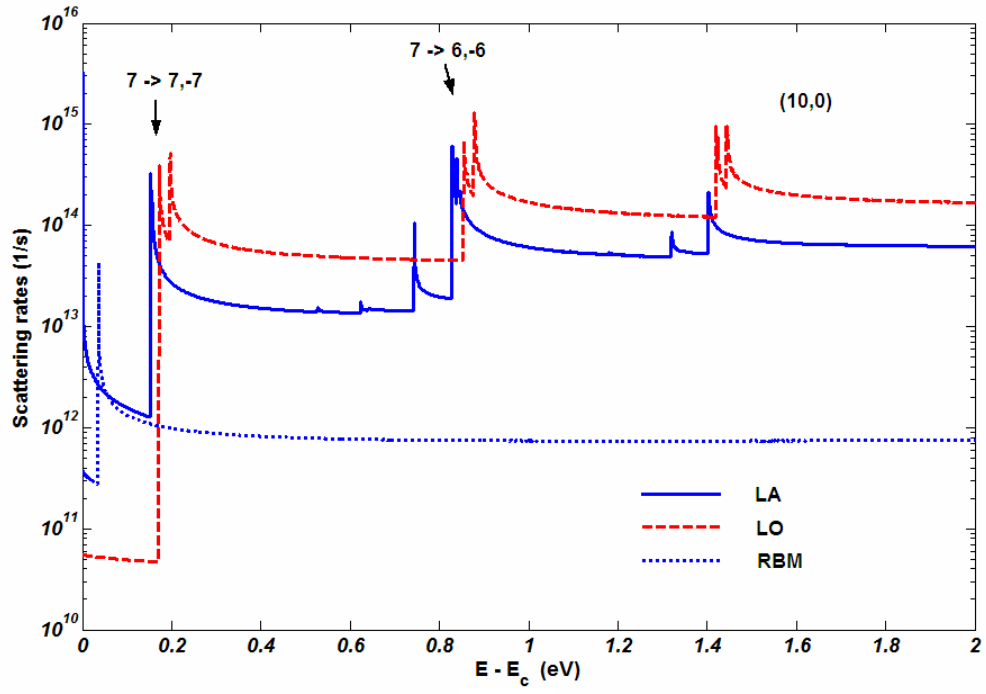
behavior of charge across these CNTs. This has necessitated the modeling of a large number of zigzag CNTs. Various CNTs are modeled with diameters ranging from relatively small, to intermediate, to relatively large. The CNTs selected also cover the two zigzag families, namely $(3p+1)$ and $(3p+2)$, where p is an integer. These CNTs are listed in Table 3.1.

Zigzag CNT family	Small diameter	Intermediate diameter	Large diameter
$(3p+1,0)$	(10,0)	(25,0)	(49,0)
$(3p+2,0)$	(11,0)	(26,0)	(50,0)

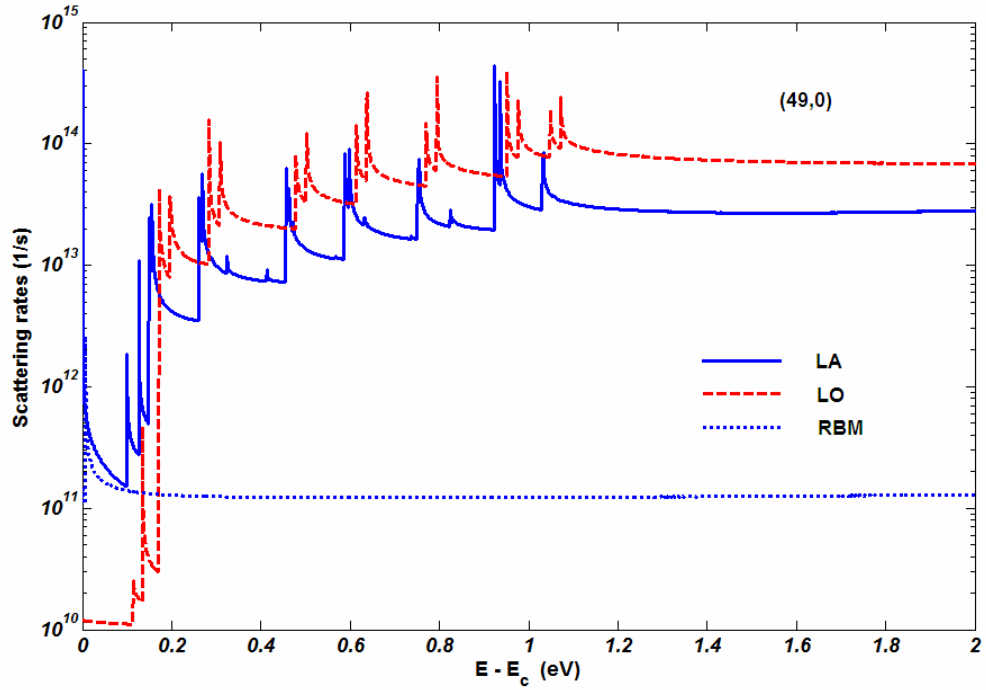
Table 3.1: Semiconducting zigzag CNTs included in this work, and their grouping. The CNTs selected cover a large range of diameter, and include both semiconducting zigzag families. CNT $(3p,0)$ is metallic for all p , where p is an integer (see Chapter 1 for details).

3.1 Scattering rates

Figure 3.1 shows the various electron-phonon scattering rates for the lowest subbands for (a) CNT (10,0) and (b) CNT (49,0) at a temperature of 300K. The energy is measured from the bottom of the subbands. All three phonon scattering rates, LA, LO, and RBM are depicted. The cause of the sharp peaks observed in the scattering rates – due to an electron transition to the bottom of a subband - has already been discussed in Chapter 2. It can be seen that the scattering rates for CNT (49,0) are lower than those for CNT (10,0). This is partially attributed to the higher linear mass density for CNT (49,0) (i.e. grams/cm). For CNT (10,0) the strong LA and LO emission peaks around 0.16 eV correspond to intersubband electron transitions from subband $\nu = 7$ to $\nu = -7$. The next set of emission peaks around 0.8 eV corresponds to intersubband transitions from $\nu = 7$ to $\nu = \pm 6$. However, for CNT (49,0) the first set of LA phonon peaks around 0.15 eV corresponds to intersubband phonon absorption and emission processes for transitions from subband $\nu = 33$ to $\nu = 32$. Followed by that, LA and LO phonon emission peaks for transitions from subband $\nu = 33$ to $\nu = -33$ appear around 0.16 eV. This change in order of the scattering processes for CNT (49,0) compared to that of CNT (10,0) is primarily due to a decrease in intersubband energy differences with increasing tube diameter. However, the energy of the phonon branch corresponding to the transition from subband ν_1 to subband $-\nu_1$ remains essentially unchanged with increasing tube diameter, and therefore this transition occurs at nearly the same energy for both the CNTs, as seen in Figure 3.1a. Figure 3.2 shows the scattering rates as a function of electron wave vector k directed along the tube axis. This depiction of scattering rates as a function of the electron



(a)



(b)

Figure 3.1: Lowest subbands scattering rates versus energy for (a) CNT (10,0) and (b) CNT (49,0) at 300K. Energy is measured from the bottom of the subbands. Sharp peaks are the result of electron transitions to the bottom of various subbands.

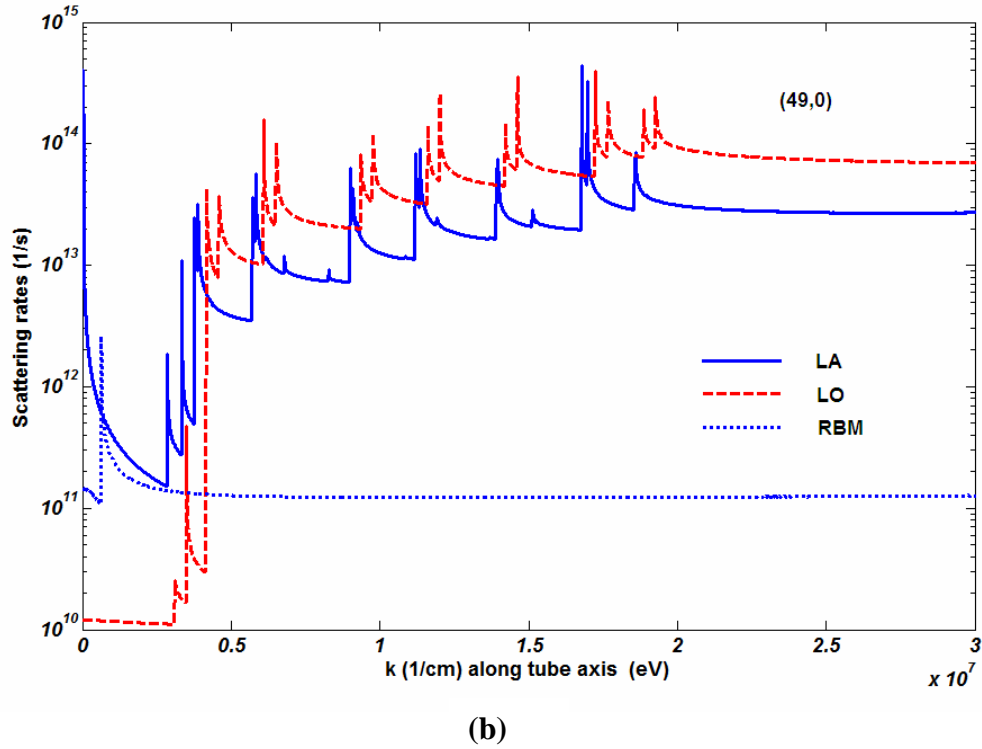
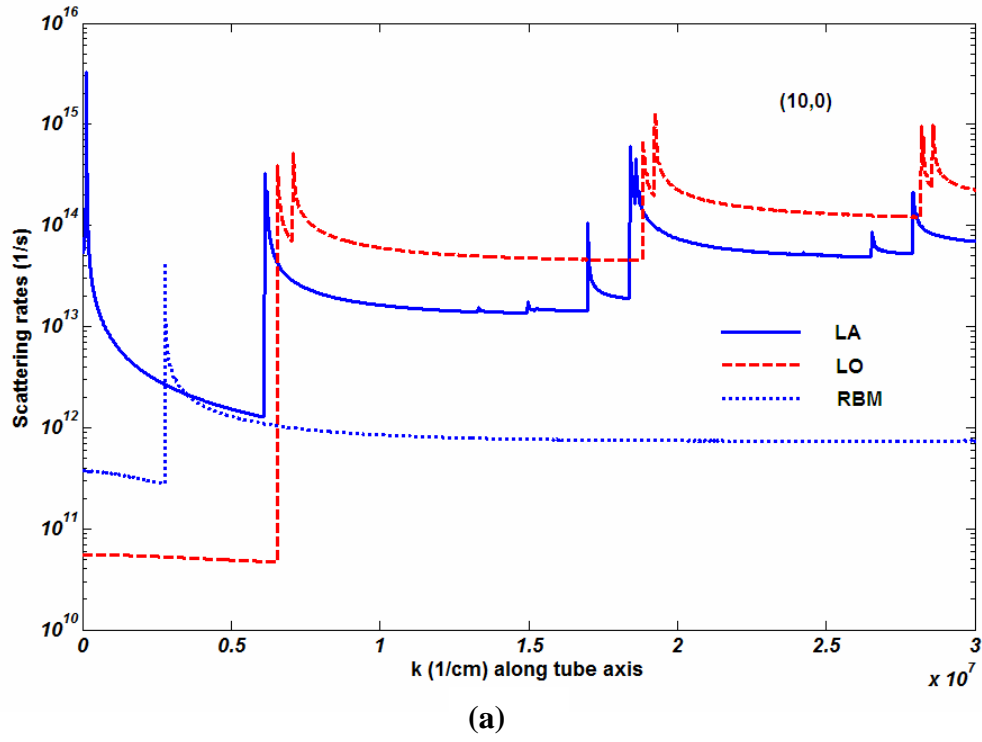


Figure 3.2: Lowest subband scattering rates for (a) CNT(10,0) and (b) CNT(49,0) at 300K. Scattering rates are depicted versus k directed along the tube axis.

wave vector will be useful later when we analyze various steady-state and transient results.

3.2 Steady-state

3.2.1 Field dependent mobility

3.2.1.a Velocity and mobility behavior with electric field

Figure 3.3 shows the steady-state average drift velocity of electrons as a function of electric field for CNTs (10,0) and (11,0) obtained at 300K. Looking at the figure, we can divide the curves into 3 distinct regions. The first is a nearly linear region where the average electron velocity appears to be an almost linear function of the applied electric field. The second region is one of near saturation, where the electron velocity shows little or no variation with the applied electric field. The third region is more obviously visible for CNT (10,0), and absent for CNT (11,0). It is one of a negative differential mobility (NDM), where the velocity is seen to decrease with increasing electric field. Figure 3.4 shows the average mobility (drift velocity/electric field) as a function of electric field for the two CNTs mentioned above. It may be observed that the mobility decreases by more than an order of magnitude for the electric fields considered.

The behavior of the average electron drift velocity with electric field may be deduced as follows. Initially electrons are present within the lowest subbands. When a small electric field is applied, electrons in the subbands gain a net average momentum in the direction of the electric field. When the scattering is low (as slightly away from the Γ -

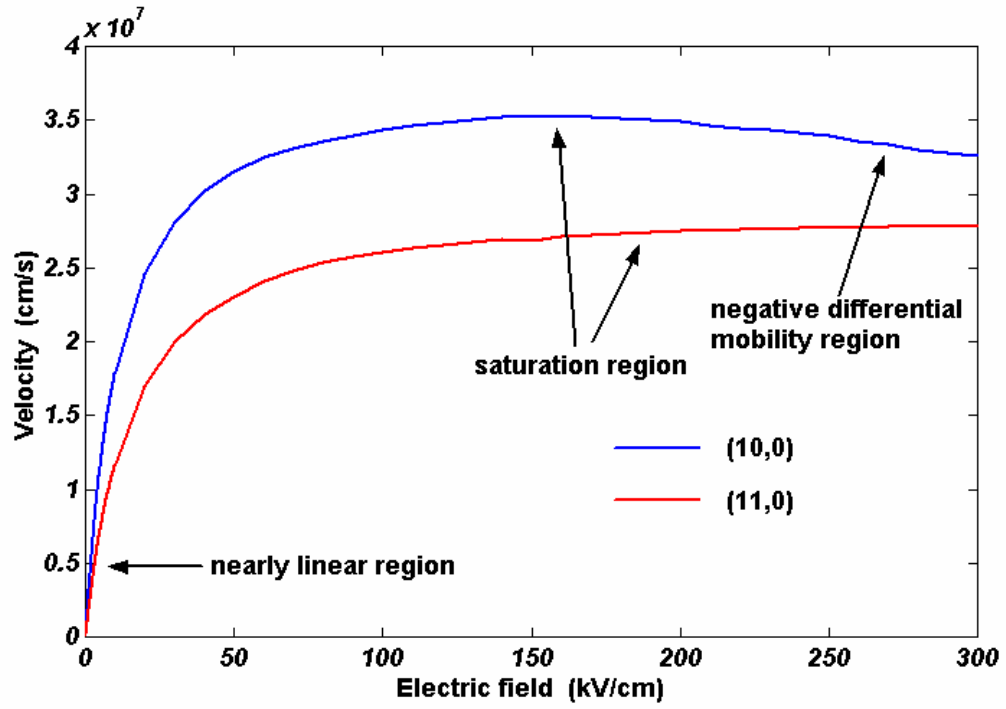


Figure 3.3: Average electron drift steady-state drift velocity as a function of electric field for CNT (10,0) and (11,0) at 300K. The presence of NDM region is clearly visible for (10,0), but is absent for (11,0). For explanation see text.

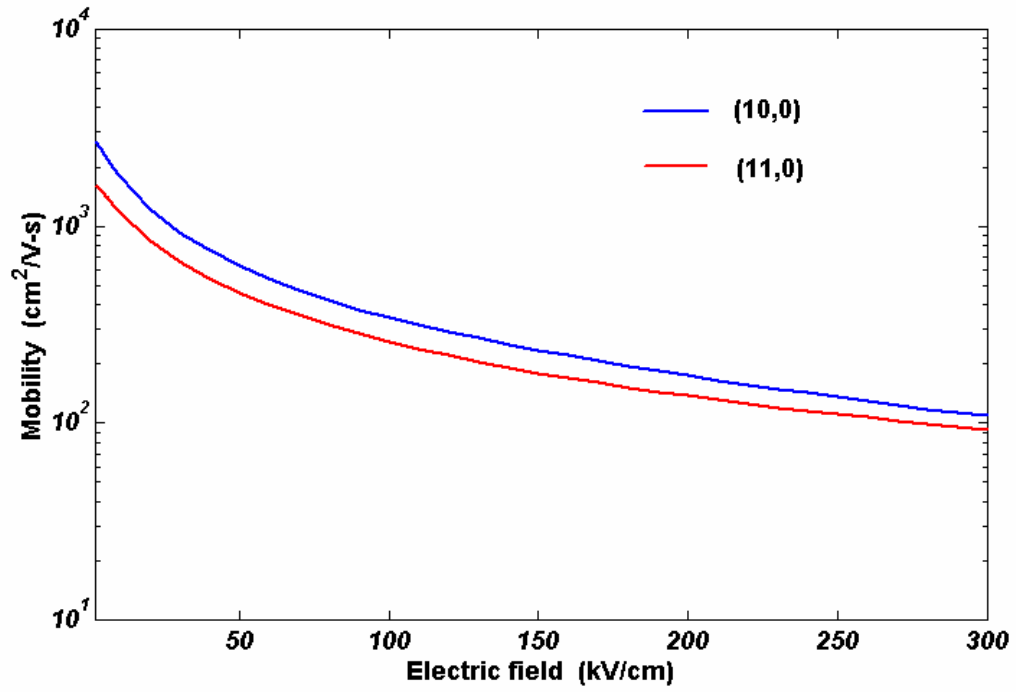


Figure 3.4: Variation of the average electron mobility with electric field for CNTs (10,0) and (11,0). The mobility is seen to vary by over a magnitude in the field range considered.

point in Figure 3.2), the increase in net average momentum of the electron distribution is very nearly directly proportional to the electric field, if a constant relaxation time is assumed. The result is a displaced Maxwellian electron distribution in the direction of electric field and, consequently, a nearly linear variation of velocity with the electric-field. The situation continues until an electric field is reached where the steady-state electron momentum distribution reaches the first set of intersubband LA emission peaks. This occurs for CNT (10,0) near $k \sim 6 \times 10^6 \text{ cm}^{-1}$ and involves electron transitions from subbands $\nu_i = \pm 7$ to $\nu_f = \mp 7$ due to emission of a $\mu = \mp 6$ LA phonon. At only slightly larger k , $\mu = \pm 6$ ($\nu_i = \pm 7$ to $\nu_f = \mp 7$) and $\mu = 0$ (intrasubband $\nu_i = \pm 7$ to $\nu_f = \pm 7$ transitions) LO phonon emission processes become possible. All of these strong inelastic scattering events prevent electrons from gaining momentum and induce the observed saturation of the ensemble drift velocity. Figure 3.5 shows the variation of the steady-state electron momentum distribution with the electric field for CNT (10,0). The presence of a scattering barrier around $k \sim 6 \times 10^6 \text{ cm}^{-1}$ is clearly seen. Once the distribution reaches this barrier at approximately 50 kV/cm, there is no significant change in the distribution function until an electric field of about 150 kV/cm is reached. It is only after that, that the electrons are able to overcome the barrier in significant numbers. The saturation of current, observed in some recent high-voltage experiments [44], may be attributed to this saturation of electron velocity. Moreover, recent numerical modeling of semiconducting zigzag CNTs, incorporating a multi-band Boltzmann approach also predicts the appearance of velocity saturation at intermediate to high electric fields [21].

The NDM phenomenon seen in Figure 3.3 for CNT (10,0) is similar in nature to the one observed in various other semiconductors, notably, GaAs [41]. It is caused by

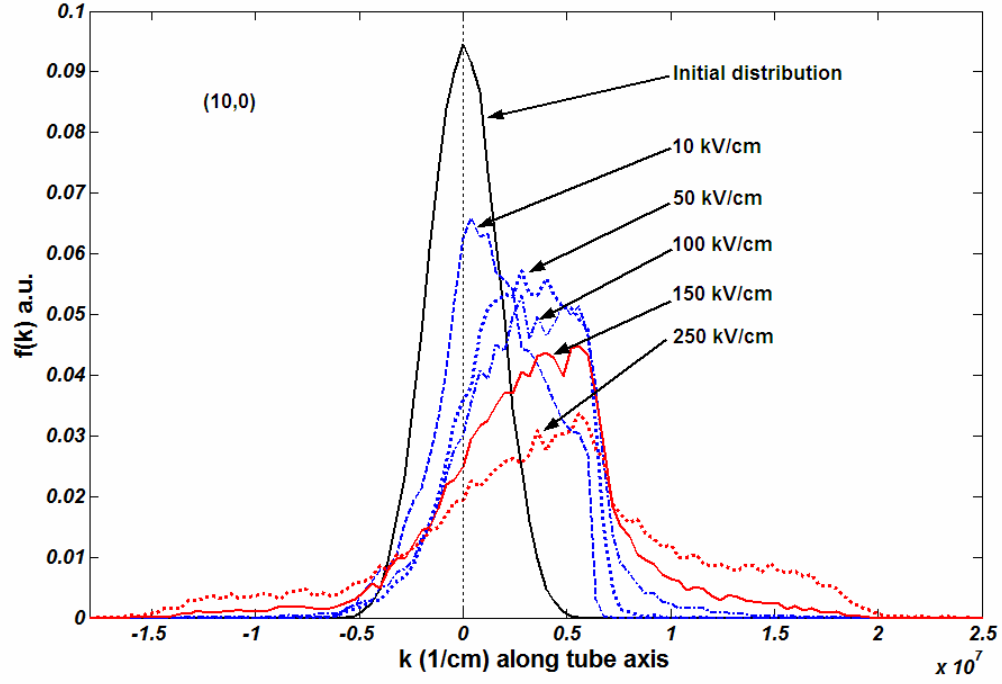
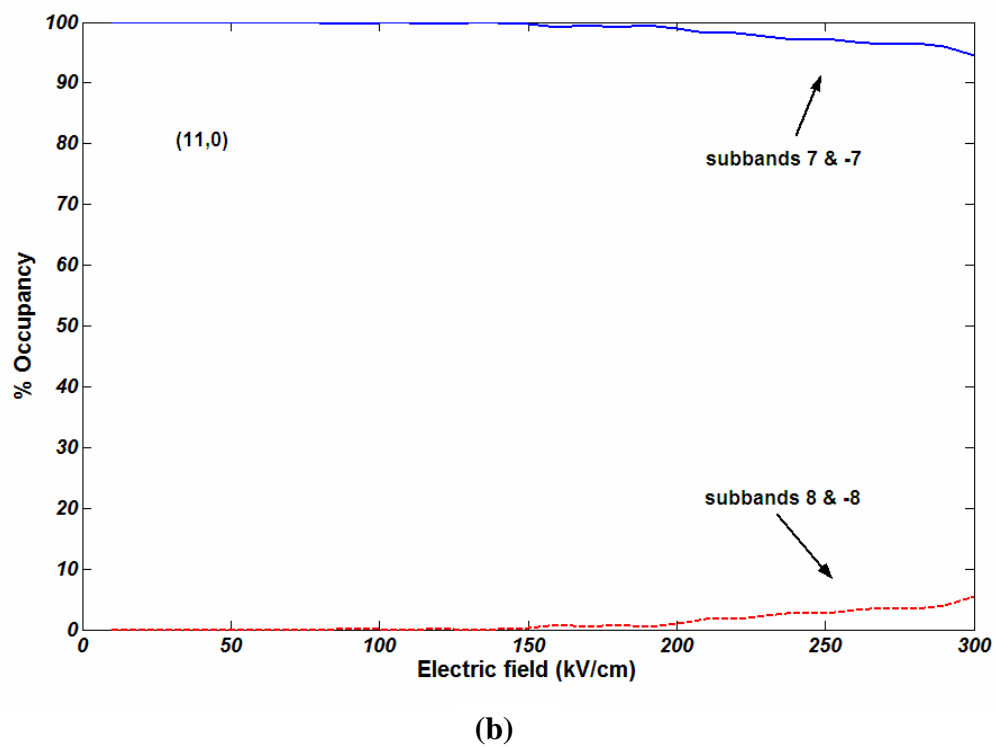
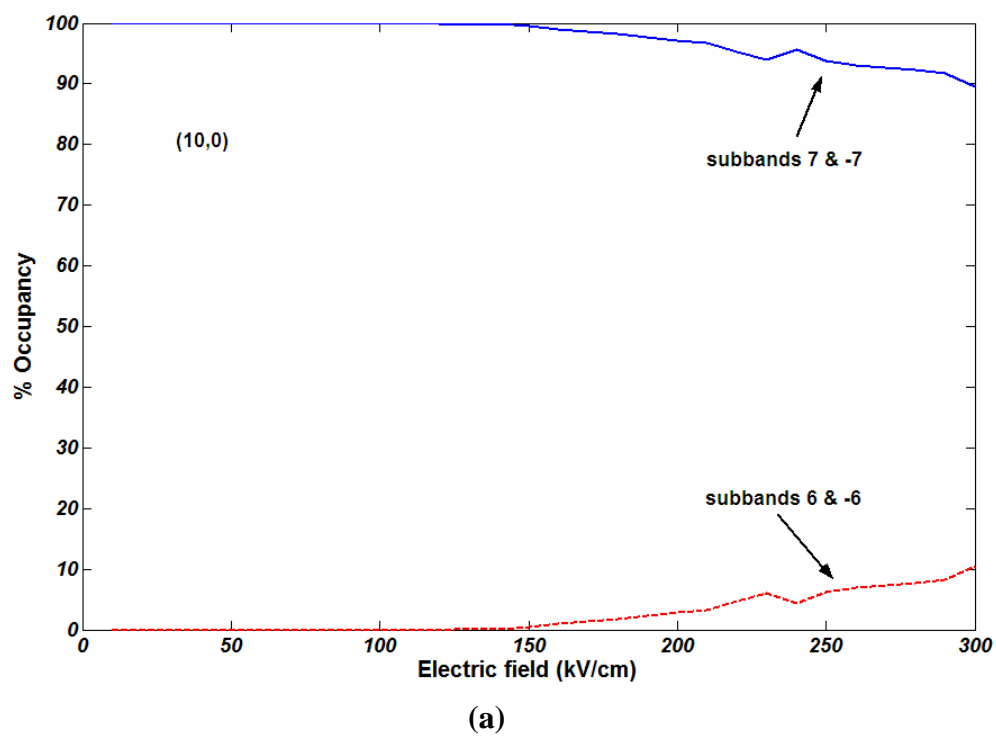


Figure 3.5: Steady-state momentum distribution for CNT (10,0) at various electric fields. The presence of the scattering barrier discussed in the text is clearly visible around $k \sim 6 \times 10^6 \text{ cm}^{-1}$. This barrier prevents any significant electron momentum gain until a high electric field is reached.

electrons making a transition from a lower energy and lower effective mass subband to a higher energy and higher effective mass subband. Because of the increase in effective mass of some electrons in the ensemble due to this transition, the average velocity of the ensemble decreases with increasing electric field. The absence of NDM, however, for CNT (11,0) is not due to an absence of electron transitions to higher subbands, but rather to the similarity of electron effective masses in the two subbands (the effective mass for the lowest 2 subbands (each subband four-fold degenerate including spin) for CNT (10,0) are approximately $0.081m$ and $0.377m$, while those for CNT (11,0) are $0.131m$ and $0.134m$, where m is the electron rest mass). This is further corroborated through Figure 3.6, which depicts the relative electron occupancy of various subbands as a function of applied electric field at 300K for (a) CNT (10,0), (b) CNT (11,0), and (c) CNT (49,0). As can also be seen from Figure 3.6, even at very high electric fields, higher energy subbands show little to no occupancy. This justifies the inclusion of only the lowest 3 and lowest 4 subbands (each subband four-fold degenerate including spin) for CNTs (10,0) and (11,0) respectively in the EMC CNT simulators. For larger diameter CNTs, the lowest 7 subbands are included.

3.2.1.b Diameter dependence of the velocity

Figure 3.7 shows the velocity vs. electric field plots at room temperature for all the six CNTs mentioned in Table 3.1. This allows us to visualize the effect of the tube diameter on the steady-state electron drift velocity. As can be seen, $(3p+2,0)$ CNTs have a lower velocity at the same electric field compared to that of the $(3p+1,0)$ CNTs for the same p . The difference becomes progressively smaller with increasing diameter, as the



(continued)

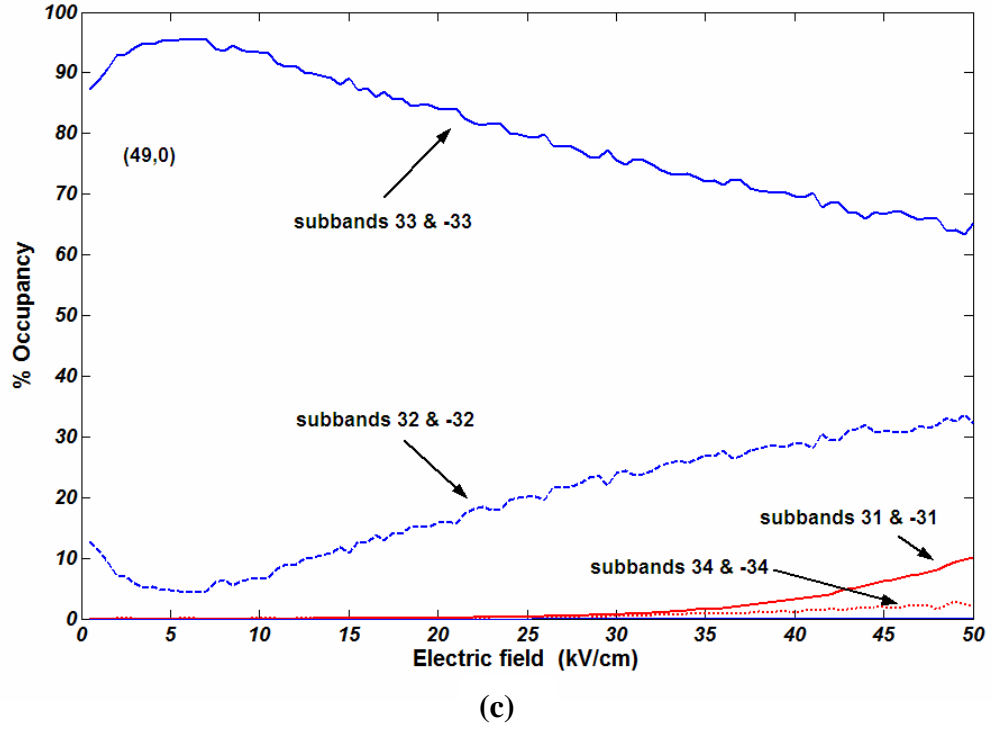


Figure 3.6: Electron occupancy of various subbands as a function of electric field for (a) CNT (10,0), (b) CNT (11,0), and (c) CNT (49,0). Even at relatively high electric fields few subbands are occupied, justifying the limited number of subbands included in the EMC simulation for the CNTs considered.

relative difference in electron effective masses decreases (Figure 1.14). Both families show saturation of the electron velocity at intermediate electric fields. The saturation electric field, E_{sat} , is vastly different for CNTs with different diameter. E_{sat} is found to decrease with increasing tube diameter, as seen in Figure 3.7. This is primarily because the smaller effective mass in larger diameter CNTs allows electrons to gain momentum quickly from the electric field, and reach the set of scattering peaks that cause velocity saturation.

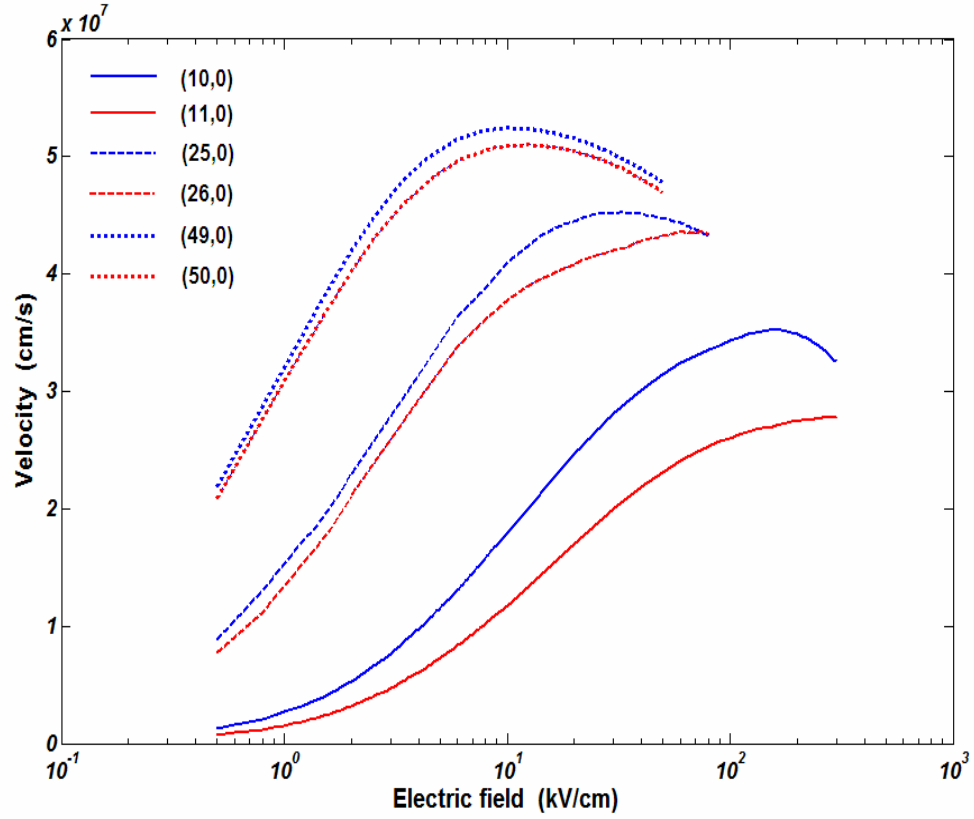
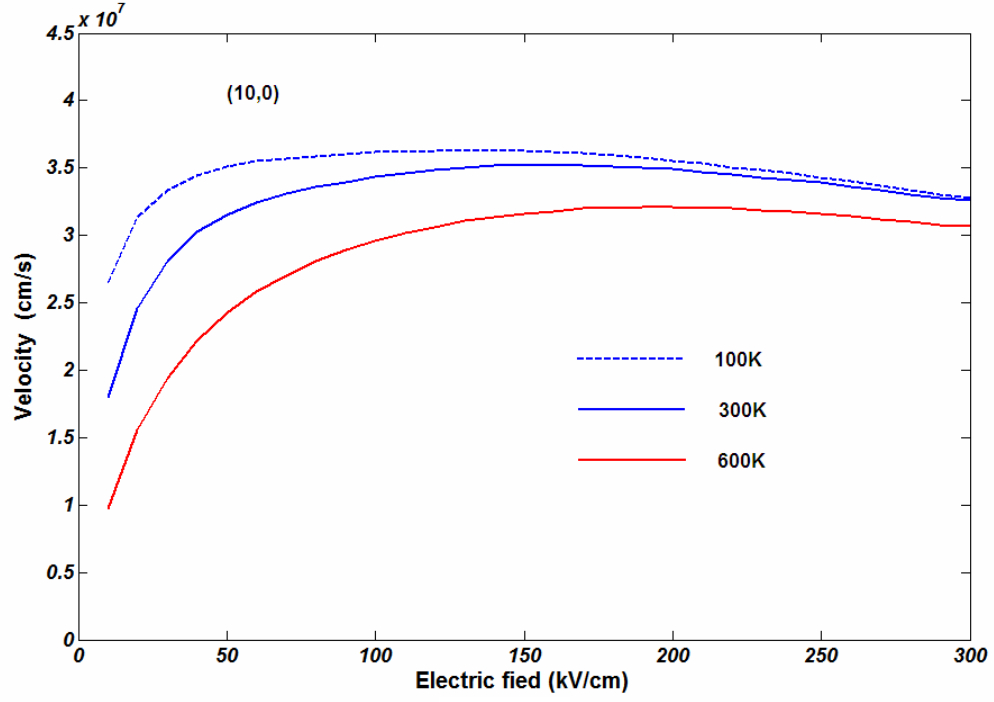


Figure 3.7: Steady-state electron velocity versus electric field for various CNTs encompassing a broad range of diameter, at 300K. Smaller diameter CNTs have a lower velocity in accordance with their lower electron effective mass. $(3p+1,0)$ CNTs have higher velocity than $(3p+2,0)$ CNTs for the same integer p . A lower velocity-saturation electric field is observed for larger diameter CNTs.

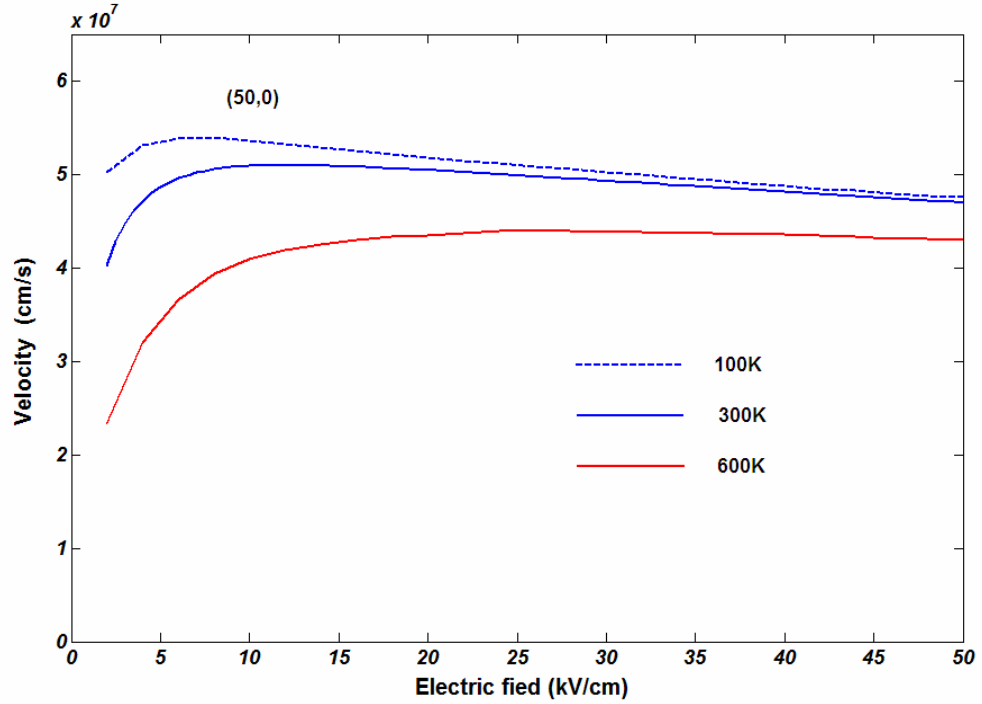
Another important noticeable transport phenomenon is the NDM. As can be seen from Figure 3.7, smaller diameter $(3p+1,0)$ CNTs show a more pronounced NDM than do smaller diameter $(3p+2,0)$ CNTs. However at a larger diameter, CNTs of both families show NDM at relatively high electric fields. From Figure 3.6 it can be seen that for the small diameter tube, CNT (10,0), the electrons reside in the lowest subbands until a relatively high electric field is reached. However, for the large diameter tube, i.e. CNT (49,0), the second subband populates at relatively low electric fields and the other higher subbands begin to be occupied at higher electric fields. This is due to the reduction of intersubband spacing with increasing tube diameter as seen in Figure 1.12 and 1.13. Thus, due to a greater occupancy of higher subbands with larger effective mass (as seen in Figure 1.14), the NDM effect is more pronounced for large diameter CNTs.

3.2.1.c Temperature dependence of the velocity

Figure 3.8 depicts the steady-state electron drift velocity relation with electric field for CNTs (a) (10,0), and (b) (50,0) at temperatures of 100K, 300K, and 600K. The dependence on temperature is found to be strong in the low to intermediate electric field regimes, and becomes negligible in the high field regime. This behavior has also been found to be essentially independent of tube diameter. In the low to intermediate electric field regime, the electrons are mostly held in the low k region by the scattering barrier (Figure 3.5), where scattering rates are dominated by phonon absorption and hence are very sensitive to temperature. Therefore, with an increase in temperature, and subsequent increase in scattering rates, the electron velocity decreases. At high electric fields, electrons gain sufficient energy to overcome the scattering rate barriers. In this regime,



(a)



(b)

Figure 3.8: Effect of temperature on steady-state electron velocity for (a) CNT (10,0), and (b) CNT (50,0). Temperature is seen to have a strong influence at low and intermediate electric fields. The effect decreases with an increase in the field.

the total scattering rate is dominated by phonon emission, which is less sensitive to temperature, and hence the electron velocity shows little change with a variation in temperature. This is illustrated in Figure 3.9, which shows the total scattering rates for CNT (10,0) at temperatures of 100K and 300K. As can be seen, beyond $k \sim 6 \times 10^6 \text{ cm}^{-1}$, scattering rates show insignificant change, even though the temperature has increased by a factor of three.

3.2.1.d Impact of individual scattering rates on velocity

LO phonons are the most important scattering mechanism in a CNT at intermediate and high electric fields, where they define the behavior of charge transport. In Figure 3.10a, we see the average steady-state electron drift velocity as a function of electric field in the presence and absence of LO phonon scattering. Absence of LO scattering results in a sharper and earlier NDM, and a near absence of velocity saturation. This is because without LO scattering, electrons quickly gain enough momentum to make a transition to the next higher subbands, as seen in Figure 3.10b. In the field range depicted in Figure 3.10b, the next higher subbands show negligible occupancy with LO scattering, while there is significant occupancy when LO scattering is not operating.

Figure 3.11 shows the average steady-state electron velocity as a function of the applied electric field for CNTs (a) (10,0), and (b) (11,0) at room temperature, both with and without RBM phonon scattering. The effects of RBM phonon scattering on steady-state transport are small but not insignificant. In the case of CNT (10,0), this extra scattering mechanism causes a lowering of the electron velocity at low and moderate electric fields. At high electric fields, the electron velocity is seen to be almost independent of RBM

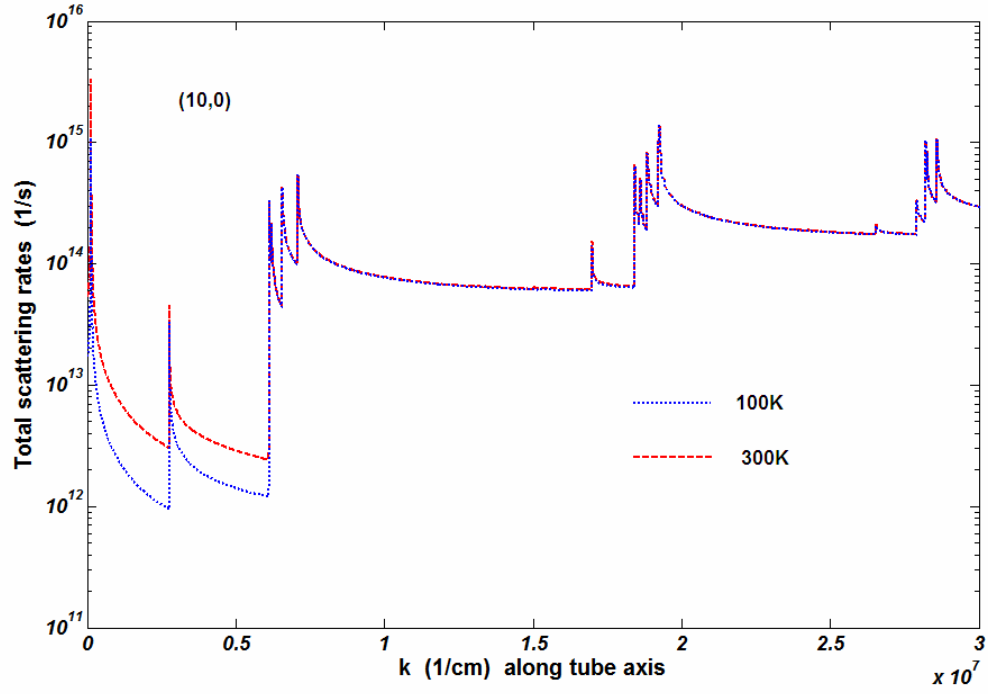
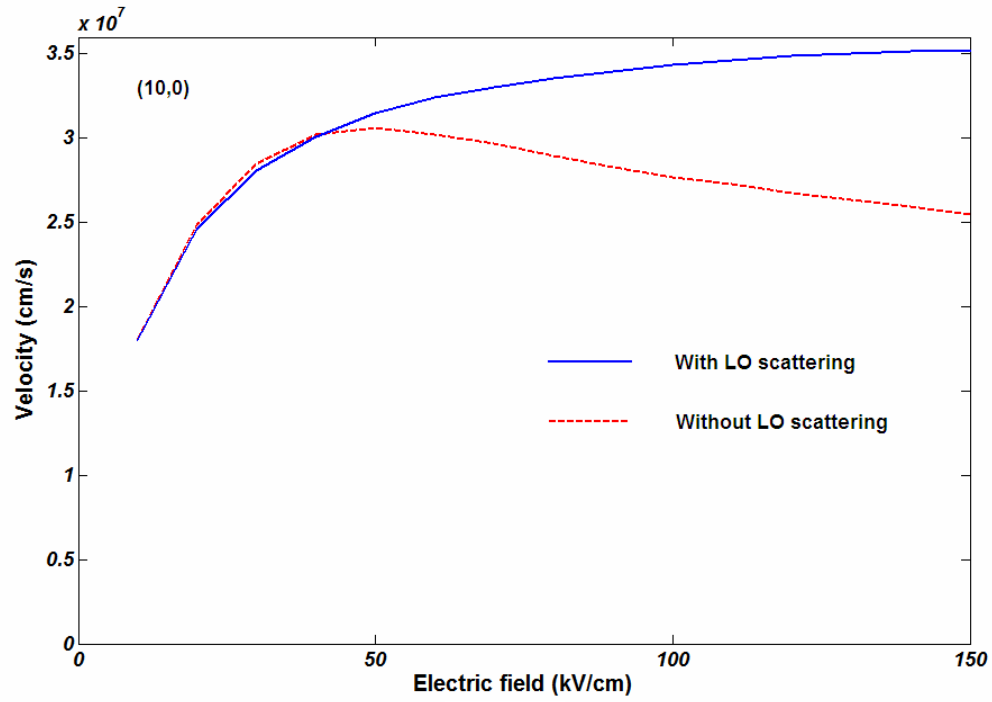
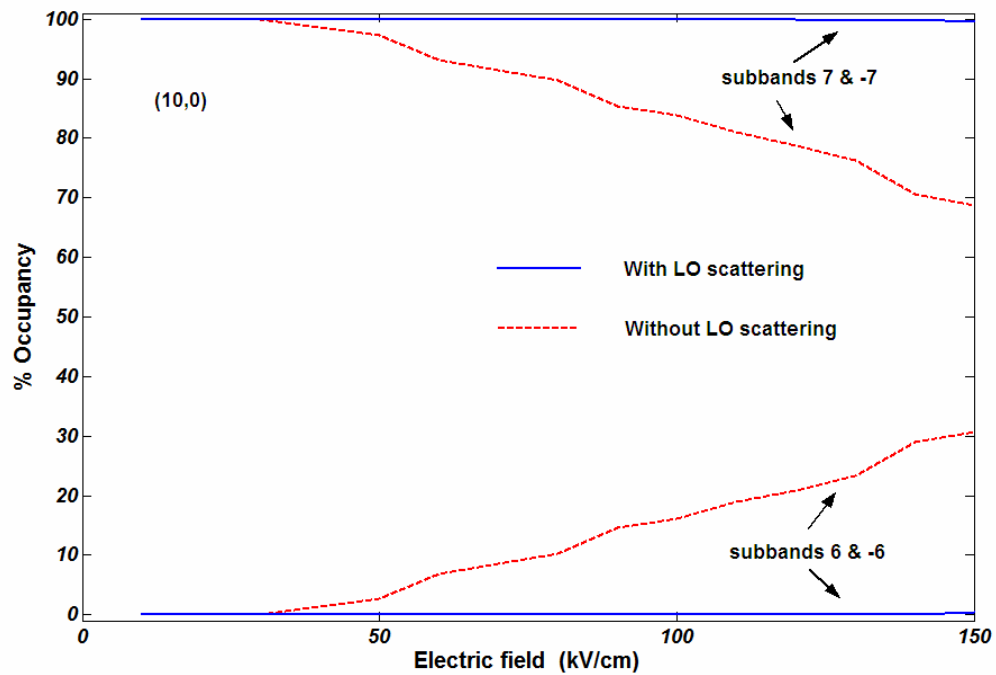


Figure 3.9: Total electron-phonon scattering rates for CNT (10,0) at 100K and 300K. In the low k regime, scattering rates are relatively more sensitive to temperature than in the high k regime. This makes the electron velocity at high electric fields less sensitive to temperature change.

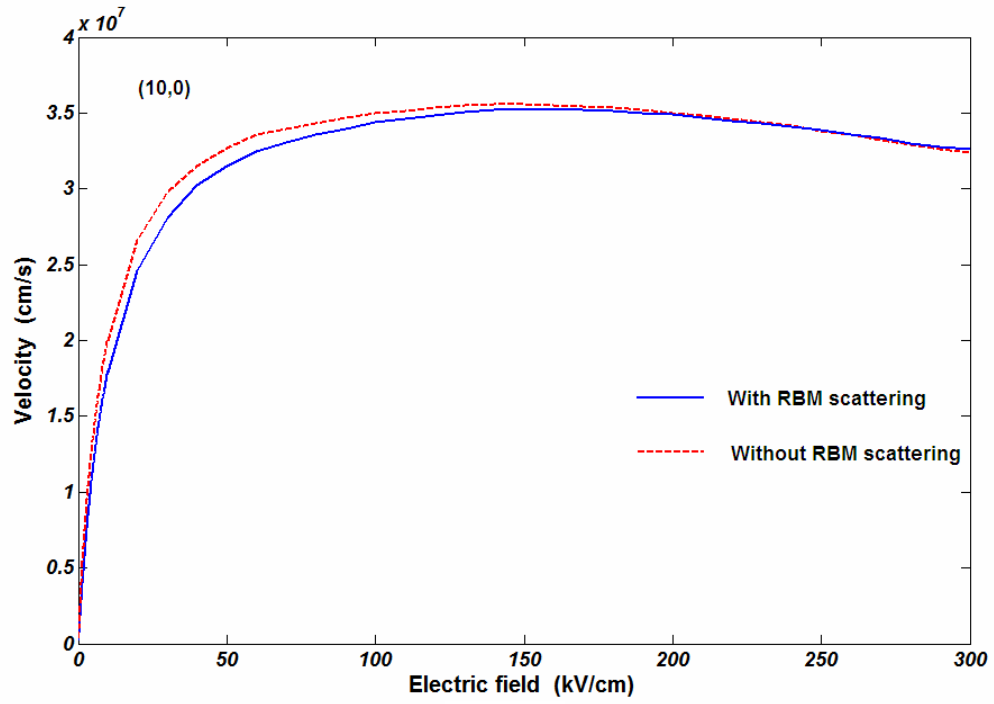


(a)

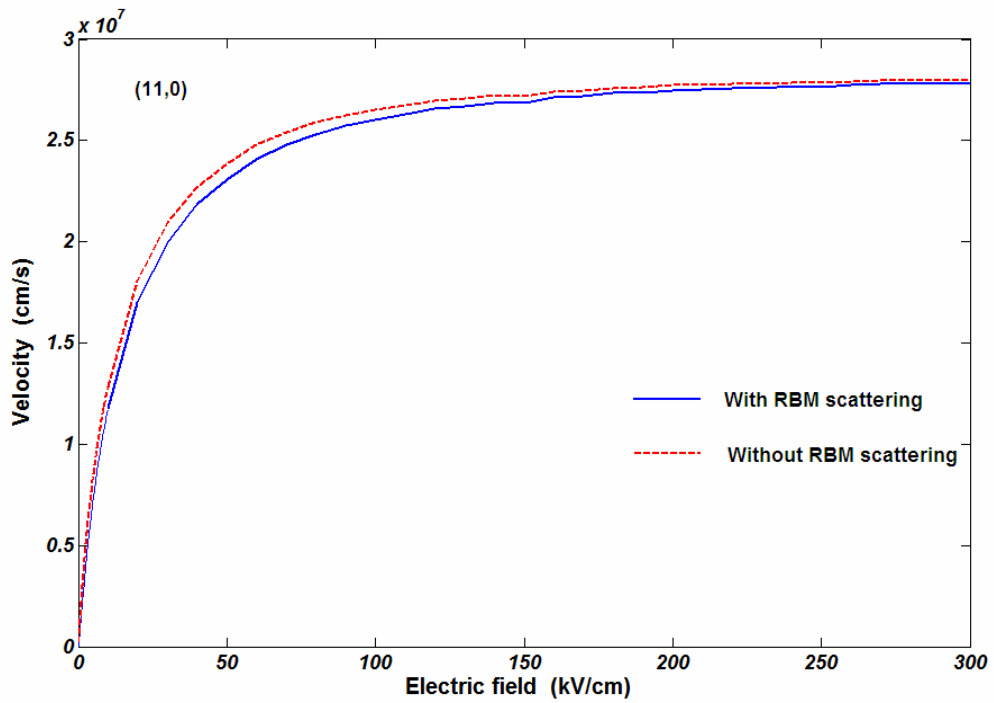


(b)

Figure 3.10: Effect of LO phonon scattering for CNT (10,0) on (a) steady-state velocity, and (b) electron occupancy. LO phonons cause electron velocity to saturate because they prevent electrons from gaining sufficient momentum to make a transition to higher subbands.



(a)



(b)

Figure 3.11: Velocity versus applied field for (a) CNT (10,0), and (b) CNT (11,0) with and without RBM scattering. The effect of RBM scattering is seen primarily in the low to intermediate field regime.

phonon scattering. Since velocity saturation occurs mainly because of the scattering barrier imposed by LA and LO phonon emission processes near $k \sim 6 \times 10^6 \text{ cm}^{-1}$, the impact of RBM phonon scattering is seen primarily in the field range below velocity saturation. RBM phonon scattering is less important in the NDM region. Though RBM scattering does cause a slight lowering of the observed average steady-state velocity for both CNTs, its influence is slightly weaker in CNT (11,0) compared to CNT (10,0). This is mainly attributed to the fact that the RBM deformation potential for CNT (11,0) is only about 73% of that for CNT (10,0), resulting in a lower RBM phonon scattering rate for the former.

3.2.2 Low-field mobility

Low-field mobility is a very important parameter from a device application point of view. Its determination provides the circuit designer with fundamental information about the way a device or material should be incorporated in a circuit. As an example, in a Si Complementary MOSFET (CMOS), the p-channel MOS transistor is usually designed to be wider than the n-channel MOS transistor. This is because the hole mobility in silicon is smaller, and therefore to carry the same amount of current, the width of the p-channel transistor has to be larger than that in the n-channel transistor.

Determination of the low-field mobility through EMC simulation is usually not very accurate, as was discussed in Chapter 2. Therefore, in order to determine the low-field mobility for CNTs, the iterative Rode's method was employed [45]. The steady-

state and spatially homogeneous Boltzmann Transport Equation (BTE) under low electric fields can be solved efficiently using this technique. In this work the low-field mobilities of different CNTs are calculated through the Rode's method by considering only the lowest conduction subband. For simplicity the lowest subband is approximated by

Equation 2.2, $e(1 + \alpha e) = \frac{\hbar^2 k^2}{2m^*}$, where α is the non-parabolicity factor. As a very low

electric field does not result in any significant electron occupancy for larger k-values, only k-values close to the Γ point need be considered. In this regime, there is a less than 1% difference between the more accurate band structure obtained through the tight-binding method [3], and the analytical assumption represented by Equation 2.2, for the various CNTs considered. While the inclusion of only the lowest subbands is appropriate for the CNTs considered here, more subbands may need to be included for larger diameter tubes, or for higher temperatures. This is because in significantly larger diameter CNTs, subbands are expected to be very closely spaced (Figure 1.12), and therefore, even at equilibrium at intermediate temperatures (for example room temperature), higher subbands may show significant electron occupancy. When this happens, the effect of inter-subband coupling, through the inter-subband scattering rates, needs to be incorporated within Rode's method. Even for the larger diameter CNTs considered in this work, this situation may arise at significantly higher temperatures. For the evaluation of the low-field mobility, all three electron-phonon scattering mechanisms (LA, RBM, and LO) are taken into account. As can be deduced from Figure 3.1, the low-field mobility is mainly affected by LA and RBM scattering. LO scattering is relatively insignificant around the Γ point.

The low-field mobility as a function of diameter for different temperatures is plotted

in Figure 3.12. It can be seen that for a fixed temperature the low-field mobility increases with increasing CNT diameter. This is due to a reduction in the total scattering rate. As was mentioned previously, the scattering rate decreases with increasing tube diameter, to a large extent due to an increase in linear mass density. Another notable feature is that the mobility of the $(3p+1,0)$ CNT is greater than that of the $(3p+2,0)$ CNT for all p . This is attributed to the higher effective mass of the $(3p+2,0)$ CNT. In addition, for a given CNT, the scattering rate increases with decreasing temperature, due to the reduction in acoustic and RBM scattering rates. These calculated low-field mobility values are consistent with previous theoretical and experimental work [21,46].

To investigate the effect of RBM electron-phonon scattering on low-field mobility, results with and without consideration of RBM phonon scattering are plotted as a function of CNT diameter in Figure 3.13. Also shown is the relative difference between the two results, which turns out to be nearly independent of the tube diameter. Although we have observed that the RBM scattering rate decreases with increasing tube diameter, this decrease is matched by the simultaneous decrease in the LA scattering rate, as seen in Figures 3.1 and 3.2. Therefore, the relative difference in the low-field mobility due to the inclusion or exclusion of RBM scattering remains essentially constant.

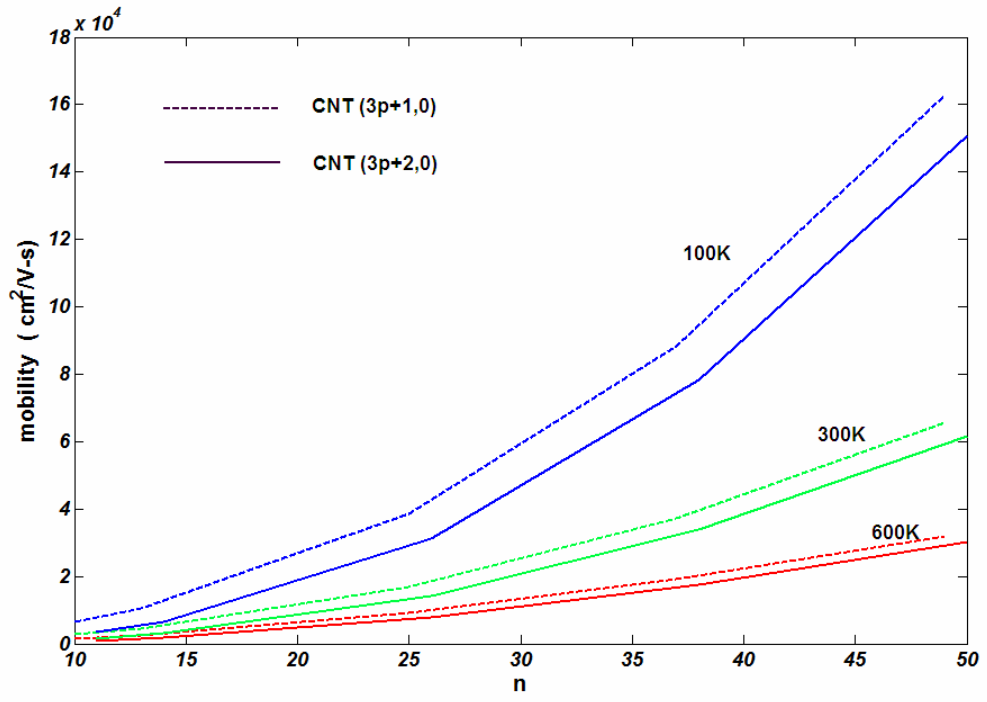


Figure 3.12: Low-field mobility as a function of temperature and n . The diameter of CNT $(n,0)$ is directly related to n . The mobility difference between $(n=3p+1,0)$, and $(n=3p+2,0)$ CNTs follows from their different electron effective masses.

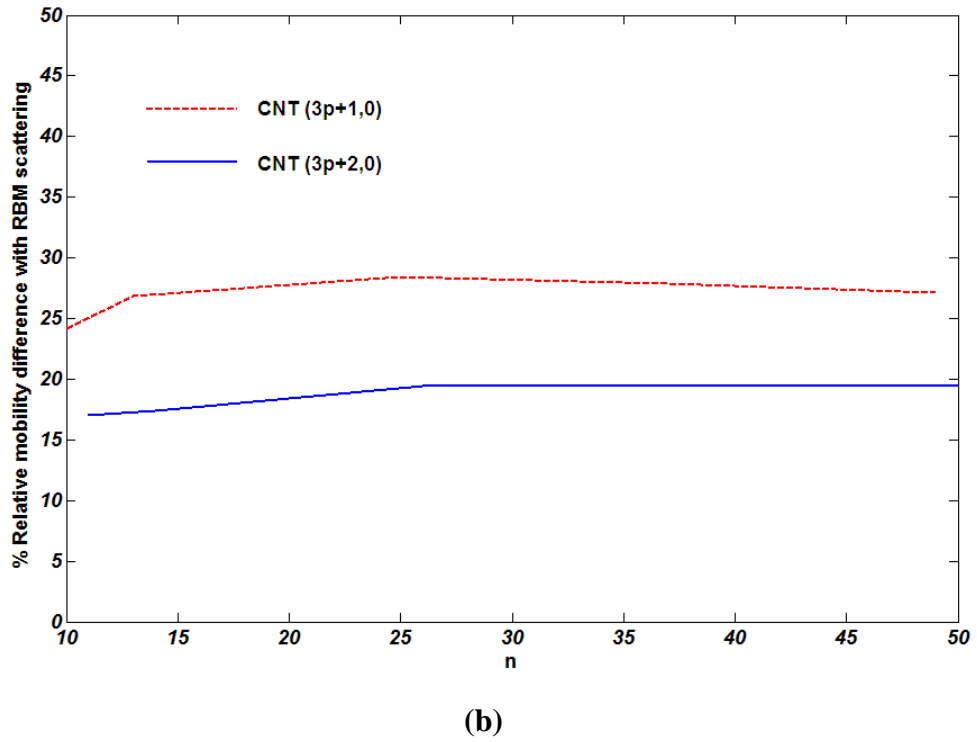
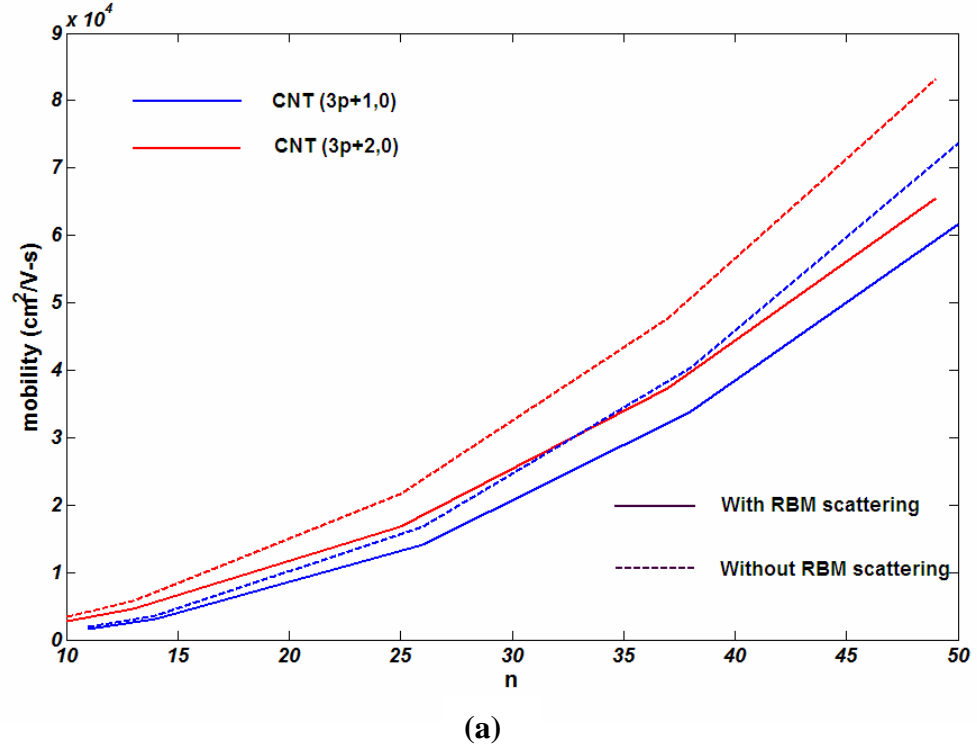


Figure 3.13: Effect of RBM scattering on low-field mobility. (a) RBM scattering causes a degradation of mobility, but (b) the relative difference is essentially independent of tube diameter. This is because the LA scattering rate decrease matches the RBM scattering rate decrease.

3.3. Transient phenomenon

3.3.1 Transient velocity

3.3.1.a Average transient velocity response

The investigation of transient charge transport phenomena in CNTs is extremely important. It is more than likely that CNTs will be utilized in applications where the charge carriers will not relax to steady-state. A focus on transients has led to the observation of interesting phenomena that are a result of the streaming motion within the 1-D electron dispersion of the CNTs [47]. Figure 3.14 depicts the evolution of the average drift velocity of the electron ensemble with time for CNT (49,0) at room temperature and at various electric fields after the injection of thermal electrons. As can be seen, the transient velocity response is oscillatory in nature at intermediate fields. The oscillations eventually damp out to a steady state value that depends upon the applied electric field. This phenomenon is not observed in conventional semiconductors (for example Si, and GaAs), where oscillations are absent [41]. The time period for the oscillations is seen to depend on the electric field, and is nearly equal to twice the time it takes the average velocity to reach the first peak, making the case for a nano-scale voltage-controlled current oscillator. The reason for the oscillations may be described with the help of Figure 3.2. As electrons gain crystal momentum through the electric field, they experience acoustic scattering mainly due to the acoustic phonon branch $\mu = 0$, and RBM scattering. However, after an electron in the lowest subbands has gained enough energy to emit $\mu = \pm 32$ LA or $\mu = 0, \pm 32$ LO phonons, it will suffer such a scattering process with high probability and lose nearly all of its energy and crystal momentum.

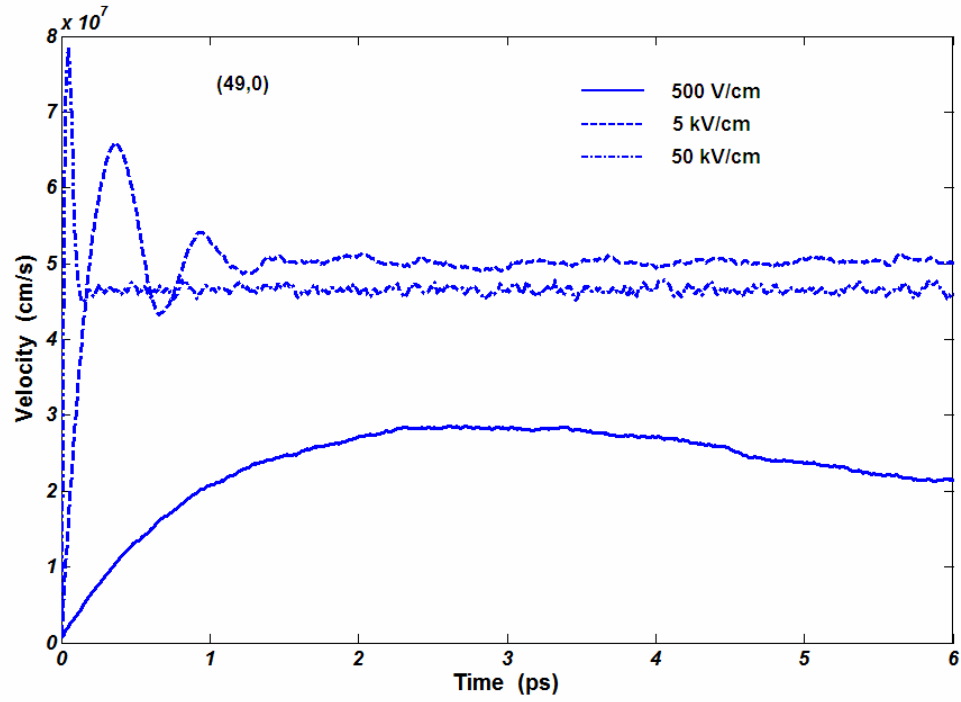


Figure 3.14: Evolution of the average transient velocity with time for CNT (49,0) at various electric fields and 300K. The presence of oscillations in the velocity response is clearly observed at intermediate fields. The time period of the oscillations is also seen to be field dependent.

Subsequently it is again accelerated by the electric field. Consequently the ensemble average velocity oscillates until other scattering events that occur with lower probability facilitate the establishment of a steady state distribution. The entire process can be visualized with the help of Figure 3.15, which shows the distribution function $f(k)$ of the ensemble at various times for CNT (49,0). It can be seen that the distribution bounces back-and-forth before settling down to a steady-state. The presence of a scattering rates barrier at $k \sim 4 \times 10^6 \text{ cm}^{-1}$ is reflected in the sharp features in $f(k)$ around that k -point. At relatively low electric fields, electrons have sufficient time to interact with the $\mu = 0$ LA and RBM phonons, which suppresses the oscillations, as can be seen in Figure 3.14. At sufficiently high electric fields, electrons gain enough momentum through the action of the electric field to overcome the scattering rate barrier, again resulting in little or no observable velocity oscillations.

A simple classical treatment of the electron motion at intermediate fields results in the following prescription to determine the time period of oscillations:

$$t_p = \frac{2\hbar k_b}{QE} \quad (3.1)$$

where t_p is the time period of transient velocity oscillations, E is the applied electric field directed along the CNT axis, Q is the electron charge, and k_b is the point at which the (optical emission) scattering barrier occurs ($k_b \sim 4 \times 10^6 \text{ cm}^{-1}$ for CNT (49,0)).

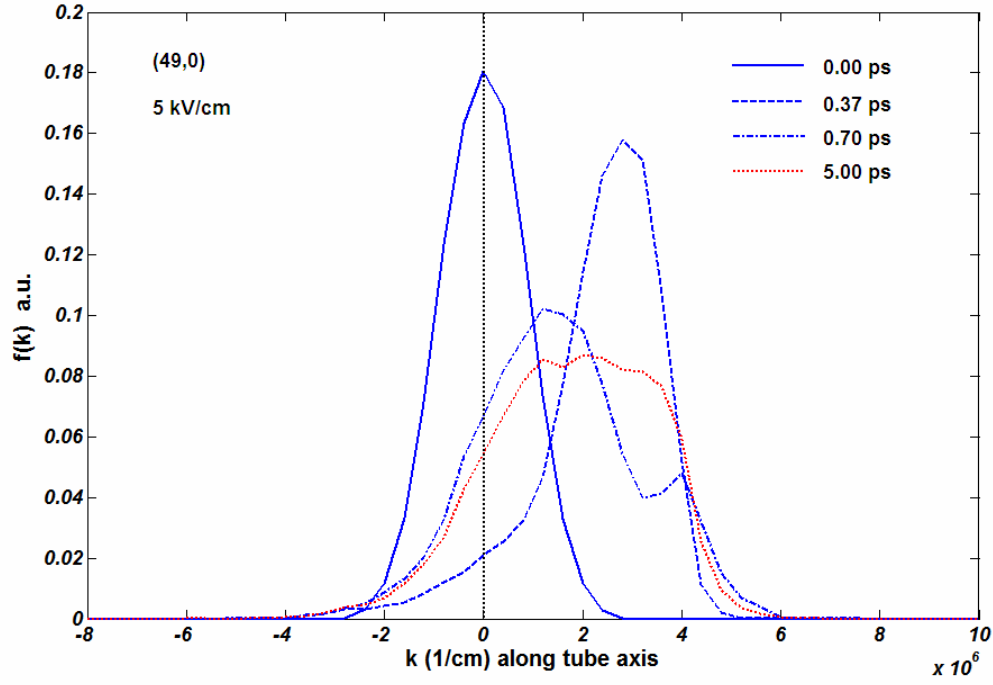


Figure 3.15: Evolution of the electron momentum distribution function with time for CNT (49,0) at 5 kV/cm and 300K. The distribution function is seen to “bounce” between $k = 0 \text{ cm}^{-1}$ and $k \sim 4 \times 10^6 \text{ cm}^{-1}$, before settling down. This results in the observed damped oscillation in the transient velocity oscillations.

It is possible to further simplify Equation 3.1 by considering the fact that in all the CNTs mentioned in Table 3.1, the LO phonon emission scattering barrier occurs around the same energy (Figure 3.1). Now using Equation 2.2, and the fact that the non-parabolicity factor $\alpha \cong \frac{I}{e_g}$, where e_g is the band gap, we may obtain an approximate

formulation of the time period of the transient velocity oscillations as:

$$t_p = \frac{23}{E} \sqrt{m_e \left(1 + \frac{0.19}{e_g}\right)} \quad (3.2)$$

where t_p is the time period in pico second (ps), m_e is the ratio of the electron effective mass at the bottom of a subband to the free electron mass, and e_g is in eV.

The transient drift velocity oscillations are expected to be observable as noise in high speed transport measurements [48]. In order to observe the streaming motion noise at the output, a sufficiently small length of CNT may be required. Figure 3.16 shows the average transient drift velocity versus distance for CNT (49,0) at 5 kV/cm and at 10 kV/cm. It can be seen that at 5 kV/cm the oscillations have died down after about 0.7 μm . This distance reduces to 0.3 μm at 10 kV/cm.

3.3.1.b Diameter dependence of the velocity

Figure 3.17 shows the average transient velocity vs. time for various CNTs at room temperature. It can be seen that due to the lower effective masses of the larger tubes, the peak velocity increases with increasing tube diameter. The oscillation is more pronounced and the settling time is longer in larger diameter tubes. This is due to lower damping, since the LA and RBM scattering rates, which provide the damping mechanism [to be discussed shortly], decrease with increasing tube diameter. Just as is seen for the steady-state response, Figure 3.7, CNTs $(3p+1,0)$ show a higher transient velocity than do the CNTs $(3p+2,0)$ because of the larger electron effective mass of the latter.

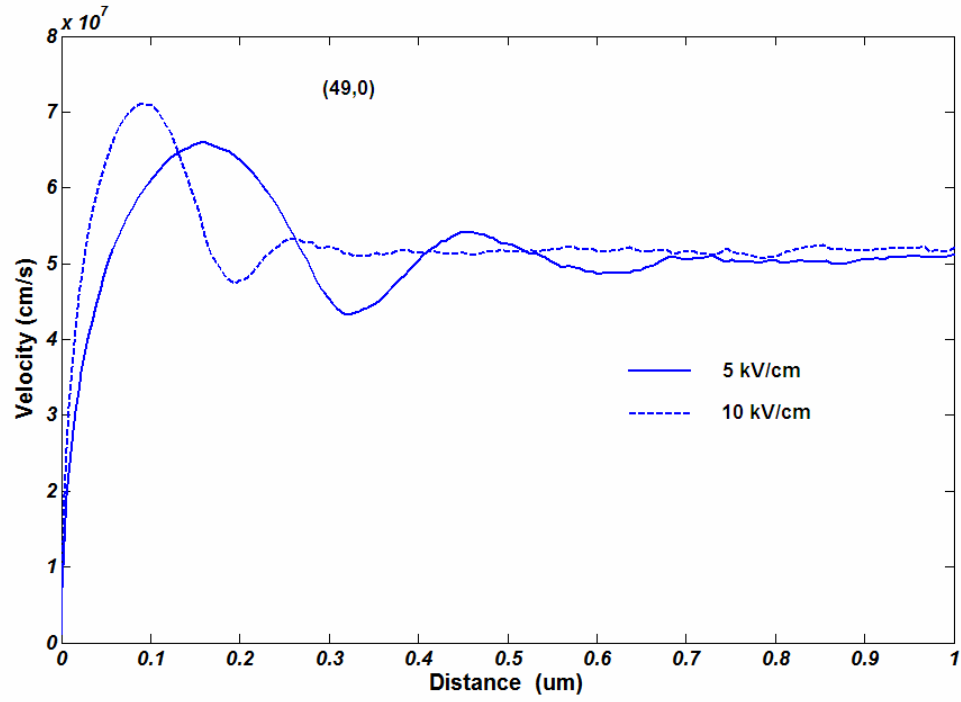


Figure 3.16: Average transient drift velocity versus distance at 5 kV/cm and 10 kV/cm for CNT (49,0) at 300K. Oscillations are seen to persist for long distances, making high frequency noise a possible issue for CNT based devices.

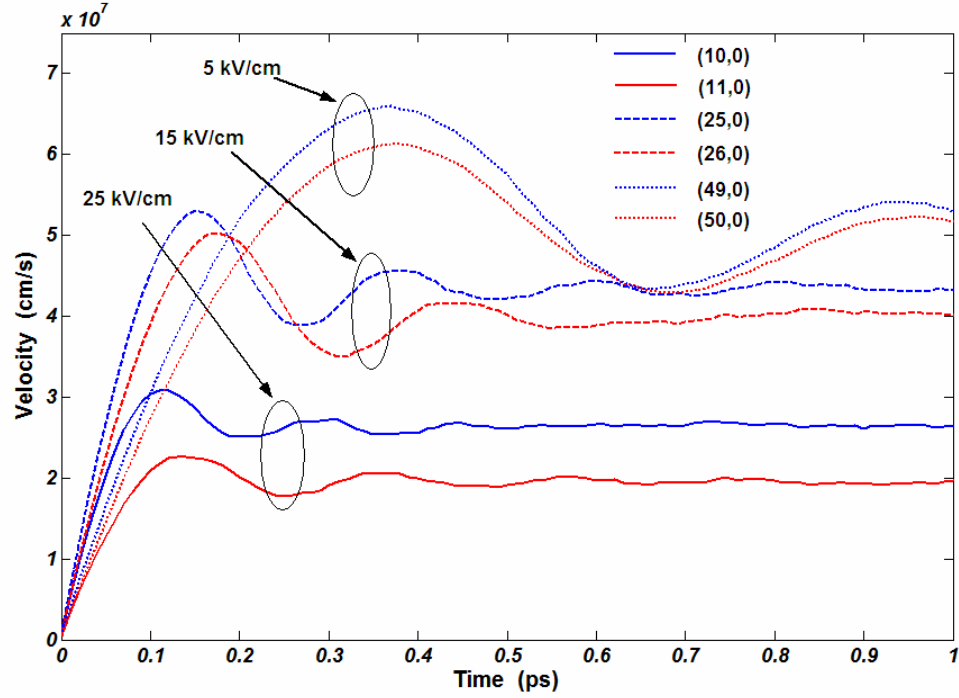
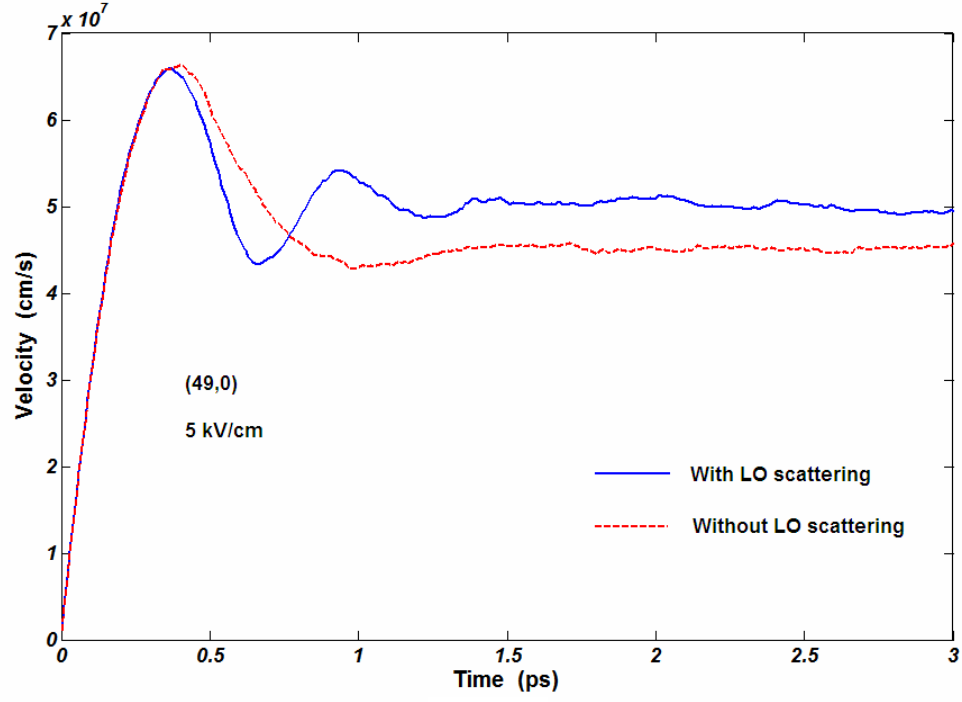


Figure 3.17: Transient velocity response versus time for various CNTs at 300K. As with the steady-state case, smaller diameter CNTs have a lower velocity in accordance with their lower electron effective mass. $(3p+1,0)$ CNTs have higher velocity than do $(3p+2,0)$ CNTs for the same integer p .

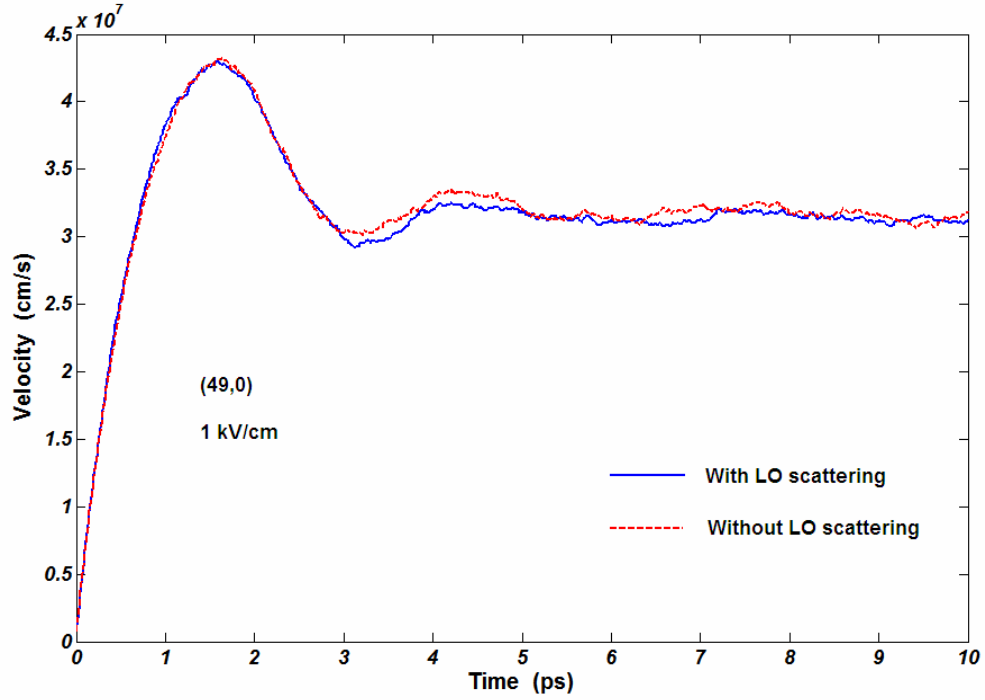
3.3.1.c Effect of various scattering rates

As discussed in the previous sections, three factors determine the transient velocity oscillations. They are the electric field, the ‘strength’ of the scattering barrier that causes electrons to lose nearly all their momentum, and other scattering rates that cause damping. Figure 3.18a shows the average electron transient velocity with time for CNT (49,0) at 5 kV/cm, with and without LO scattering (while LA and RBM scattering mechanisms are present). It can be deduced from the figure that the primary cause of the

velocity oscillation mechanism is the LO phonon scattering. In the absence of LO scattering, electrons can overcome the barrier imposed by LA intersubband emission scattering (Figure 3.2), and hence show little oscillation. However at lower electric fields where there is greater interaction between the electrons and phonons, even the absence of LO scattering can result in velocity oscillations. These are primarily caused by the LA intersubband emission peaks. This can be seen in Figure 3.18b, which shows the electron transient velocity versus time with and without LO scattering at 1 kV/cm. The effect of LO scattering is small but noticeable. The primary cause of damping in oscillations is the combination of LA and RBM scattering. Figure 3.19a and b depict the transient velocity for CNT (49,0) at 5 kV/cm and at 1 kV/cm, respectively, at 300K, when only LO scattering is present, and when all considered phonon scatterings are operational. Extended oscillations are observed, particularly at 1 kV/cm when LA and RBM scatterings are absent. At the higher electric field, i.e., 5 kV/cm, greater intersubband LO scattering (in particular scattering through phonon absorption) is encountered. This results in a decreased velocity change compared to the case when an electric field of 1 kV/cm is applied. In both cases, however, the velocity oscillations are more pronounced and last longer when only LO scattering is present, clearly demonstrating the role played by the LA and RBM phonons in causing damping. This is further illustrated through Figure 3.20, which shows the effect of temperature on the transient velocity oscillations. As can be seen, given the same electric field, oscillations are significantly damped at a high temperature of 600K because of the enhanced LA and RBM phonon scattering. On the other end of the temperature spectrum, at 100K, oscillations are more pronounced because of a decrease in scattering rates.



(a)



(b)

Figure 3.18: Effect of LO scattering on the average transient velocity for CNT (49,0) at 300K at (a) 5 kV/cm and (b) 1 kV/cm. It can be seen that LO phonons are primarily responsible for the transient velocity oscillations. The small oscillations at 1 kV/cm are due to LA intersubband phonon emission scattering.

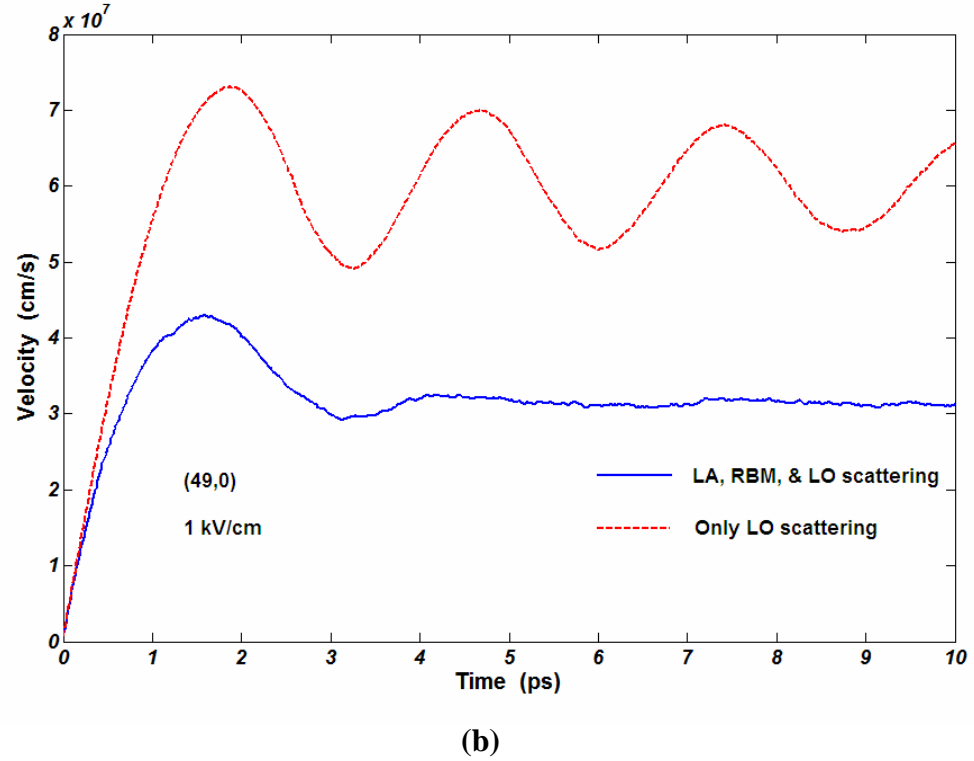
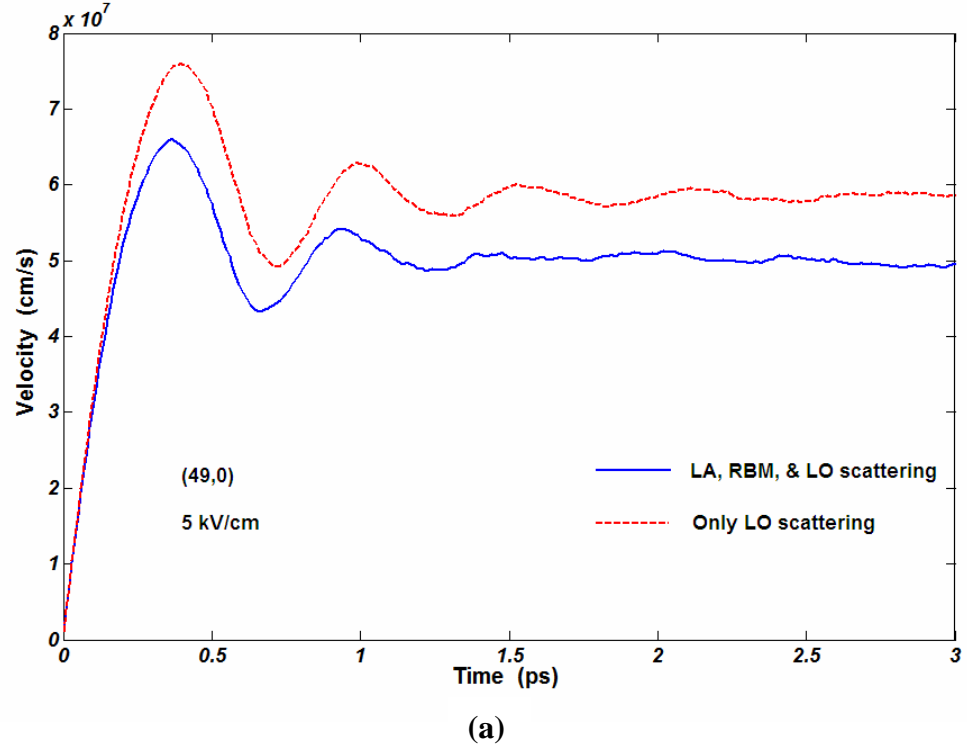


Figure 3.19: Effect of LA and RBM scattering on the transient velocity oscillations for CNT (49,0) at 300K at (a) 5 kV/cm and (b) 1 kV/cm. LA and RBM phonon scattering are seen to be the primary cause of damping in oscillations.

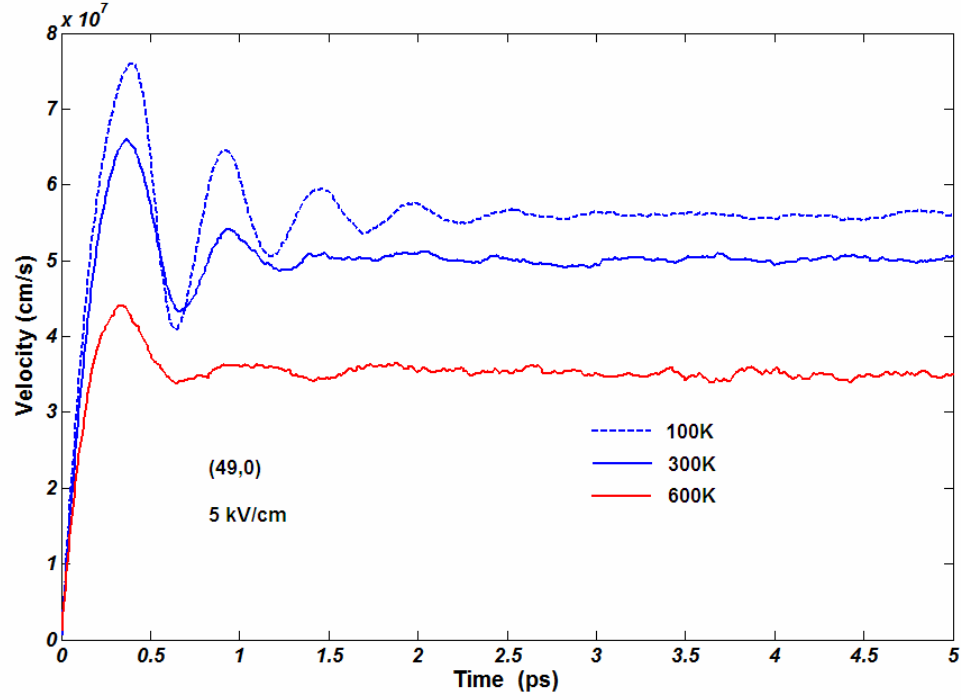


Figure 3.20: Effect of temperature on the transient velocity for CNT (49,0) at 5 kV/cm. At low temperatures, oscillations are more pronounced because of a reduction in scattering.

3.3.2. Ballistic distance

Ballistic distance, or mean free path, is another important parameter from a device application viewpoint. During ballistic transport, electrons traverse the length of the ballistic distance without interacting with the lattice (i.e., scattering). Devices made of sufficiently short lengths, such that ballistic transport occurs, show increased speed of operation. Ballistic distance within CNTs has been a matter of debate for some time.

Various technical articles have used different methodologies to determine the ballistic distances in CNT, or used different assumptions about the ballistic lengths [39,46].

As part of this research work, a graphical method was employed to obtain the ballistic length. The description of this method follows. In the ballistic region, i.e., for $t \ll \tau$, where τ is the relaxation time, the distance traveled by an electron with effective mass m^* is given by, $d_z = QEt^2 / 2m^*$, where E is the applied electric field along the axis of the tube. In the diffusive regime, where $t \gg \tau$, the distance traveled can be expressed as, $d_z = \mu_e Et$, where μ_e is the mobility of electrons. Accordingly, the slope of the log-log plot of average distance traveled by electrons versus time will be two in the ballistic regime and will become unity beyond that. The transition point between the two slopes may be interpreted as the ballistic mean free path and the average relaxation time. This is further illustrated in Figure 3.21, which shows the distance versus time plot for CNT (49,0) at different electric fields. The ballistic distance is seen to vary from ~200 nm to ~50 nm, when the electric field varies from 5 kV/cm to 20 kV/cm. In general, the ballistic distance decreases with increasing electric field for a particular CNT. It is found that the ballistic distances of the $(3p+1, 0)$, and $(3p+2,0)$ CNTs are slightly different at small diameters, with the $(3p+2,0)$ CNTs showing a shorter ballistic distance than do the $(3p+1,0)$ CNTs for the same p and electric field. This is because of the difference in effective mass of the two zigzag CNT families (Figure 1.14). However the ballistic distance becomes nearly equal at large diameters as can be seen in Figure 3.22, which shows the variation of the average distance with time for various CNTs. As a further comparison, under an electric field of 15 kV/cm, ballistic distances are found to be ~25nm and ~60nm for CNTs (10,0) and (50,0) respectively. On the other hand, a ballistic distance

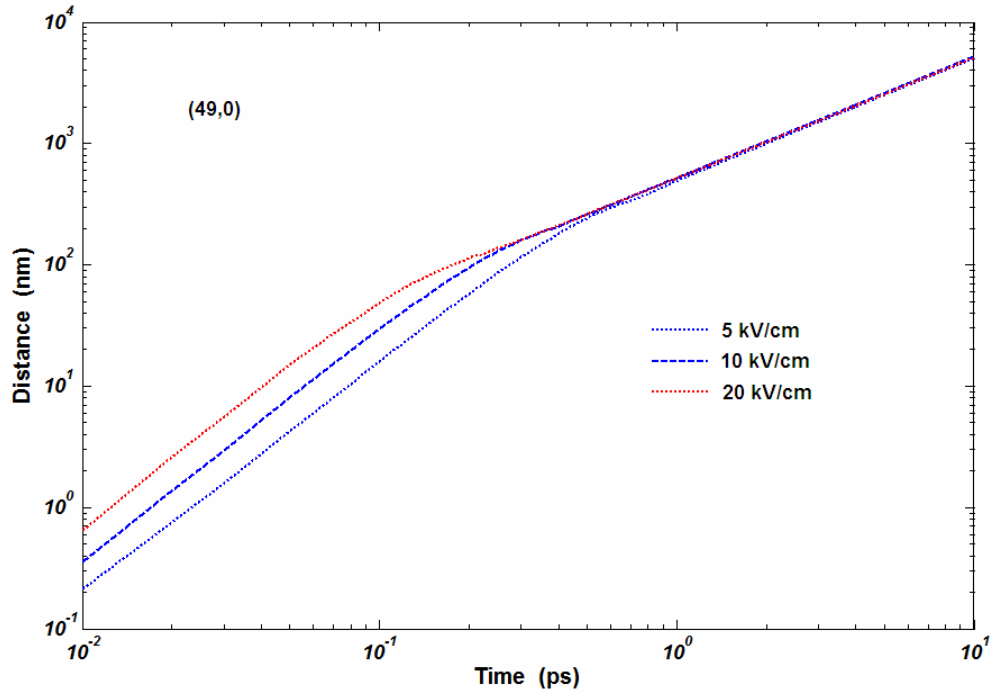


Figure 3.21: Average electron distance traveled versus time for CNT (49,0) at 300K and various electric fields. The region of high slope signifies ballistic transport, while low slope signifies diffusive transport. Ballistic distance, which is the point at which the change in slope occurs, is seen to decrease with increasing electric field.

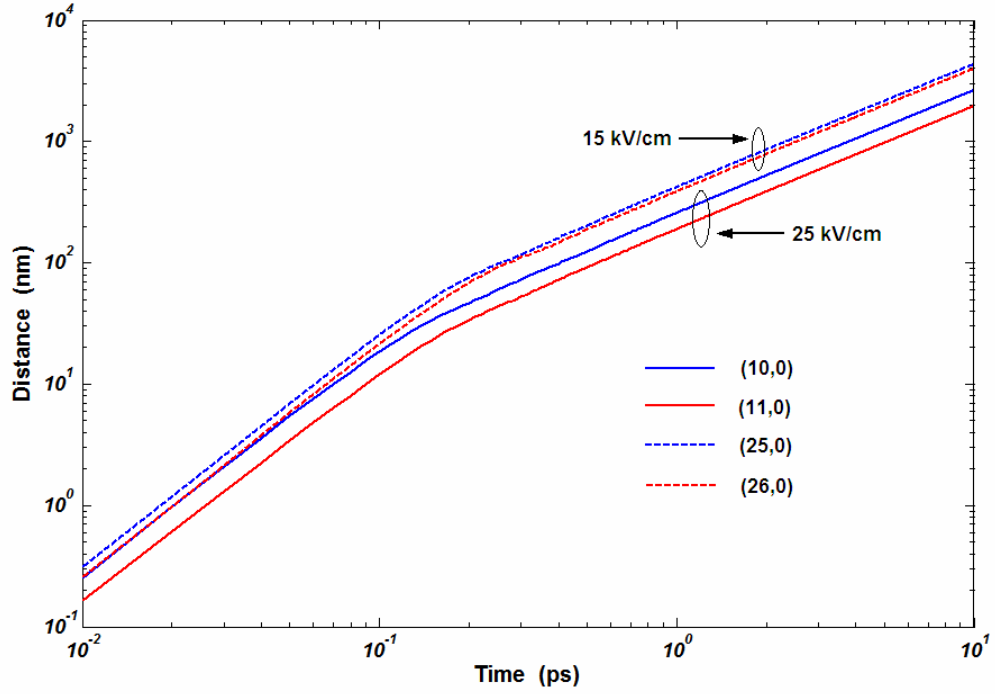


Figure 3.22: Variation of the average electron distance traveled versus time across various CNTs at 300K. Ballistic distance becomes nearly equal for both semiconducting zigzag CNT families at large diameters (for same integer p and electric field).

of ~30 nm is obtained for CNTs (10,0) and (50,0) at electric fields of 10 kV/cm and 32 kV/cm, respectively. These values are in the range of recently extracted experimental values [39].

Chapter 4

Conclusion

4.1 Conclusions

Within the course of the research that formed this thesis, a comprehensive numerical study of the electron transport in semiconducting zigzag $(n,0)$ carbon nanotubes (CNTs) has been performed. An Ensemble Monte Carlo (EMC) algorithm is utilized to model the electron transport properties under a wide range of external stimuli. Additionally, Rode's method is used to investigate the low-field mobility. Through the results obtained, it has been found that even though each CNT is unique in terms of its electrical response, and must be chosen for a particular application based on its own merit, there are general features that make it easier to predict its behavior. In order to understand comprehensively the basis of the results, certain physical aspects of the CNTs simulated have to be kept in mind. They are:

1. Two semiconducting zigzag CNT families exist. They may be represented as $(3p+1, 0)$, and $(3p+2,0)$ where p is an integer.
2. For the same integer value of p , the lowest subband electron effective mass is lower for CNT $(3p+1,0)$ than for CNT $(3p+2,0)$.

3. The difference in the effective masses between the two families decreases with increasing tube diameter.
4. In general, for CNTs with different values of p , the effective mass decreases with increasing diameter.

By considering the above points, certain aspects of electron transport are seen to emerge. They are summarized in the following subsections.

4.1.1 Low-field mobility

Low-field mobility for various CNTs is obtained through Rode's method. Only the lowest subbands are considered, and an analytical approximation (with a non-parabolicity factor incorporated) is used to model those subbands. In addition, the mobility values obtained are confirmed through EMC simulations below electric fields of 1 kV/cm. The following conclusions may be drawn from the results:

1. Low-field mobility is primarily affected by electron scattering from longitudinal acoustic (LA) and radial breathing mode (RBM) phonons. Longitudinal optical (LO) phonons play an insignificant role.
2. Due to the electron effective mass difference, $(3p+1,0)$ CNTs have a higher low-field mobility than do $(3p+2,0)$ CNTs for the same integer p .
3. Low-field mobility shows a wide variation with tube diameter. At 300K, CNT (10,0) has a mobility value of $\sim 2,700 \text{ cm}^2/\text{V-s}$, while for CNT (49,0) the value is

$\sim 65,000 \text{ cm}^2/\text{V-s}$. This is due to the smaller effective mass and the reduced electron scattering for larger diameter tubes.

4. At lower temperatures, higher low-field mobility values are obtained, because of a reduction in the scattering rates. For example, at a temperature of 100K, the mobility for CNT (49,0) is obtained as $\sim 160,000 \text{ cm}^2/\text{V-s}$, whereas it is $\sim 6,500 \text{ cm}^2/\text{V-s}$ for CNT (10,0).
5. The contribution of the RBM phonons in the low field mobility is different for the two zigzag CNT families, though it is almost independent of tube diameter. For the $(3p+1,0)$ family, the contribution is nearly 25%, while for the $(3p+2,0)$ family, it is about 18%.

4.1.2 Field dependent mobility

We have also investigated the steady-state average electron drift velocity as a function of applied electric fields for various semiconducting zigzag CNTs. The drift velocity shows a few trends that are similar to those of the low-field mobility. These are:

1. The velocity is higher for CNT $(3p+1,0)$ compared to CNT $(3p+2,0)$ for the same integer p ,
2. The velocity increases considerably for larger diameter CNTs, and,
3. The velocity is inversely proportional to the temperature.

However, there are also other important features that are a consequence of electrons participating in streaming motion, which is due to an electron scattering barrier

imposed by acoustic and optical phonon emission processes within a dynamically 1-D band structure, and the difference between the effective masses among subbands within a CNT. In the small diameter regime, electron drift velocity saturates at intermediate electric fields because of the streaming motion. Velocity saturation is primarily caused by the strong LO emission. At higher electric fields, $(3p+1,0)$ CNT families show a negative differential mobility (NDM), where the drift velocity decreases with an increase in electric field. This phenomenon, which is also observed in other semiconductor materials such as GaAs, is caused by an electron transition from a lower subband with smaller effective mass to higher subbands with larger effective masses. The magnitude of the NDM is dependent on the relative differences among the electron effective masses within the subbands involved. The absence of NDM in the lower diameter $(3p+2,0)$ CNTs is not due to the absence of electron transitions to higher subbands, but due to the insignificant difference in the electron effective masses within the subbands. At relatively high electric fields, the average steady-state drift velocity becomes essentially independent of temperature. This is because at such high electric fields, electron scattering is dominated by phonon emission, which shows decreased sensitivity to temperature.

Large diameter CNTs show a more pronounced NDM, and a reduced range of electric fields for which velocity saturation occurs. Moreover, the saturation electric field, E_{sat} (the electric field at which velocity saturation occurs), is lower. This is because, since the electron effective mass is lower for larger diameter CNTs, and the subbands more closely spaced, electrons quickly gain enough energy from the field to make transitions to higher subbands. Therefore more than two subbands (each subband four-fold degenerate including spin) play roles in larger diameter CNTs. The relative velocity difference

between the two zigzag semiconducting families also decreases with increasing diameter. This is in accord with the decrease in relative difference in electron effective mass.

4.1.3 Transient phenomenon

4.1.3.a Velocity response

The transient velocity response within CNTs is guided by the electron streaming motion that results from strong acoustic and optical phonon emission. This results in velocity oscillations at intermediate electric fields. LO phonons are the dominant cause of oscillations, while LA and RBM phonons are the primary cause of damping. This is significantly different from the behavior of 3-D semiconductor materials, where the average transient velocity reaches a peak, and then drops to a lower steady-state value. At lower temperatures, velocity oscillations can be significantly more pronounced because of a reduced scattering rate. At low electric fields, electrons have sufficient time to interact with the phonons, thereby resulting in little or no oscillations in velocity. At the other extreme, i.e., high electric fields, electrons gain enough energy to overcome the scattering barrier, again resulting in little or no oscillations. Within the intermediate field regime, the time period of the oscillations is approximately twice the time it takes for the velocity to reach the maximum value, and is inversely proportional to the applied electric field.

Transient velocity oscillations are expected to manifest themselves under various circumstances. The most obvious is a high frequency noise response in the CNT to an applied voltage. Moreover, since any accelerating charge emits electromagnetic radiation [49], these velocity oscillations are expected to result in radiation that can be measured. Since the time period of the velocity oscillations is dependent upon the applied electric

field, one suggested application of this phenomenon could be a nano-scale voltage controlled oscillator. To date, however, there has been no direct evidence of the occurrence of the oscillations in experiments.

The transient velocity response is also different for the two zigzag families, where the $(3p+1,0)$ CNTs show higher electron velocities than do the $(3p+2,0)$ CNTs at the same electric field. This is attributed to the difference in the electron effective mass between the two CNT families.

4.1.3.b Ballistic distance

The ballistic distance has been found to be of the order of tens of nanometers for the various CNTs investigated. This is in the range of experimental results. The ballistic distance is found to be dependent upon the applied electric field (inversely proportional), and the CNT diameter. In general, larger diameter CNTs show greater ballistic lengths. The method utilized to evaluate the ballistic distance in our work involved tracking the log of the average distance traveled by the electron ensemble, versus the log of the time. The region of the higher slope (≈ 2) corresponds to ballistic transport, while the region of lower slope (≈ 1) corresponds to diffusive transport. Ballistic distances of the two zigzag semiconducting CNT families, $(3p+1,0)$ and $(3p+2,0)$ are found to be nearly equal for large diameter CNTs and same integer p .

4.2 Recommendations for future work

Research work presented in this thesis opens up a range of possibilities for further research work in this area. Briefly, these possibilities are:

1. Chiral CNTs: Semiconducting zigzag CNTs have shown a richness and diversity in transport properties that are truly impressive. It is found that there is a variation of these properties with the CNT diameter. Moreover, there are two distinct zigzag semiconducting CNT families and their response to external stimuli is different. However to complete the study of the entire class of semiconducting single-wall CNTs (SWCNTs), it is important to investigate semiconducting chiral CNTs too. This will allow a greater understanding of the diameter dependence on electron transport, and help in formulating important analytical expressions that predict various transport properties such as the low-field mobility.
2. Incorporation of other scattering mechanisms: Most semiconductor electronic applications do not use an intrinsic semiconductor material. The material is doped with impurities to increase the concentration of either electrons or holes. These ionized impurities present another significant scattering mechanism. Developing a formulation for incorporating this scattering mechanism within the CNT EMC scheme has been a challenge. Since the interaction potential between an electron and an ionized impurity varies as the inverse of the distance between these two charge species, the potential will tend to mathematically become infinite as the electron approaches the impurity ion. Therefore a treatment of this interaction that overcomes the mathematical singularity will require further theoretical

approximations and/or experimental data. This will also provide the basis for another important scattering mechanism, the electron-electron short range interaction. This is because the interaction potential between two electrons, or between an electron and ion atom is expected to be similar.

3. Hole transport: Incorporation of the hole simulator within the present EMC CNT scheme is relatively straightforward. Since the CNT band structure is symmetric around the Fermi level, hole behavior is expected to be essentially the same as electron behavior. The easiest way to include a hole simulator, therefore, would be to use the electron simulator with the charge reversed on the electrons.
4. Breakdown study: An investigation of the electrical breakdown of CNTs is extremely important because it places a bound on the range of electric fields within which a CNT may be operated.
5. Device simulator: After incorporating the above within the EMC model, the base is set to investigate a device that utilizes CNTs, for example a CNT field effect transistor (CNTFET). In addition to CNT material transport properties, additional features that need to be incorporated within the device simulator are the boundary metal-CNT contacts, and a Poisson solver that includes the physical geometry of the device.

APPENDIX

Electron-phonon interaction

The matrix element for the electron-phonon interaction for a CNT is given by [22]:

$$\left| \left\langle \psi_f \left| H^{ep} \right| \psi_i \right\rangle \right|^2 = \sum_{\substack{\text{all possible} \\ \mathbf{q} \text{ and } \mu}} \frac{\hbar^2 D^2}{2\rho\Omega e_p(\mathbf{q}, \mu)} \times \left(N[e_p(\mathbf{q}, \mu)] + \frac{1}{2} \pm \frac{1}{2} \right) \quad (\text{A.1})$$

where ψ_f and ψ_i are the final and initial electron states respectively, H^{ep} is the electron-phonon interaction, ρ is the CNT mass density, Ω is volume of the CNT, \hbar is the reduced Plank's constant, and N is the phonon Bose-Einstein phonon occupation number for a phonon energy e_p . \mathbf{q} and μ are the phonon wave vector and branch index respectively. The above formulation assumes a value of unity of the overlap between the cell periodic parts of the initial and final Bloch states. Also,

$$D^2 = \begin{cases} D_{LA}^2 \left[q^2 + \left(\frac{2\mu}{d} \right)^2 \right] & \text{acoustic phonon scattering} \\ D_{LO}^2 & \text{optical phonon scattering} \\ D_{RBM}^2 & \text{RBM phonon scattering} \end{cases} \quad (\text{A.2})$$

where $q = |\mathbf{q}|$, and D_{LA} , D_{LO} , and D_{RBM} are the longitudinal acoustic, longitudinal optical, and radial breathing mode deformation potentials or deformation potential fields, respectively.

Using Fermi's Golden Rule, the electron scattering rate is given by:

$$W(\mathbf{k}_i) = \frac{\Omega}{2\pi} \int \left| \left\langle \psi_f \left| H^{ep} \right| \psi_i \right\rangle \right|^2 \delta \left(e_{\mathbf{k}_f} - e_{\mathbf{k}_i} \mp e_p(\mathbf{q}, \mu) \right) d\mathbf{k}_f \quad (\text{A.3})$$

However, it is easier to perform the integral over the phonon wave vector \mathbf{q} rather than the final electron wave vector \mathbf{k}_f . Now, equation A.3 may be compared to the standard integral form involving Dirac-delta function [43]:

$$\int_{-\infty}^{+\infty} f(x) \delta(g(x)) dx = \sum_i \frac{f(x_i)}{|g'(x_i)|} \quad (\text{A.4})$$

Using equations A.1, A.3, and A.4 we obtain the electron-phonon scattering rate

as:

$$W(\mathbf{k}_i, v_i) = \sum_{\substack{\text{all possible} \\ \mathbf{q} \text{ and } \mu}} \frac{\hbar^2 D^2}{2\rho\Omega e_p(\mathbf{q}, \mu)} \times \left(N[E_p(\mathbf{q}, \mu)] + \frac{1}{2} \pm \frac{1}{2} \right) \times d\delta \quad (\text{A.5})$$

$$\text{where } d\delta = \left| \frac{de_{\mathbf{k}_f}}{d\mathbf{q}} - \frac{de_{\mathbf{k}_i}}{d\mathbf{q}} \pm \frac{de_p(\mathbf{q}, \mu)}{d\mathbf{q}} \right|^{-1} \quad (\text{A.6})$$

Now since the initial state of the electron is independent of the phonon wave vector,

hence $\frac{de_{\mathbf{k}_i}}{d\mathbf{q}} = 0$. Therefore,

$$d\delta = \left| \frac{de_{\mathbf{k}_f}}{d\mathbf{q}} \pm \frac{de_p(\mathbf{q}, \mu)}{d\mathbf{q}} \right|^{-1} \quad (\text{A.7})$$

Now, $\frac{de_{\mathbf{k}_f}}{d\mathbf{q}} = \frac{de_{\mathbf{k}_f}}{d\mathbf{k}_f} \times \frac{d\mathbf{k}_f}{d\mathbf{q}}$, and since $\mathbf{k}_f = \mathbf{k}_i \pm \mathbf{q}$, therefore, $\frac{d\mathbf{k}_f}{d\mathbf{q}} = \pm 1$. Using these

relationships, $d\delta$ can now be formulated in a form that can be easily evaluated from the tabulated values of the electron and phonon dispersion. This expression is:

$$d\delta = \left| \pm \frac{de_{\mathbf{k}_f}}{d\mathbf{k}_f} \pm \frac{de_p(\mathbf{q}, \mu)}{d\mathbf{q}} \right|^{-1} \quad (\text{A.8})$$

THESIS PUBLICATIONS

- 1 A. Verma, M.Z.Kauser, B.W.Lee, K.F.Brennan, and P.P.Ruden, “Ensemble Monte Carlo transport simulations for semiconducting carbon nanotubes”, Proceedings of the 27th International conference on Physics of Semiconductors (ICPS), Flagstaff, AZ, 2004, AIP Conference Proceedings, vol. 772, p. 1049, 2005.
- 2 A.Verma, M.Z.Kauser, and P.P.Ruden, “Ensemble Monte Carlo transport simulations for semiconducting carbon nanotubes”, Journal of Applied Physics, vol. 97, p. 114319, 2005.
- 3 A. Verma, M.Z.Kauser, and P.P.Ruden, “Effects of radial breathing mode phonons on charge transport in semiconducting carbon nanotubes”, Applied Physics Letters, vol. 87, p. 123101, 2005.
- 4 M.Z.Kauser, A.Verma, and P.P.Ruden, “Low and high field transport for semiconducting carbon nanotubes”, Proceedings of the 16th conference of Electron Properties of 2-Dimensional Systems (EP2DS-16), July 2005, accepted for publication.

REFERENCES

- [1] S. Iijima, "Helical microtubules of graphitic carbon", Nature, vol. 354, p. 56, 1991.
- [2] S. Baker and A. Aston, "The business of nanotech", BusinessWeek, 14 Jan., p.64, 2005.
- [3] R. Saito, M. S. Dresselhaus, and G. Dresselhaus, Physical Properties of Carbon Nanotubes, Imperial College Press, London, 1998.
- [4] K. Welsher , "Carbon Nanotube Electronics", <http://spice.chem.emory.edu/students/welsher/history.html>, Accessed: 08/15/2005.
- [5] S. J. Tans, A. R. M. Verschueren, and C. Dekker, "Room-temperature transistor based on a single carbon nanotube", Nature, vol. 393, p. 49, 1998.
- [6] A. Bachtold, P. Hadley, T. Nakanishi, and C. Dekker, "Logic circuits with carbon nanotube transistors", Science, vol. 294, p.1317, 2001.
- [7] J. A. Misewich, R. Martel, Ph. Avouris, J. C. Tsang, S. Heinze, and J. Tersoff, "Electrically induced optical emission from a carbon nanotube FET", Science, vol. 300, p. 783, 2003.
- [8] V. Derycke, R. Martel, J. Appenzeller, and Ph. Avouris, "Carbon nanotube inter- and intramolecular logic gates", Nano Letters, vol. 1, p. 453, 2001.
- [9] L. Chico, V.H. Crespi, L.X. Benedict, S.G. Louie, and M.L. Cohen, "Pure carbon nanoscale devices: nanotube heterojunctions", Physical Review Letters, vol. 76, p. 971, 1996.
- [10] P.G. Collins, A. Zettl, H. Brando, A. Thess, and R.E. Smalley, "Nanotube nanodevice", Science, vol. 278, p. 100, 1997.
- [11] Chi-Ti Hseish, "Carrier transport in optical-emitting devices based on carbon-nanotube field-effect transistors", diss, Atlanta: Georgia Institute of Technology.
- [12] P. Avouris, J. Appenzeller, R Martel, and S. J. Wind, " Carbon nanotube electronics", Proceedings of the IEEE, vol. 91, no. 11, p. 1772, 2003.
- [13] ILJIN CNT, "Synthesis methods", <http://www.iljinnanotech.co.kr/en/material/r-4-1.htm>, Accessed: 08/15/2005.
- [14] S. Iijima and T. Ichihashi, "Single-shell carbon nanotubes of 1-nm diameter",

Nature, vol. 363, p. 603, 1993.

- [15] D.S. Bethune, C.H. Kiang, M.S. de Vries, G. Gorman, R. Savoy, J. Vazquez, and R. Beyers, “Cobalt-catalysed growth of carbon nanotubes with single-atomic-layer walls”, Nature vol. 363, p. 605, 1993.
- [16] M.S. Dresselhaus, G. Dresselhaus, and R. Saito,” Physics of carbon nanotubes”, Carbon, Vol. 33, No. 7, p. 883, 1995
- [17] H. Suzuura and T. Ando, “Phonons and electron-phonon scattering in carbon nanotubes”, Physical review B, vol. 65, p. 235412, 2002.
- [18] T. W. Odom, J. L. Huang, P. Kim, and C. M. Lieber, “Atomic structure and electronic properties of single-walled carbon nanotubes”, Nature, vol. 391, p. 62, 1998.
- [19] J.W. Mintmire and C.T. White, “Universal Density of States for Carbon Nanotubes”, Physical Review Letters, vol. 81, p. 2506, 1998.
- [20] J. Guo and M.A. Alam,” Carrier transport and light-spot movement in carbon-nanotube infrared emitters”, Applied Physics Letters, vol. 86, p. 023105, 2005.
- [21] V. Perebeinos, J. Tersoff, and Ph. Avouris, “Electron-Phonon Interaction and Transport in Semiconducting Carbon Nanotubes”, Physical Review Letters, vol. 94, p. 86802, 2005.
- [22] G. Pennington and N. Goldsman, “Monte Carlo Study of Electron Transport in a carbon nanotube”, IEICE Trans. Electron., vol. E86-C, p. 372, 2003.
- [23] G. Pennington and N. Goldsman, “Semiclassical transport and phonon scattering of electrons in semiconducting carbon nanotubes”, Physical Review B, vol. 68, p. 045426, 2003.
- [24] J. Guo and M. Lundstrom, “Role of phonon scattering in carbon nanotube field-effect transistors”, Applied Physics Letters, vol. 86, p. 193103, 2005.
- [25] A. Maiti, A. Svizhenko, and M.P. Anantram, “Electronic transport through carbon nanotubes: effects of structural deformation and tube chirality”, Physical Review Letters, vol. 88, p. 126805, 2002.
- [26] C. Jacoboni and P. Lugli, The Monte Carlo method for semiconductor device simulation, Wein , New York : Springer-Verlag, 1989.
- [27] K. Hess, Ed., Monte Carlo Device Simulation: Full Band and Beyond, Kluwer Academic Publishers, Dordrecht, Netherlands, 1991.

- [28] K.F. Brennan, D.H. Park, and Y. Wang, “Design and comparison of advanced semiconductor devices using computer experiments: application to APDs and HEMTs”, IEEE Transactions on Electron Devices, vol. 37, no. 3, 1990.
- [29] Wikipedia, the free encyclopedia : User-Kebe, “Carbon nanotube”, <http://en.wikipedia.org/wiki/Image:CNTnames.png>, Accessed: 08/15/2005.
- [30] K.F. Brennan, The Physics of Semiconductors: With Applications to Optoelectronic Devices, Cambridge University Press, 1999.
- [31] A. De Martino, “An introduction to the theory of carbon nanotubes”, http://www.cs.infn.it/de_martino_1.ppt, Accessed: 08/16/2005.
- [32] A. Kleiner and S. Eggert, “Curvature, hybridization, and STM images of carbon nanotubes”, Physical Review B, vol. 64, p. 113402, 2001.
- [33] J. W. Ding, X. H. Yan, and J. X. Cao, “Analytical relation of band gaps to both chirality and diameter of single-wall carbon nanotubes”, Physical Review B, vol. 66, p. 073401, 2002.
- [34] K. Kanamitsu and S. Saito, “Geometries, electronic properties, and energetics of isolated single walled carbon nanotubes”, Journal of Physics Society of Japan, vol. 71, p. 483, 2002.
- [35] B. J. LeRoy, S. G. Lemay, J. Kong, and C. Dekker, “Electrical generation and absorption of phonons in carbon nanotubes”, Nature, vol. 432, p. 371, 2004.
- [36] M. Machon, S. Reich, H. Telg, J. Maultzsch, P. Ordejon, and C. Thomsen, “Strength of radial breathing mode in single-walled carbon nanotubes”, Physical Review B, vol. 71, p. 035416, 2005.
- [37] J. Kurti, G. Kresse, and H. Kuzmany, “First-principles calculations of the radial breathing mode of single-wall carbon nanotubes”, Physical Review B, vol. 58, p. 8869, 1998.
- [38] J. Singh, Physics of Semiconductors and Their Heterostructures, McGraw-Hill, 1993.
- [39] A. Javey, J. Guo, M. Paulsson, Q. Wang, D. Mann, M. Lundstrom, and H. Dai, “High-field quasiballistic transport in short carbon nanotubes”, Physical Review Letters, vol. 92, p. 106804, 2004.
- [40] M. Freitag, V. Perebeinos, J. Chen, A. Stein, J.C. Tsang, J.A. Misewich, R. Martel, and Ph. Avouris, “Hot carrier electroluminescence from a single carbon nanotube”, Nano Letters, vol. 4, p. 1063, 2004.

- [41] K. Tomizawa, Numerical Simulation of Submicron Semiconductor Devices, Artech House, Boston, London, 1993.
- [42] M. Lundstrom, Fundamentals of Carrier Transport, Second edition, Cambridge University Press, 2000.
- [43] E. Kreyszig, Advanced Engineering Mathematics, Fifth Edition, Wiley Eastern, 1983.
- [44] J. Y. Park, S. Rosenblatt, Y. Yaish, V. Sazonova, H. Üstünel, S. Braig, T. A. Arias, P. W. Brouwer, and P. L. McEuen, “Electron-phonon scattering in metallic single-walled carbon nanotubes”, Nano Letters, vol. 4, p. 517, 2004.
- [45] D. L. Rode, “Low-field transport in semiconductors,” in Semiconductors and Semimetals, vol. 10, R. K. Willardson and A. C. Beer, Eds. Academic Press, 1972.
- [46] P. L. McEuen, M.S. Fuhrer, and H. Park, “Single-walled carbon nanotube electronics”, IEEE Transactions on Nanotechnology, vol. 1, p. 78, 2002.
- [47] D. Javanovic and J.P. Leburton, “Electron-phonon interaction and velocity oscillations in quantum wire structures”, Superlattices and Microstructures, vol. 11, p. 141, 1992.
- [48] A.Suizhenko, S.Bandyopadhyay, and M. A.Stroscio, “Velocity fluctuations and Johnson noise in quantum wires: the effect of phonon confinement”, Journal of Physics: Condensed Matter, vol. 11, p. 3697, 1999.
- [49] D. J. Griffiths, Introduction to Electrodynamics, Second Edition, Prentice-Hall, 1989.